March 2019

Probing Quantized Excitations and Many-body Correlations in Transition Metal Dichalcogenides with Optical Spectroscopy

Shao-Yu Chen

PROBING QUANTIZED EXCITATIONS AND MANY-BODY CORRELATIONS IN TRANSITION METAL DICHALCOGENIDES WITH OPTICAL SPECTROSCOPY

A Dissertation Presented

by

SHAO-YU CHEN

Submitted to the Graduate School of the
University of Massachusetts Amherst in partial fulfillment
of the requirements for the degree of

DOCTOR OF PHILOSOPHY

February 2019

Department of Physics

PROBING QUANTIZED EXCITATIONS AND MANY-BODY CORRELATIONS IN TRANSITION METAL DICHALCOGENIDES WITH OPTICAL SPECTROSCOPY

A Dissertation Presented

by

SHAO-YU CHEN

Approved as to style and content by:

_____
Jun Yan, Chair

_____
Anthony Dinsmore, Member

_____
Jae-Hwang Lee, Member

_____
Chen Wang, Member

_____
Narayanan Menon., Department Head of Physics

DEDICATION

To my beloved Mua-Ji and Song-Jin Yang.

ACKNOWLEDGMENTS

First and the foremost, I would like to deeply thank my advisor Dr. Jun Yan. His supportive advices steered me in the right direction, enabling me to complete my Ph.D. program smoothly. I am also grateful to my lab mates Jiayue Tong, Tom Goldstein and Yueh-Chun Wu. I enjoyed and learned plenty from working with them. My research would have been impossible without the aid and the support from them. I would like to thank the collaborators Zhengguang Lu and Dr. Dimtri Smirnov in National High Magnetic Field Laboratory. They provided me invaluable help with the magneto-optical measurement with high magnetic fields. I would like to give my special thanks to Dr. Matthew Sfeir from Brookhaven National Laboratory. He is very supportive to help us setting up the time-resolved PL measurements. I benefit greatly from interaction and collaboration with him.

My sincere thanks to my friends Wei-Ting Wong, Huei-Shian Lin, Hsin-Ting Huang, Szu Yin Lin, Hsin Fei Tu, Ning-Hsuan Tseng, Li Yang Ku, FangLing Yeh, Ming-che Liu, Shih-chan Dai, Cheng-Hsuan Li, Rui Cao, Wanting Xie, Meng Xin, and Qingqing Zhang. My life in Amherst could not be fulfilled without them. Last but by no means least, I must explicit my gratitude to my parent, sibling and Tammy Wu for providing me with unfailing support and continuous encouragement throughout my Ph.D. studies. This accomplishment would not have been possible without them.

ABSTRACT

PROBING QUANTIZED EXCITATIONS AND MANY-BODY CORRELATIONS IN TRANSITION METAL DICHALCOGENIDES WITH OPTICAL SPECTROSCOPY

FEBRUARY 2019

SHAO-YU CHEN

B.A., NATIONAL TAIWAN UNIVERSITY

M.A., NATIONAL TAIWAN UNIVERSITY

Ph.D., UNIVERSITY OF MASSACHUSETTS AMHERST

Directed by: Professor Jun Yan

Layered transition metal dichalcogenides (TMDCs) have attracted great interests in recent years due to their physical properties manifested in different polytypes: Hexagonal(H)-TMDC, which is semiconducting, exhibits strong Coulomb interaction and intriguing valleytronic properties; distorted octahedral(T')-TMDC, which is semi-metallic, is predicted to exhibit rich nontrivial topological physics. In this dissertation, we employ the polarization-resolved micron-Raman/PL spectroscopy to investigate the optical properties of the atomic layer of several polytypes of TMDC.

In the first part for polarization-resolved Raman spectroscopy, we study the lattice vibration of both H and T'-TMDC, providing a thorough understanding of the polymorphism of TMDCs. We demonstrate that Raman spectroscopy is a versatile tool to probe the symmetry as well as the quality of crystals. This becomes quite important for

atomic layers of TMDCs which are sensitive to the environment and substrate. In the second part of the dissertation, we focus on fabricating high-quality monolayer tungsten diselenide samples and study their excitonic bound states by photoluminescence, reflection, resonant-Raman spectroscopy, magneto-optical measurements and time-resolved spectroscopy. We first demonstrate the many-body correlation of the multi-particle bound excitonic states at low temperatures. The PL measurement in magnetic fields demonstrate for the first time the abnormal valleytronic properties of the biexciton and five-particle bound states, exciton-trion in 1L-TMDCs. The time-resolved PL measurement reveals the ultralong lifetime of the several bound states at even lower energy range, establishing a potential platform for further investigation on exciton condensation. In addition to the lower energy bound states, we also explore its excited Rydberg states in high magnetic fields. Surprisingly, we observe for the first time the PL of up to 4*s* excitons, opening doors to the investigation the physics of Rydberg exciton in a 2D system. For example, we investigate the role of electron-hole exchange-interactions in 2*s* exciton. Contrary to 1*s* exciton, the exchange interaction in 2*s* exciton is strongly suppressed due to its larger size. Consequently, the 2*s* display superior valley polarization and valley coherence, paving the way to valleytronic applications.

TABLE OF CONTENTS

Page

LIST OF TABLES

Table Page

LIST OF FIGURES

Figure Page

CHAPTER 1

BACKGROUND

1.1 Polymorphism of Two-Dimensional Transition Metal Dichalcogenide

Two-dimensional transition metal dichalcogenide (2D-TMDC) is a class of van der Waals nanomaterials that exhibits interesting phase transition within its various polytypes. As illustrated in Figure 0.1, the unit layer of 2D-TMDC is composed by MX_2 three atomic layers [1]: a center transition metal(M) (e.g. Mo, W) atomic layer sandwiched by the top and bottom chalcogen (X) (e.g. S, Se, Te) atomic layers. The three atomic layers are linked by covalent bonds, forming a triatomic unit layer. The unit layers can be further stacked with van der Waals forces to form a few layer TMDCs, reflecting the nature of van der Waals crystal.

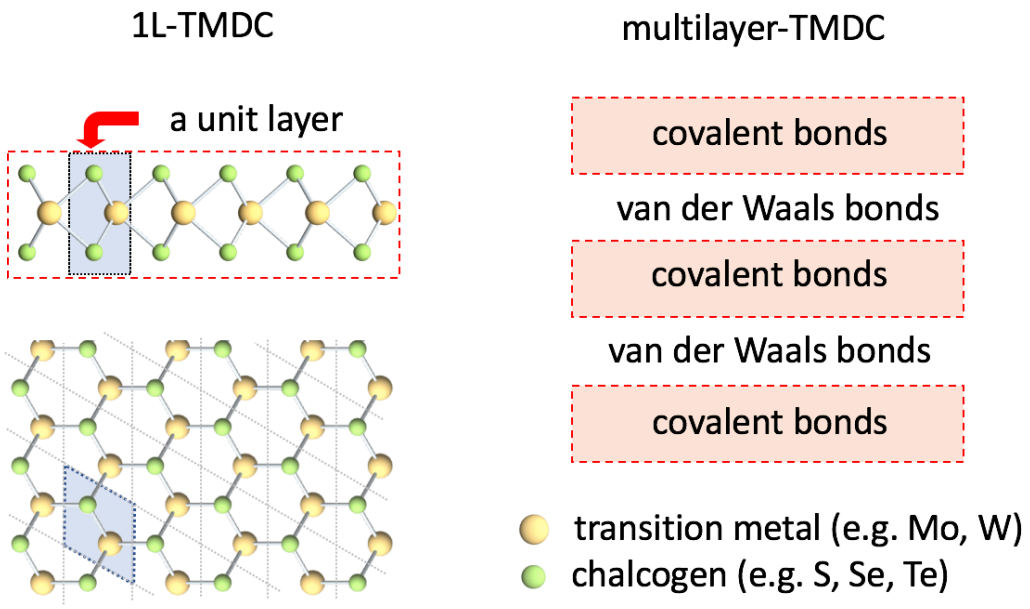

Figure 0.1: Schematic of monolayer and multilayer-TMDCs. The red dash squares enclose the unit layer of TMDCs. Atoms in the unit layer are linked by covalent bonds, while the unit layers are coupled by van der Waals force.

The polymorphs in 2D-TMDCs can be categorized by intralayer and interlayer polytypes. The structure presented in Figure 0.1 is the hexagonal (H) phase of 1L TMDCs; the unit cell is arranged in triangular lattice which can be seen from the top perspective view. Indeed, 2D-TMDCs have other intralayer polytypes. Figure 0.2 depicts the atomic structure of monolayer TMDC in three distinct intralayer polytypes: hexagonal (H), octahedral (T) and distorted octahedral (T') phases. Based on the atom size and the involved orbitals in constructing the crystal, the energetic favorable phase for different types of TMDCs can be various. The H phase is the most common semiconducting phase in TMDCs except WTe_2 T' phase is energy favorable for WTe_2 but a metastable phase for others [2]. T phase is in general an unstable phase but can be engineered by chemical charge doping [3].

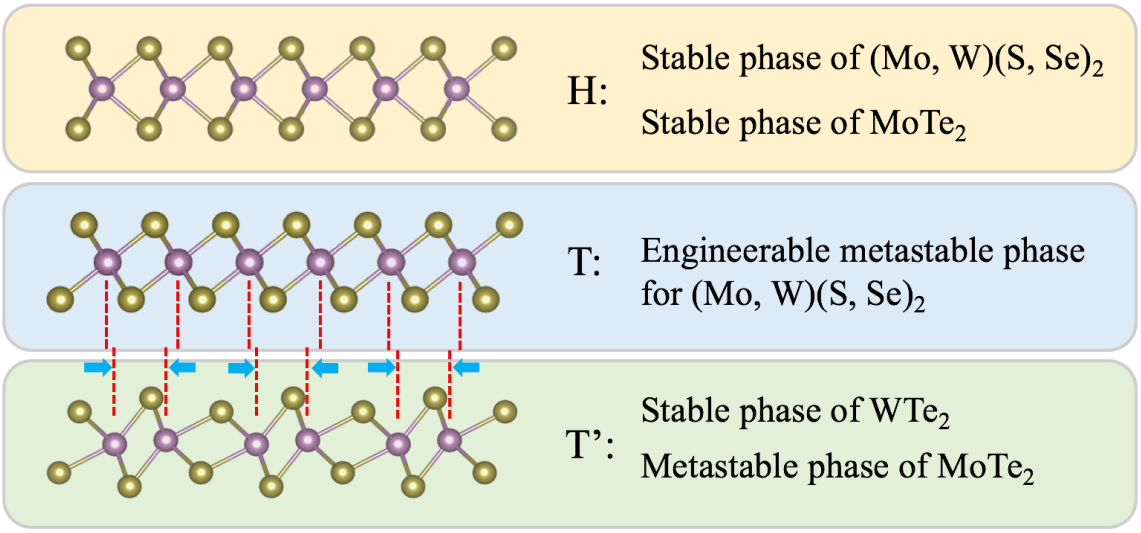

Figure 0.2: The schematics of 1L hexagonal (H), octahedral (T), and distorted octahedral (T')-TMDCs.

In addition to the intralayer polytypes, 2D-TMDCs possess rich interlayer polytypes through a variety of van der Waals stacking, i.e. unit layers may stack in various orders to achieve distinct stable/metastable phases [4]. Although the interlayer van der Waals interaction is much weaker than the intralayer covalent bonding, the different stacking orders may induce the change of crystal symmetry, dielectric environment and Coulomb interactions which are crucial in mediating in the physical properties of materials [5–7]. As a representative example, H-TMDC undergoes an electronic band transition from the direct-bandgap (1L H-TMDC) to indirect-bandgap semiconductor (few-layer and bulk H-TMDC). This has been demonstrated by seeing the dramatically enhancement of quantum efficiency in photoluminescence measurements [8,9]. Furthermore, the phase transition between polytypes may involve inversion symmetry breaking which is critical in studying valley-spin coupling [10–12], the valley-Hall effect [10,13] and the Weyl fermion in Type-II semimetals [14]. A systematic study on the polymorphism of TMDC is thus crucial to realize those physics as well as the further applications such as the valleytronics [15] which will be addressed in the next section.

1.2 The Tightly Bound Quantized Excitons in H-TMDCs

Exciton is a two-particle excitation in semiconductor with one electron and one hole (absent of electron) bound by Coulomb interaction. In conventional 3D semiconductors, the exciton emission can only be observed in the cryogenic temperature due the tiny binding energy (10 meV in silicon and 2.7 meV in germanium [16]), as a direct consequence of strong dielectric screening. In contrast, the dielectric screening

effect from material is strongly suppressed in atomically thin 2D H-TMDCs, enabling the observation of excitons even at room temperature. The giant binding energies of exciton in 2D H-TMDCs thus provide a promising platform to investigate the Coulomb interaction.

Experimentally, however, the assignment of binding energy is still under debate. It is because the emissions from band edge is strongly suppressed so that it fails to directly probe the binding energy of exciton by optical spectroscopy. As an alternative, it has been demonstrated by detecting of the quantized Rydberg states of exciton to estimate the binding energy of the ground state exciton [17–19]. In addition, the bare bandgap energy has also been measured by scanning tunneling microscopy [20], although the values are deviated from the ones derived from spectroscopy measurements. The accurate measurement of these quantized excitonic states is crucial to investigate the binding energy as well as the other Coulomb interaction mediated many-body correlation in 2D-TMDCs.

Another interesting property of H-TMDCs is the strong spin–orbit coupling (SOC) which is originated from the *d* orbitals in transition metal, leading to a large spin splitting for the valence band [21]. In 1L H-TMDCs, the splitting of valance band is about 150 meV for 1L-Mo(S, Se)$_2$ and 450 meV for 1L-W(S, Se)$_2$; while the splitting in conduction band is relatively small, ranging from 10 to 30 meV. In addition, due the presence of inversion symmetry breaking in 1L H-TMDC, the K and K' valleys become a time reversal pair, addressing the new valley degree of freedom (DoF) [10]. As a direct consequence, the spin DoF in valence band near K and K' points are coupled to valley

DoF and develop a robust spin polarized states, as shown in spin-valley configurations in Figure 0.3.

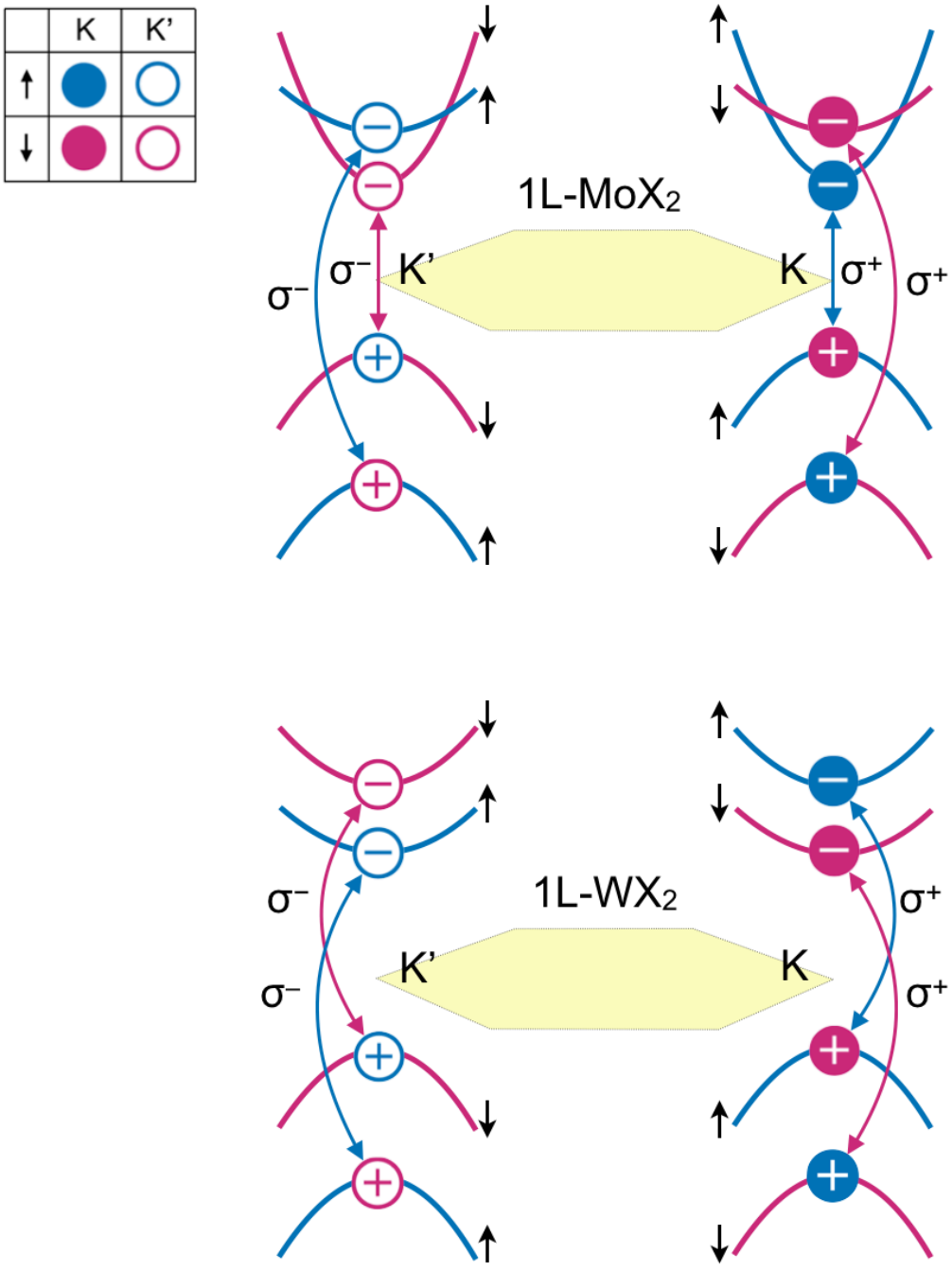

Figure 0.3: The schematic of spin-valley configurations of valence and conduction bands splitting near K and K' points in Brillouin zone. The top and bottom panel are corresponding to 1L-MoX_2 and WX_2, respectively.

As denoted in Figure 0.3, the spin-orbital coupling in conduction bands is distinct for 1L MoX_2 and WX_2, resulting in the dramatic difference in their optical properties. The abnormal SOC in 1L MoX_2 has been revealed from the theoretical calculation with three-band tight binding model [21]: the conduction band spin splitting (CBSS) is opposite in sign and the conduction band crossing in a small finite k, in contrast to 1L-WX_2. Experimentally, the spin-orbit splitting energies are confirmed by measuring the PL emission from the dipole forbidden PL emission from the dark excitons with opposite spins. This has been demonstrated by various methods, such as measuring the PL emission with the presence of in-plane magnetic fields [22], by coupling the exciton to the surface plasmon polaritons [23], or by detecting with a finite outgoing angles [24]. The experimental results reveal that the CBSS is about 40 meV [22–25] for 1L-WSe_2 and 47 meV [26] for 1L-WS_2 while the CBSS is –2 meV for 1L-$MoSe_2$, substantiating the theoretical frameworks.

The unique spin-valley configurations of 1L-WX_2 open a window to investigate the many-body correlation in the 2D excitonic system. Specifically, the ground state free exciton in 1L-WX_2 comes from the lower conduction band and the top valence band, which is not dipole allowed transition (so it is named dark exciton). As a result, the dark exciton is highly populated in the system with longer lifetime than bright exciton at the cryogenic temperature. The dark exciton in the system thus may interact with the bright exciton through the Coulomb exchange interaction, providing an outstanding platform for studying the intriguing many body interactions. This motivates our study of intervalley biexciton and exciton-trion in Chapter 6 and Chapter 9.

1.3 Outline

In Chapter 1, we briefly introduce the background of the 2D-TMDCs. Recent progress on the electrical and optical properties of atomically thin TMDC declare several interesting physics in the monolayer limits, which motivate the works presented in this dissertation. Chapter 2 describes the experimental methods. In section 2.1, we introduce the fabrication procedures of making ultrahigh quality 2D heterostructures. In section 2.2, we illustrate the experimental setup of polarization resolved PL/Raman spectroscopy with several different configurations. Section 2.3 introduces the experimental setup of the magneto-optical measurements carried out in our lab as well as in the National High Magnetic Field Laboratory(NHMFL) in Tallahassee, Florida.

Chapters 3 to 5 are composed as the first part of the dissertation: Investigation on the polymorphisms of atomic layered TMDCs by employing the polarization-resolved Raman spectroscopy. In Chapter 3, we focus on the five prototypical semiconducting TMDCs including H-MoS_2, H-WS_2, H-$MoSe_2$, H-WSe_2 and H-$MoTe_2$. Employing crystal symmetry analysis, we find a generic classification of the optical phonons of H-TMDCs into six stereotypes. Assisted by Raman tensor calculation, we demonstrate that the energies of these six type optical phonons is sensitive to the structural change, enabling us to characterize the symmetry and the number of layer of H-TMDCs [27,28].

In Chapter 4, we turn to the polymorphism studies of bulk $MoTe_2$ in distorted octahedral (T') phase. We present the Raman signatures of the temperature induced phase transition from monoclinic to orthorhombic phase in bulk T'-$MoTe_2$, which is essentially a reflection of the phase-transition-driven inversion symmetry breaking of crystal [29]. In Chapter 5, we investigate the Raman signature of the high quality T'-(Mo, W)Te_2

crystal down to the monolayer limit. The hBN/graphene covered/encapsulated 1L T'-TMDC crystal exhibits superb stability and ultrahigh crystal quality. Moreover, we employ Raman scattering to *in situ* monitor the crystal quality of atomic layered T'-$MoTe_2$ by watching the relative intensity of defect activated extrinsic peaks at 128 and 141 cm^{-1} [30].

Chapters 6 to 9 are composed as the second part of the dissertation: Investigation on the many-body correlation of the tightly Coulomb bound exciton in high quality 1L-WSe_2. In Chapter 6, we reveal the excitonic emission features with narrow linewidth in the high quality hBN/1L-WSe_2/hBN heterostructure [31]. Of the most interests is we observed the abnormally large and negative valley polarization of the biexciton and exciton-trion. Consequently, the results reveal the significant roles of dark exciton in 1L-WSe_2. In Chapter 7, we carry out the finding of the luminescent emission up to 4*s* excitons of 1L-WSe_2 in high magnetic fields. By analyzing the diamagnetic and Zeeman shift, we further point out the nontrivial differences of magnetic dipole moment between these Rydberg exciton states, as a direct consequence of the finite momentum distributions. Chapter 8 focus on the *2s* exciton luminescence which can be observed up to room temperature. By comparing the valley polarization and coherence of *1s* and *2s* exciton, we reveal that the electron-hole exchange interaction plays a significant role governing the intervalley depolarization and decoherence. In Chapter 9, we introduce the preliminary results on the low energy bound state with the time-resolved spectroscopy. The ultralong lifetime as well as the other optical properties pave the way to investigate the exciton condensation in atomic layered materials. At last, concluding remarks of the dissertation are given in Chapter 10.

CHAPTER 2

METHODOLOGY

2.1 Fabrication of High Quality 2D-TMDCs Sample

2.1.1 Pre-stacking Preparation

The substrate we typical used is a commercially available SiO_2(280nm)/p-Si wafer. The SiO_2/Si wafer is first cut in a proper size and ultrasonically cleaned with acetone/IPA/water for 5 minutes in sequence. These steps can largely remove hydrocarbon contamination and dust on the surface. After solvent cleaning, we further anneal the substrates at 1000℃ in argon ambient for at least 10 minutes to remove the small molecules such as water and oxygen absorbed on the surface and the nanoporous structure in SiO_2. Thermal annealing is essential for preparation of the air sensitive 2D-mateirals such as atomic-layered *T*'-TMDC to avoid reacting with the outgassing molecules.

We prepare the bulk crystals of 2D-TMDCs by Chemical Vapor Transport (CVT) method [29,31,32]. The grown bulk crystal is then exfoliated several times by Scotch tape and attached to the substrate immediately. We inspect the sample with a reflective optical microscope in the glovebox. After peeling off the tape, the flakes are first inspected and identified by the optical contrast. This method was firstly demonstrated with graphene [33,34] yet has been widely applied in inspecting other atomically-thin 2D materials [35,36]. Figure 0.1a shows the optical micrographs of atomic layered H-MoS_2 exfoliated on a SiO_2(300nm)/Si substrates. The optical contrast can be seen from dimmer to brighter associated to 1L to 5L H-MoS_2.

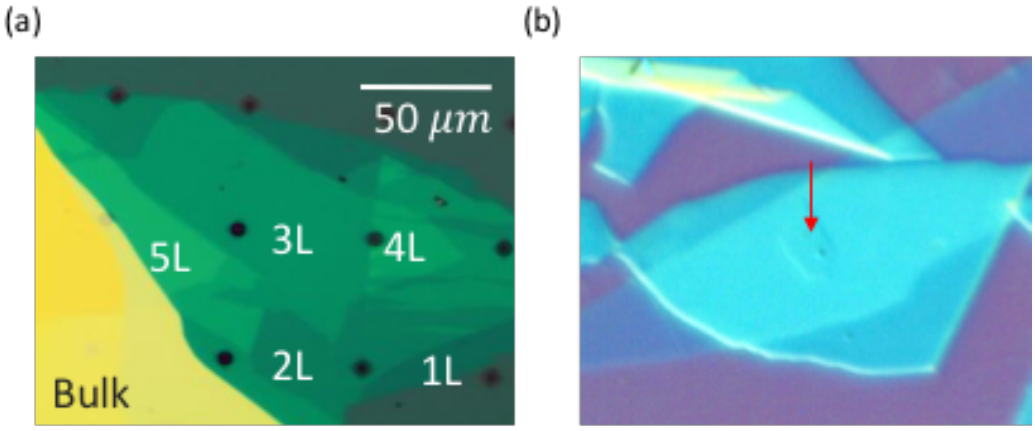

Figure 0.1: (a) The optical micrograph of exfoliated atomic layered MoS_2 from 1L to 5L on SiO_2/Si substrates. (b) The DIC micrograph of atomic-thickness hBN/1L-WSe_2/hBN heterostructures. The red arrow points out the sandwiched flake and the trapped bubble.

We further use differential interference contrast (DIC) microscopy and atomic force microscopy to further confirm the morphology and cleanness of samples. Figure 0.1b demonstrates a DIC micrograph of a heterostructure made by stacking of three 2D materials: hBN/1L-WSe_2/hBN. As can be seen, we can clearly locate the sandwiched flakes and the trapped bubbles by enhancing the contrast of edges.

2.1.2 Polymer-based Dry Transfer Technique

To make high quality sample, we further passivate samples to protect it from reacting with air. The state-of-the-art technology of passivation is sandwiching the target material with a couple of single crystal hexagonal boron nitride (hBN) thin flakes. The single crystal hBN provides an inert surface (negligible surface dangling bonds) to reduce the accidently chemical reaction and doping from the ambient. In addition, the surface of hBN flakes has been measured as atomically flat (the roughness is about 1Å [37]),

assuring that the materials can be well supported with the minimum morphology changes. To achieve that, we use the polymer based dry transfer technique to make 2D heterostructures, similar to the method published in literatures [38]. In Figure 0.2, we demonstrate the procedure of making a heterostructure of hBN/1L-WSe_2/hBN. Firstly, the PPC thin film is prepared by dropping the 8% polypropylene carbonate (PPC, Sigma-Aldrich 389021)/chloroform solution on a bare SiO_2/Si substrate. We then make a transparent double-side tape (3M^{TM}, VHB^{TM} #4910) stamp and transfer the PPC film on top of it. During the transfer processes, the PPC layer provides stronger stickiness than the van der Waals forces between the flakes and substrates, enabling us to pick up a few layer hBN flakes. After the top hBN flake pickup, we can directly use this hBN flake to continue picking up 1L-WSe_2 and another hBN flake sequentially. The last step is dropping the hBN/1L-WSe_2/hBN staking done to the target substrates.

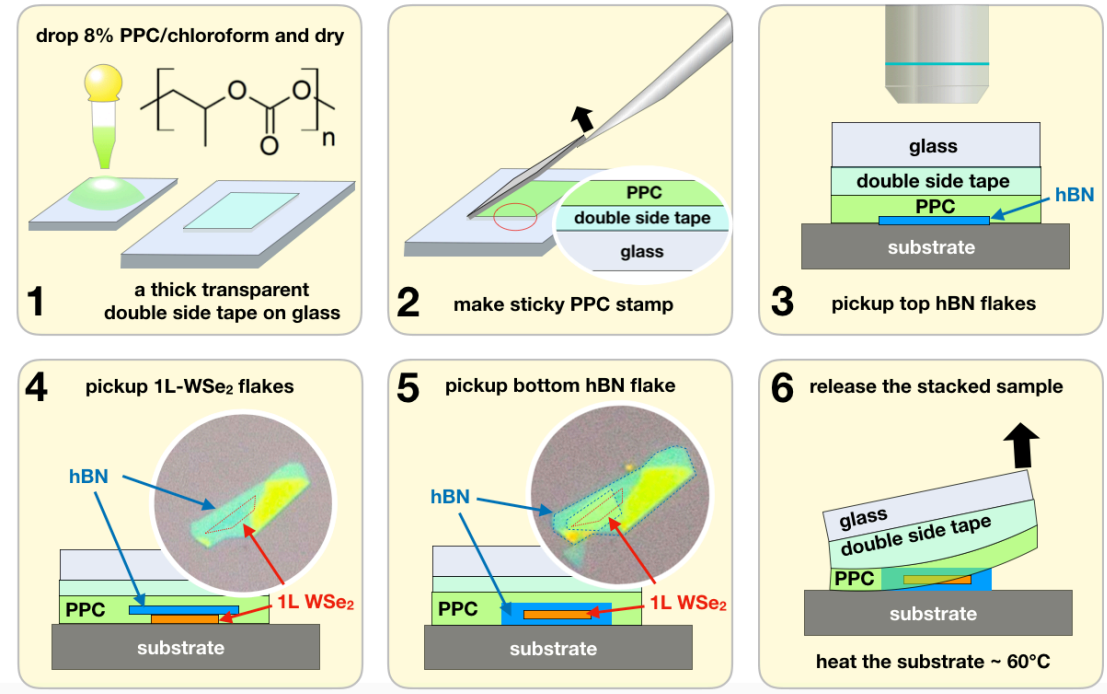

Figure 0.2: The schematic of polymer based dry transfer technology.

Figure 0.3 illustrates the setup of the polymer-based dry transfer which is composed of an upright microscope, a sample stage and a stamp manipulator. On sample stage, we further integrate thermoelectric Peltier heater to fine tune the sample temperature. We note that the precise control of temperature is critical for the successful transferring. Therefore, optimizing the temperature can greatly enhance the yield of successful pickup. In our setup, contrary to the conventional ceramic heater, thermoelectric Peltier device can actively transport the heat from one side to another side, enabling us to stabilize the temperature by a PID feedback control.

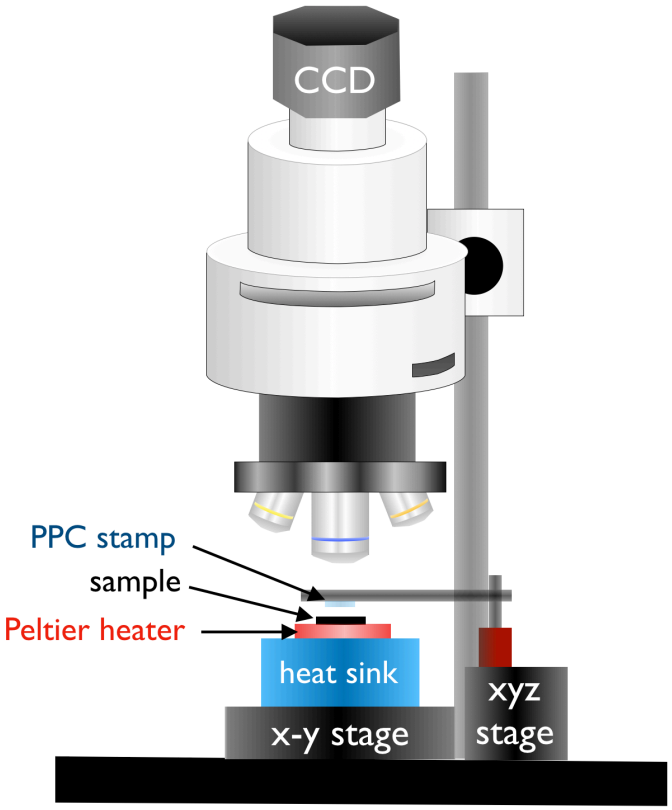

Figure 0.3: The experimental setup of the polymer-based dry transfer.

In Figure 0.4, we give the procedure of typical temperature settings for a round of pickup. We start with lowering the stamp until barely touching to the sample. At this moment, we slowly heat the sample up to 30 ℃ in a rate about 1 ℃/mins, enabling the smooth engagement. This step is crucial to reduce flake folding and bubble trapping. Once the stamp and sample have been fully contacted, we gently press the stamp down and raise the temperature to 40 ℃ and wait for 10 minutes. For picking the flake up, we cool the sample down to the pick-up temperature and lift the stamp quickly. We found that setting temperature at 30 ℃ achieves the best yield. After finishing several rounds of pickup, we drop the whole stacking down to the target substrate and heat the sample up to 60 ℃ to release the PPC.

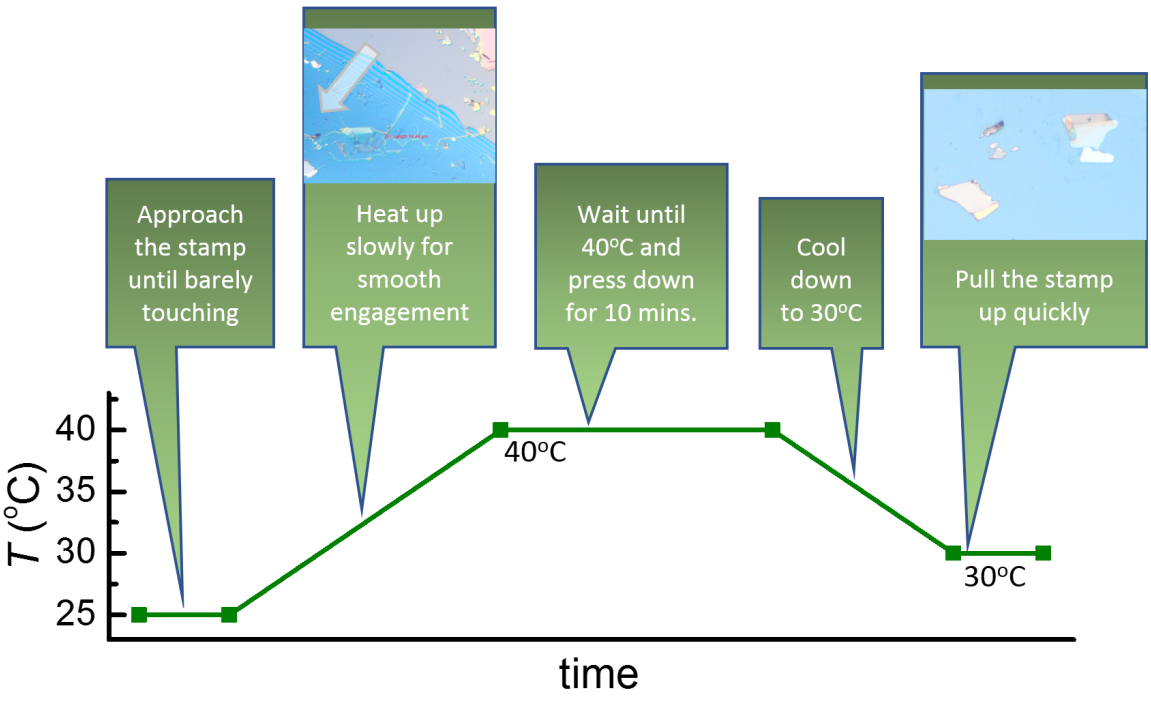

Figure 0.4: The temperature setting and procedure of a complete pickup.

2.1.3 Post-stacking Treatment

After stacking, the sample is further annealed to remove the residue from tape and PPC. Figure 0.5 shows the optical micrograph before and after thermal annealing at 350 ℃ for 1 hour. As can be seen the residue on both substrate and hBN flakes has been largely removed. In addition, we note that the annealing treatment can improve the sample quality. In general, we observed the linewidth narrowing of PL emission as well as the suppression of defect activated modes in 1L-WSe_2 sample, as carried out in Chapter 6 and Chapter 9.

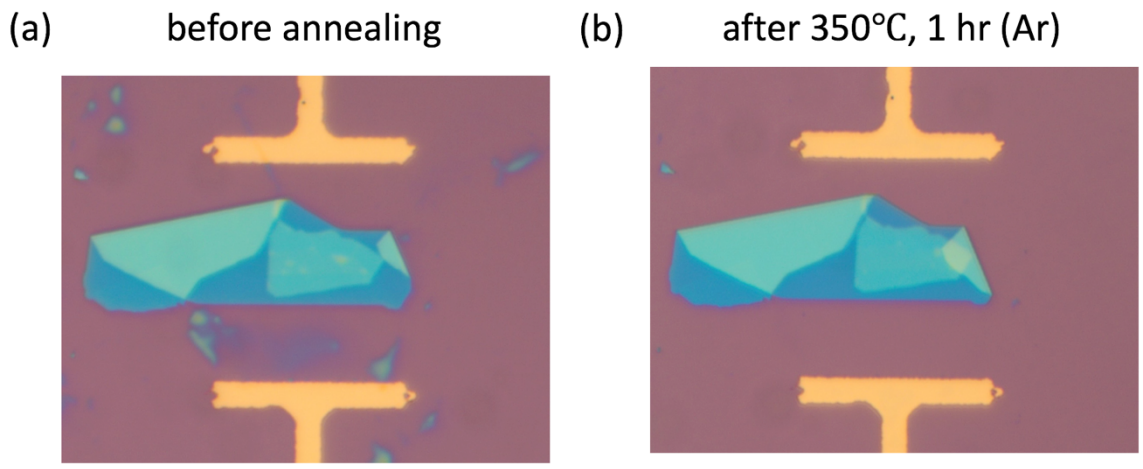

Figure 0.5: Optical micrograph of hBN/1L-WSe_2/hBN stacking (a) before and (b) after thermal annealing at 350℃ for 1 hour. The residue on substrate and hBN flakes has been effectively removed after annealing.

2.2 Polarization-resolved Raman/PL Spectroscopy

2.2.1 Introduction of Raman Scattering

Raman scattering has been widely used to probe the vibrational, rotational, and other low-frequency phonons in material. As one of the inelastic light scattering processes, the incident photons may loss or acquire the energy associated with the quantized excitations. Figure 0.6 illustrates the Stokes and anti-Stokes Raman scattering in term of photon energy. The energy of the excitation laser is E_{in}. The Stokes/anti-Stokes Raman scattering loss/gain the energy of E_{ph} which reflects the material properties. The final photon energy $E_o = E_{in} \pm E_{ph}$ obeys the energy conservation law and can be directly measured by a spectrometer. In addition to energy conservation, a valid Raman process obeys momentum conservation law. The momentum conservation ensures the total momentum of quantized excitations is zero. For first-order Raman scattering (involves only one phonon), the phonon is required to be zero momentum, zone-center phonon (the normal modes). High-order Raman scattering may involve the multiple phonons with various combination in momentum. For example, the 2D band in graphene involves two finite-k phonons which scattered the electron back and force between two valleys [39].

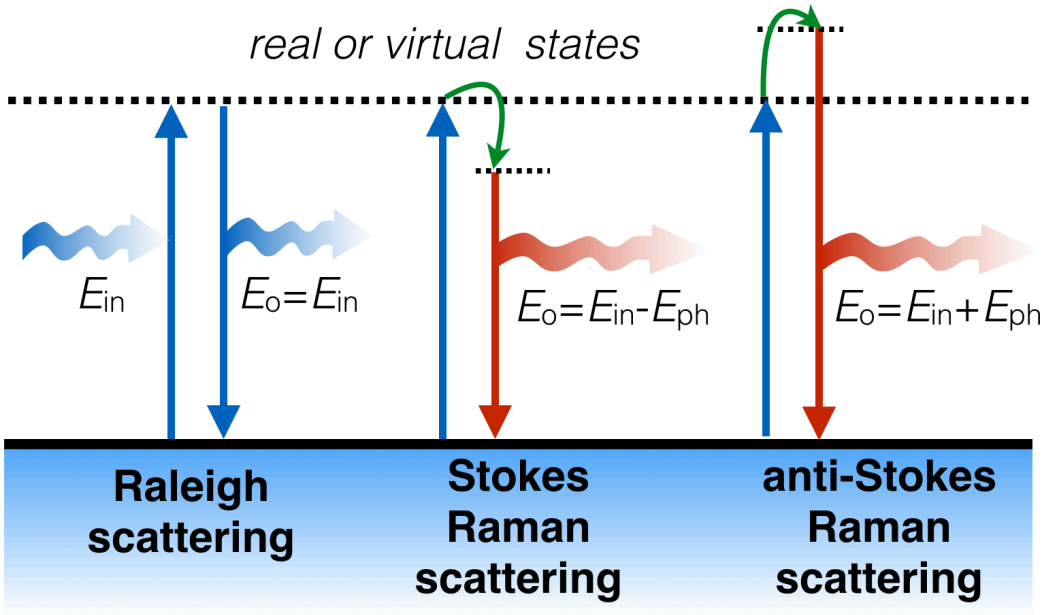

Figure 0.6: The schematics of Raleigh, Stokes and anti-Stokes Raman scattering processes.

2.2.2 Experimental Setup for Measuring Low-wavenumber Inelastic Scattering

Figure 0.7 illustrates the optical spectroscopy designed for measuring the Raman/PL spectra down to 5 cm^{-1} from the sample with micrometer size. It is composed of light sources(laser), a line filtering system, a microscope, and a spectrometer. Briefly, the laser is first cleaned by a spectral filtering system and guided through a beamsplitter and then a homemade microscope which is configured in the back-scattering geometry. The excitation laser is focused on the sample by a high NA objective lens to achieve the sub-micrometer spot size. The scattered light or luminescence from sample are then collected with the same objective lens, filtered by notch filters, dispersed by a spectrometer, and finally detected by a liquid nitrogen cooled charge-coupled device (CCD).

In our setup, we employ both single wavelength laser and tunable laser, including argon ion laser (including several lines at 476nm, 488nm, 496 nm, 514nm), DPSS Nd:YAG laser (532nm), diode laser (405 nm), dye laser and Ti:Sapphire laser. The wavelength coverage of dye laser depends on the selected dye. In our system, we can achieve the wavelength range by switching two different dyes: 560–640nm for RG6; and 615–674 nm for DCM. For Ti:Sapphire laser, the wavelength range is 708–970 nm. These tunable lasers cover the range of the 1*s* exciton emission of the H-TMDC (except H-$MoTe_2$), enabling us to perform the resonant excitation and emission to investigate the light-matter interactions.

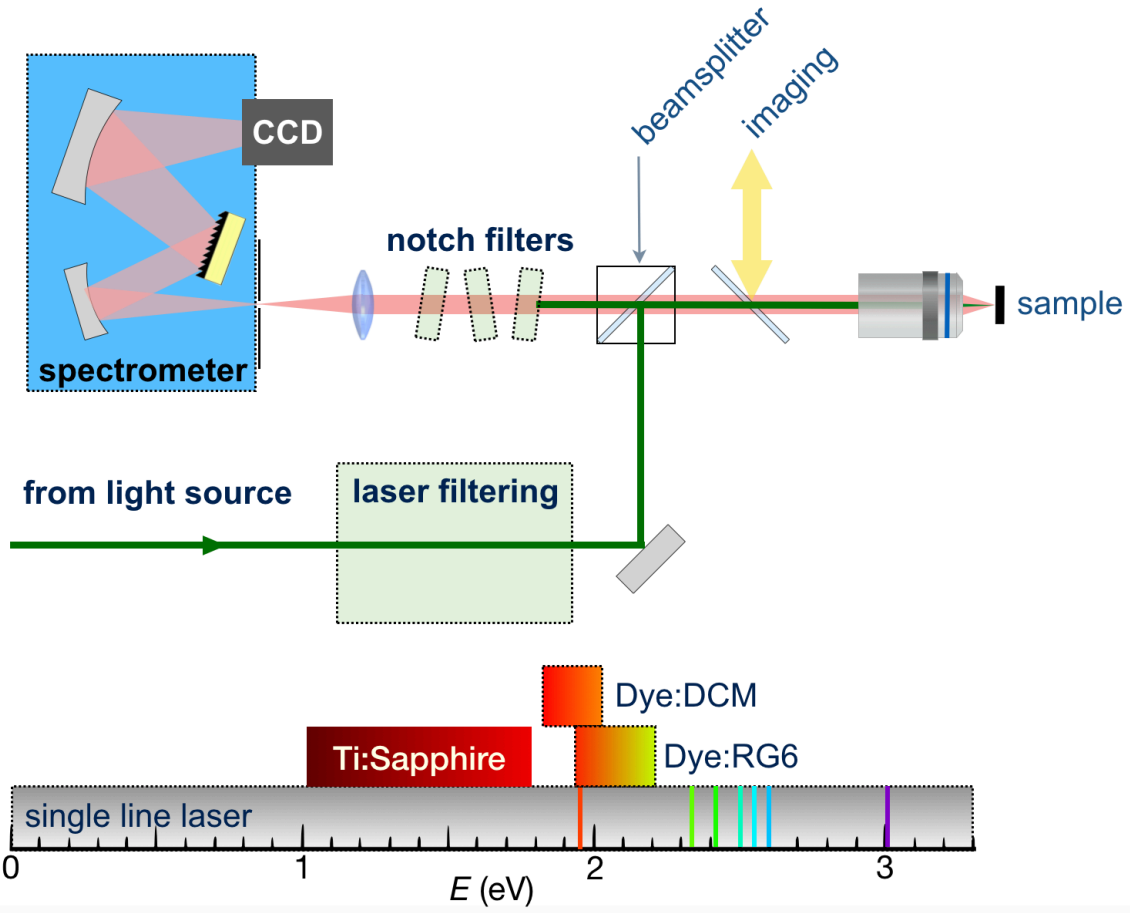

Figure 0.7: Optical setup for low-wavenumber micron-Raman/PL spectroscopy.

To perform the low wavenumber inelastic light scattering spectroscopy, a spectral clean and sharp laser line filter and an ultra-narrow notch/edge filter is required for the employed laser wavelength. For single wavelength laser, it's relative easy to achieve this by using the-state-of-the-art Bragg filters (BragGrate™) which provides both laser line and notch filtering down to 5 cm^{-1} for the selected wavelengths. However, for tunable laser, we build a homemade tunable laser line filter system to clean the laser. Figure 0.8a displays the 4f-optical setup integrated with 2 holographic gratings, which delivers the best filtering performance. In Figure 0.8b, we show the spectra of a supercontinuum laser before and after spectral filtering with the designed bandwidth about 0.15 nm. We further confirm the performance of stray light rejection in our filtering system. In Figure 0.8c, we further compare the stray light rejection performance of different setups. As can be seen, our 2-grating system delivers the cutting edge of the laser line less than 50 cm^{-1}, significantly better than the filtering system equipped only 1 grating.

For the collection, a triple stage spectrometer (Horiba T64000) is required to provide the best capability of Rayleigh scattering rejection. The first two stages are configured in the subtractive modes, acting like a tunable edge filter to reject the Rayleigh scattered photons. After cutting laser light, the signal can be analyzed by a spectrograph in the third stage.

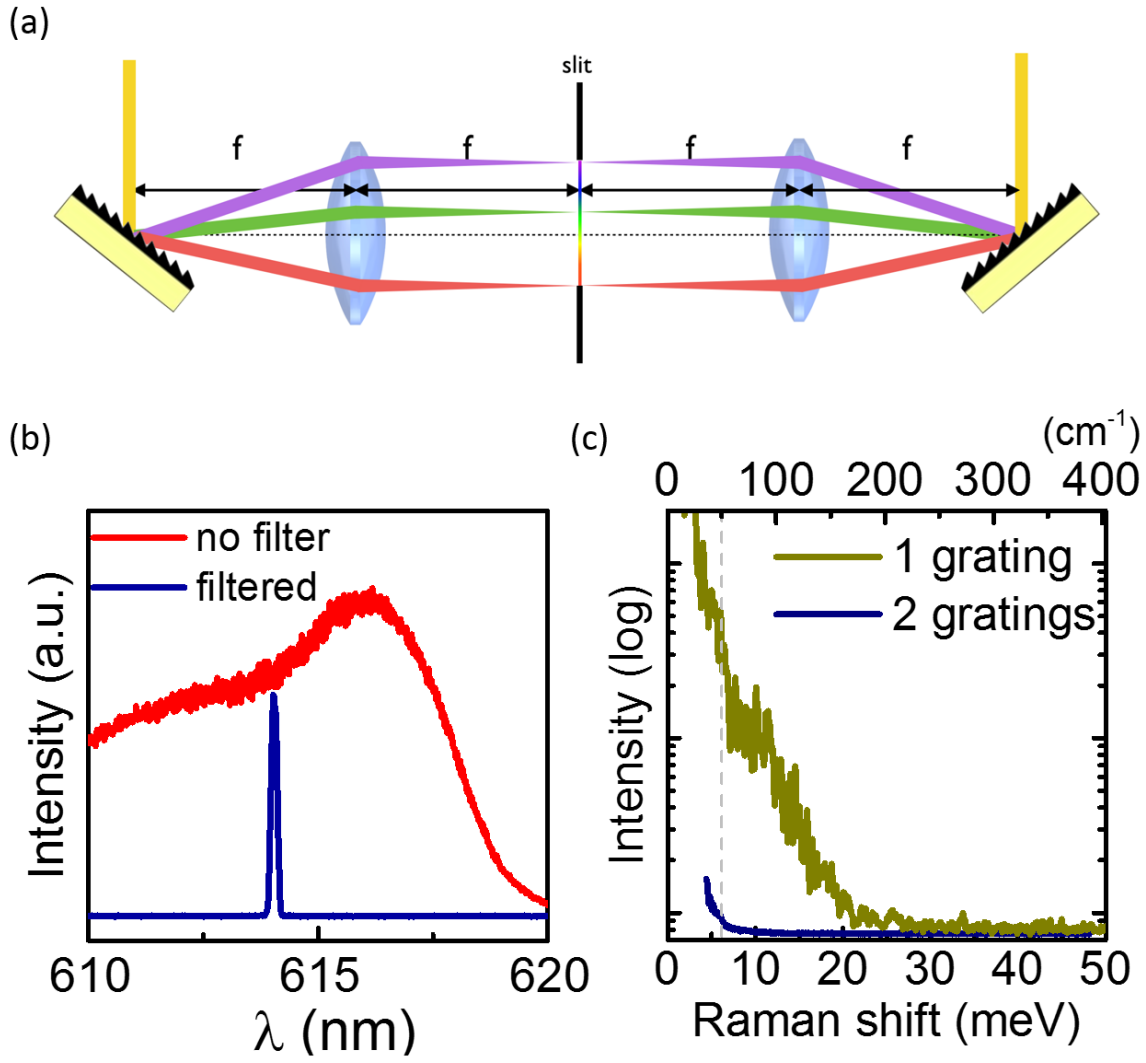

Figure 0.8: (a) Optical setup for the 2-grating laser line filter configured with a 4f optical relay system. (b) Comparison of the original broadband light sources with a filtered spectrum. (c) Comparison of the stray light rejection performance of 1-grating and 2-grating spectral filtering system.

2.2.3 Experimental Setup of Polarization-resolved Spectroscopy

We introduce several linear polarizers and waveplates into our optical system to control and analyze the polarization. Figure 0.9 illustrates three different configurations of polarization-resolved spectroscopy we used in the following chapters. Figure 0.9a is the schematic of the linear polarization resolved spectroscopy demonstrated in Chapter 4 and 5. In this configuration, the sample is excited by a linear polarized light with the controlled polarization direction relative to the crystal principle axis θ_i The direction of incident light polarization can be rotated by a half waveplate in between BS and objective lens. The back-scattered signal is analyzed by another set of half-wave plate and a linear polarizer after BS. Figure 0.9b shows the setup employed in Chapter 3 and 8. We excite sample with σ^- polarized light and detect the σ^- and σ^+ polarized light in the signal. To achieve that, we place a broadband quarter waveplate (Fresnel Rhomb) after BS to transform the incident linear polarized light into σ^- polarized light. For collection, we use the same quarter waveplate to transform the σ^- and σ^+ signals back to the linear polarized light to minimize the polarization distortion caused by other optics. Figure 0.9c illustrates the optical setup employed in Chapter 6, 7 and 9. In this configuration, we excite sample with a linear polarized light and detect the σ^- and σ^+ circular polarized signals separately.

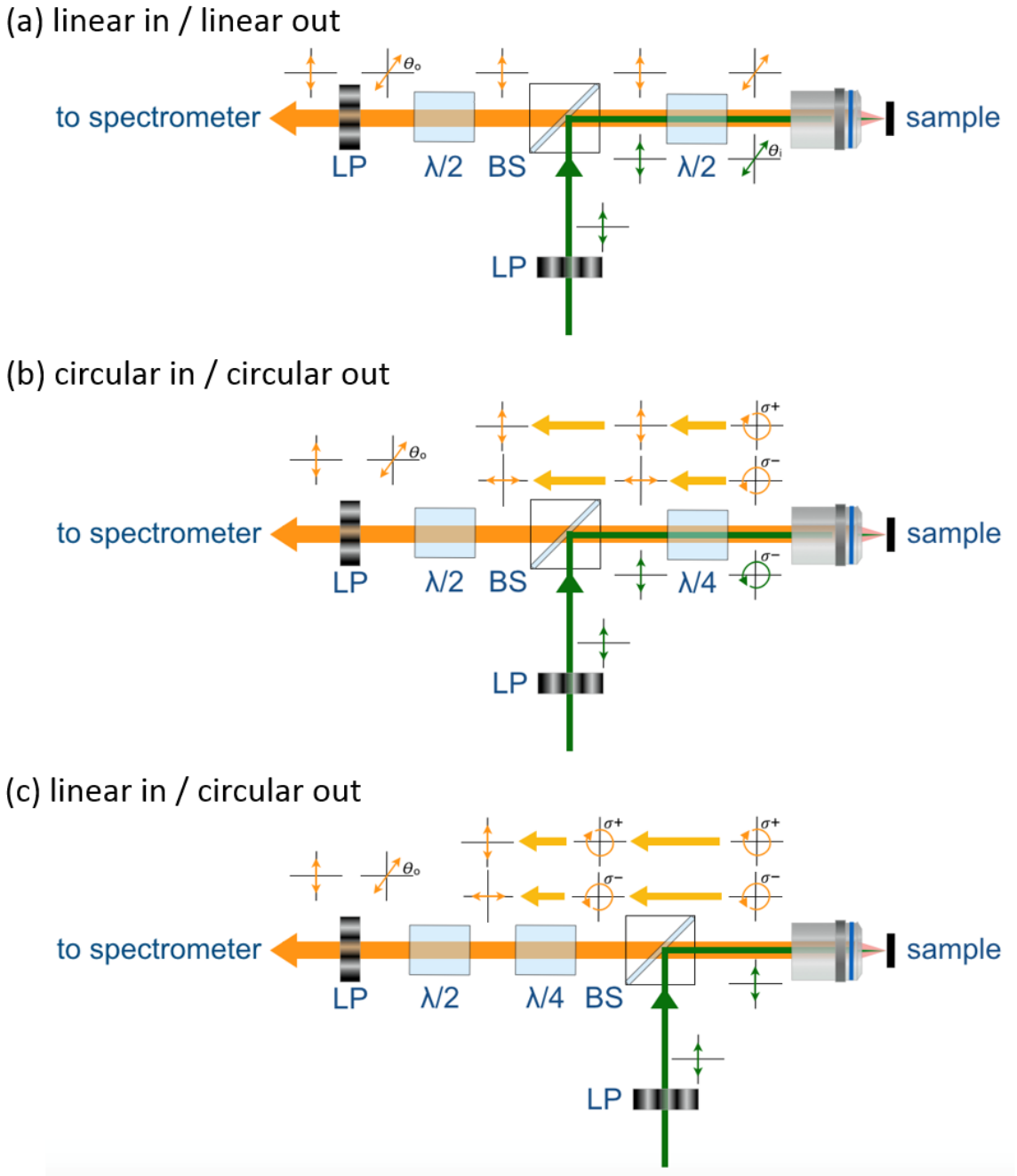

Figure 0.9: Three different experimental setups of polarization-resolved spectroscopy we used in (a) Chapter 4 and 5. (b) Chapter 3 and 8. (c) Chapter 6, 7 and 9, respectively.

2.3 Experimental Setup of Magneto-optical Spectroscopy

2.3.1 The Setup Integrating with 9T Superconducting Magnet.

To perform the spectroscopy in the high magnetic field, we further integrate a nonmagnetic cryostat with a 9T superconducting magnet in our lab. The magnet has a 2-inch room temperature bore, enabling us to integrate the polarization-resolved spectroscopy easily. We note the strong magnetic field can alter the properties of the optics. For example, the magnetic fields can induce the Faraday rotation in objective lens which must be considered and calibrated. In addition, the magnetic field may change the phase retardation of the waveplate, especially for Fresnel Rhomb due to the bulky material. To avoid that, we keep all optics except objective lens at least 3 feet away from the magnet bore in our setup.

2.3.2 Magneto-optical Spectroscopy Setup in NHMFL

To access the higher magnetic field than 9T, we also perform the polarization-resolved spectroscopy in the NHMFL in Tallahassee, Florida. We have accessed two different setups: the free-space helium bath cryostat integrating with a 17T superconducting magnet (SCM3) and a fiber based system in a Helium-3 cryostat integrating with a 31T resistive magnet (Cell 9). The optical setup for free-space is illustrated in Figure 0.10. In this setup, the sample is mounted on a 3-axis piezo stages. A nonmagnetic high NA objective lens is mounted on the probe and cooled down with the sample. This design improves the overall stability, enabling us to perform reliable measurements on the weak features from the 2*s* and 3*s* exciton emission in 1L-WSe_2. In 31T resistive magnet system, the huge magnetic fields as well as large amount of

vibrations from the cooling system make the free-space design very challenging. Instead, in this setup, all optics are carefully mounted on the probe, as illustrated in Figure 0.11. The excitation laser and signals are coupled through the fibers.

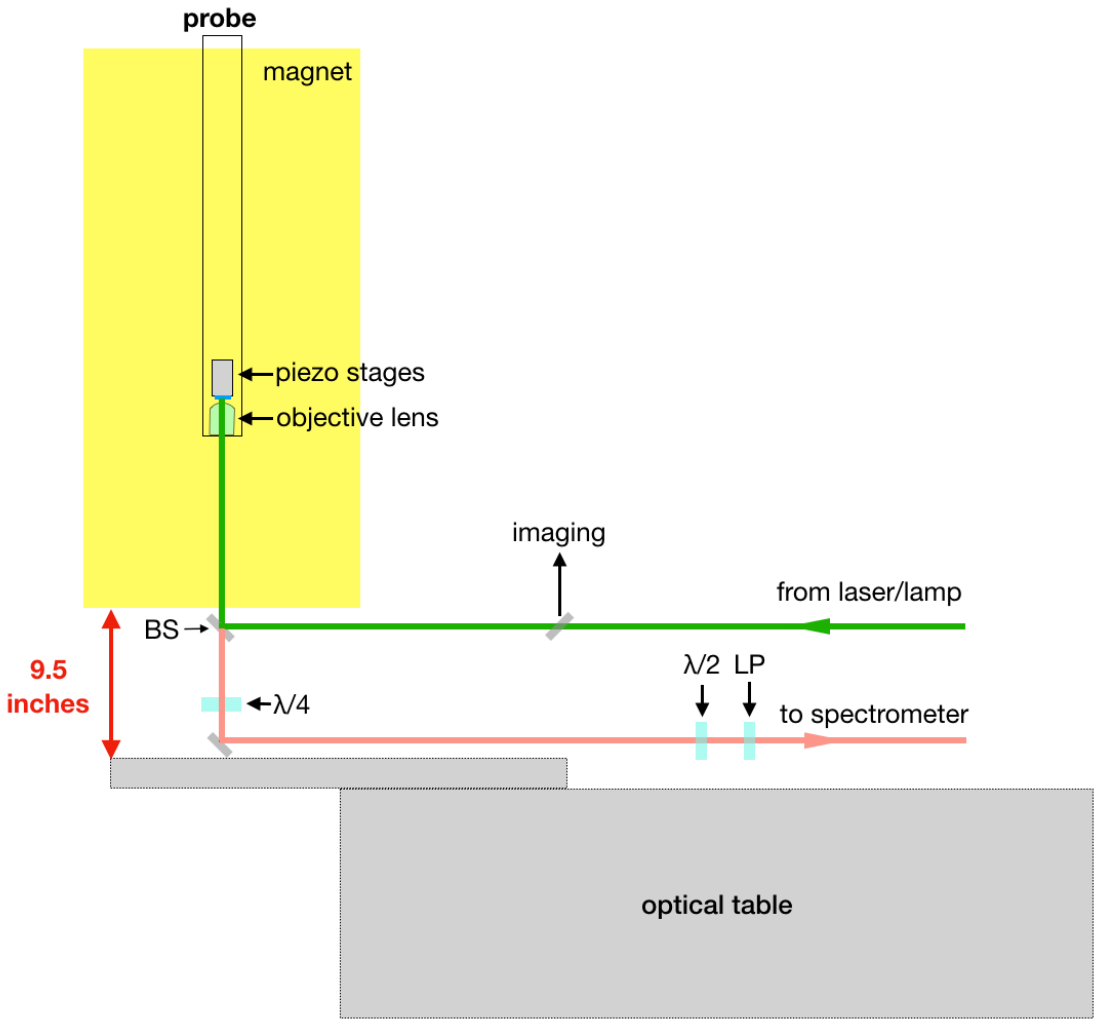

Figure 0.10: The free-space optical setup with 17T superconducting magnet (SCM3) in NHMFL.

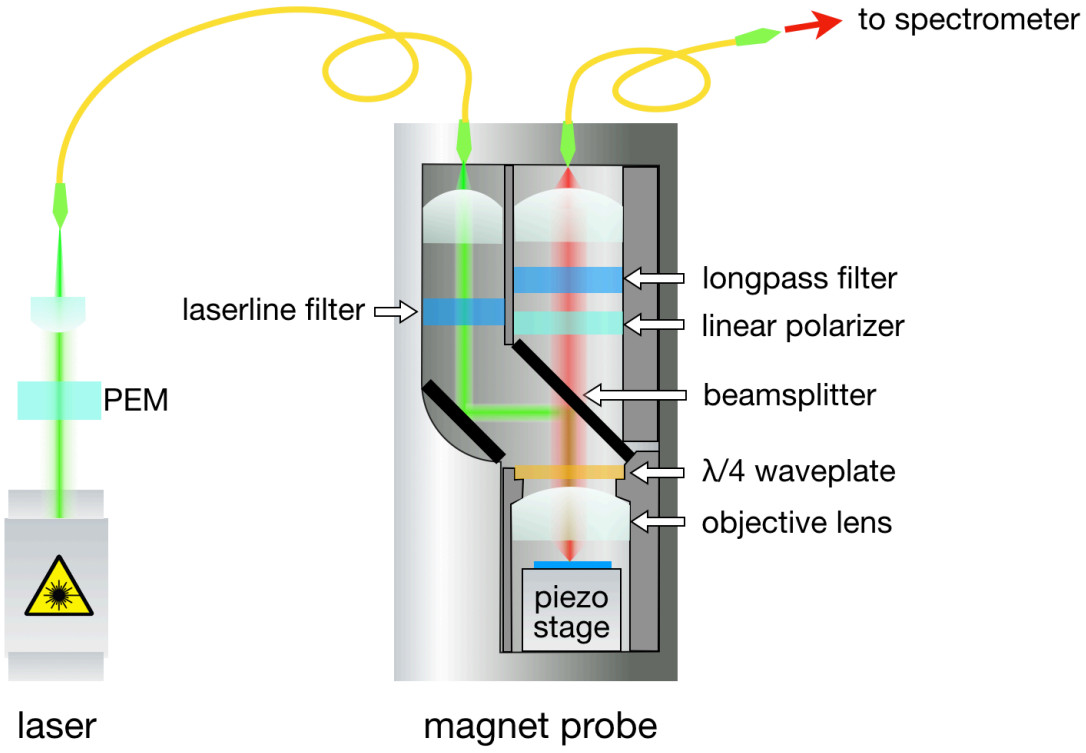

Figure 0.11: The fiber-based optical setup with 31T resistive magnet (Cell 9) in NHMFL.

CHAPTER 3

HELICITY-RESOLVED RAMAN SCATTERING OF H-TMDCS

3.1 Introduction

The study of polymorphism is to understand how the physical properties change with their atomic arrangement. In H-TMDCs, the electronic band structure is extremely sensitive to the number of layer in the monolayer limit: 1L H-MoS_2 is a direct bandgap material while 2L H-MoS_2 is an indirect bandgap material [8,9]. An accurate and reliable measurement to determine the number of layer is thus crucial when study the 2D materials in the atomic thickness level. The state-of-the-art microscopy can directly see the atomic arrangement, e.g. scanning tunneling microscope and transmission electron microscope. However, these measurements require specific sample preparation process and thus are limited in a few applications. Another conventional method to determine the number of layer is by measuring the thickness of flakes and then compare with the theoretical values from first principle calculation. Atomic force microscopy (AFM) has been widely used to measure the thickness of atomic layered material down to sub nm resolution. However, experimentally, determine the number of layer only by thickness measurement may misinterpret because of the uncertainty of the spacing between substrate and crystal [40] and the interlayer spacing in different stacking order polytypes [41]. In this chapter, we demonstrate that complementary to AFM, the helicity-resolved Raman spectroscopy enables us to determine the number of layer and stacking orders of H-TMDC unambiguously. Moreover, we discover that while some phonons maintain helicity from incident to emitted photon, others can switch it completely out.

This points out an important fact: Both σ^+ and σ^- photon can emit from K/K' valley in the nonresonant excitation, challenging the approximation in the core of the valleytronics: The σ^+/σ^- photons are only allowed to emit in K/K' valley. Our results consequently provide new insights into the relation between the photon helicity and valleytronics in semiconducting TMDCs.

3.2 Six Generic Types of Zone Center Phonon in Atomic Thickness H-TMDCs

Layered H-TMDCs have a graphite-like structure with each graphene sheet replaced with an X-M-X tri-atomic layer, where X is a chalcogen atom (S, Se, Te) and M is a transition metal atom (W, Mo). 1L-MX_2 has three atoms in its unit cell and their vibrations result in 9 normal modes, including 3 acoustic and 6 optical branches. Figure 0.1 illustrates the normal modes which can be further divided by two types: one is the vibration only involves the chalcogen atoms that includes 1 out-of-plane OC modes and 2 degenerated in-plane IC modes; another is the vibration of relative motion of transition metal and chalcogen atoms that includes 1 out-of-plane OMC modes and 2 degenerated in-plane IMC modes.

For multi-layer H-TMDC, the optical phonons within individual MX_2 layer couple to each other and create new normal modes. The energies of the new optical phonon modes are slightly shifted from the corresponding monolayer phonon due to the interlayer interactions. Similarly, the acoustic phonons of individual layers couple to each other and form new optical phonon branches, including the in-plane `shear' mode and the out-of-plane `breathing' mode (see Figure 0.2 for the shear and breathing modes AB

stacking [42] 2L-MX_2). These modes have relatively low energy less than 50 cm^{-1}, reflecting that the interlayer interactions are much weaker than the covalent bonding within each MX_2 layer. These six prototypical types of optical zone center phonons well describe all the peaks observed in the Raman spectra.

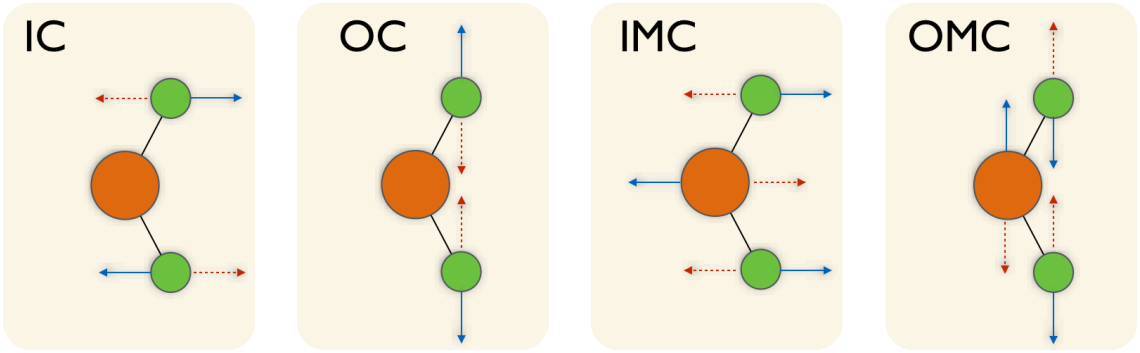

Figure 0.1: The schematic of four intralayer normal modes in 1L H-TMDC.

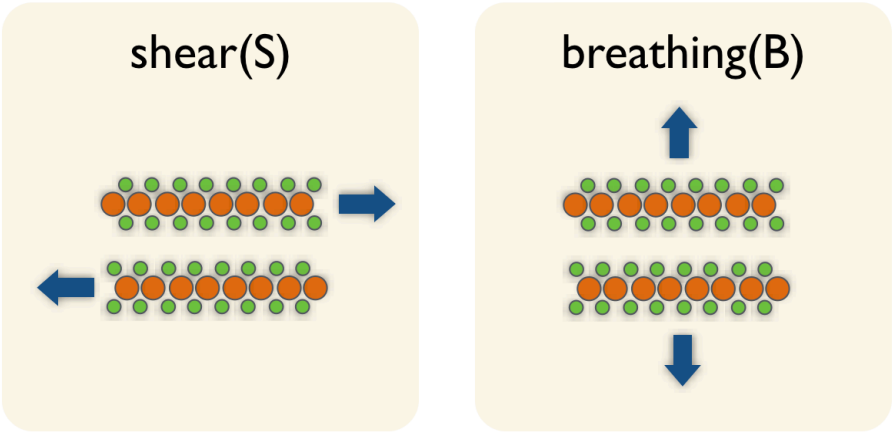

Figure 0.2: The schematic of shear and breathing modes of an AB stacking bilayer H-TMDC.

We further determine whether the optical phonon is Raman active by applying the transformation of irreducible representations based on the point group and symmetry of the crystal. Table 0.1 summarizes the irreducible representations for the six prototypical types of optical phonons. Monolayer H-TMDC is invariant under the 12 symmetry operations in the D_{3h} point group [42,43]. The IMC and OC modes belong to E' and $A_1{}'$ symmetry, respectively and both are Raman active. The IC and OMC modes belong to E'' and $A_2{}''$ symmetry, respectively and both are Raman inactive. Bilayer MoS_2 is symmetric under inversion and the symmetry operations form the D_{3d} point group. In multilayers, the optical phonons in Figure 0.1 couple to form symmetric modes (E_g for IC and IMC, A_{1g} for OC and OMC) and anti-symmetric modes (E_u for IC and IMC, A_{2u} for OC and OMC). Coupling of the acoustic phonons forms the even E_g shear mode and A_{1g} breathing mode (Figure 0.2). Going further, it turns out the symmetry point group is D_{3h} for all odd layers, and D_{3d} for all even layers. For bulk H-TMDC, the unit cell consists of 2 MX_2 units with 6 atoms, and the symmetry space group is the non-symmorphic D^4_{6h} ($P6_3/mmc$). The acoustic phonons are odd under inversion while the shear and breathing modes are even, and the IC, OC, IMC, and OMC each have one even and one odd. We note that in above discussion we only consider AB(2Hc) stacking, which is the most stable polytypes for H-TMDCs.

Table 0.1: Symmetry representations for phonon modes in bulk and few layer H-TMDCs

# of Layer	Sym. Grp.	σ_h / i Sym.*	acoustic		in-plane optical			out-of-plane optical		
			LA/TA	ZA	IC	IMC	S	OC	OMC	B
1	D_{3h}	+	E'	-	-	1 E'	-	1 A'_1	-	-
		–	-	A''_2	1 E''	-	-	-	1 A''_2	-
2	D_{3d}	+	-	-	1 E_g	1 E_g	1 E_g	1 A_{1g}	1 A_{1g}	1 A_{1g}
		–	E_u	A_{2u}	1 E_u	1 E_u	-	1 A_{2u}	1 A_{2u}	-
odd N	D_{3h}	+	E'	-	(N–1)/2 E'	(N+1)/2 E'	(N–1)/2 E'	(N+1)/2 A'_1	(N–1)/2 A'_1	(N–1)/2 A'_1
		–	-	A''_2	(N+1)/2 E''	(N–1)/2 E''	(N–1)/2 E''	(N–1)/2 A''_2	(N+1)/2 A''_2	(N–1)/2 A''_2
even N	D_{3d}	+	-	-	N/2 E_g	N/2 E_g	N/2 E_g	N/2 A_{1g}	N/2 A_{1g}	N/2 A_{1g}
		–	E_u	A_{2u}	N/2 E_u	N/2 E_u	(N–2)/2 E_u	N/2 A_{2u}	N/2 A_{2u}	(N–2)/2 A_{2u}
bulk	D^4_{6h}	+	-	-	1 E_{1g}	1 E_{2g}	1 E_{2g}	1 A_{1g}	1 B_{2g}	1 B_{2g}
		–	E_{1u}	A_{2u}	1 E_{2u}	1 E_{1u}	-	1 B_{1u}	1 A_{2u}	-

3.3 Polarization Selection Rules of Raman Modes in Atomic Layered H-TMDCs

In this section, we demonstrate the polarization-resolved Raman spectra of 2L H-$MoTe_2$ with various configurations. In Figure 0.3, four spectra are shown from top to bottom are colinear (HH: the excitation and the detected signal are in the same linear polarization), crosslinear (HV: the excitation and detected signal are in the perpendicular linear polarization), crosscircular (XC: the excitation laser is in σ^- but detected signal is in σ^+ circular polarization) and cocircular (CC: the excitation and detected signal are in σ^- circular polarization). As can be seen, the six prototypical phonon modes behave differently: The OC/OMC/breathing modes only show up in HH and CC configurations while IC/IMC/shear modes show up in HH, HV and XC configurations.

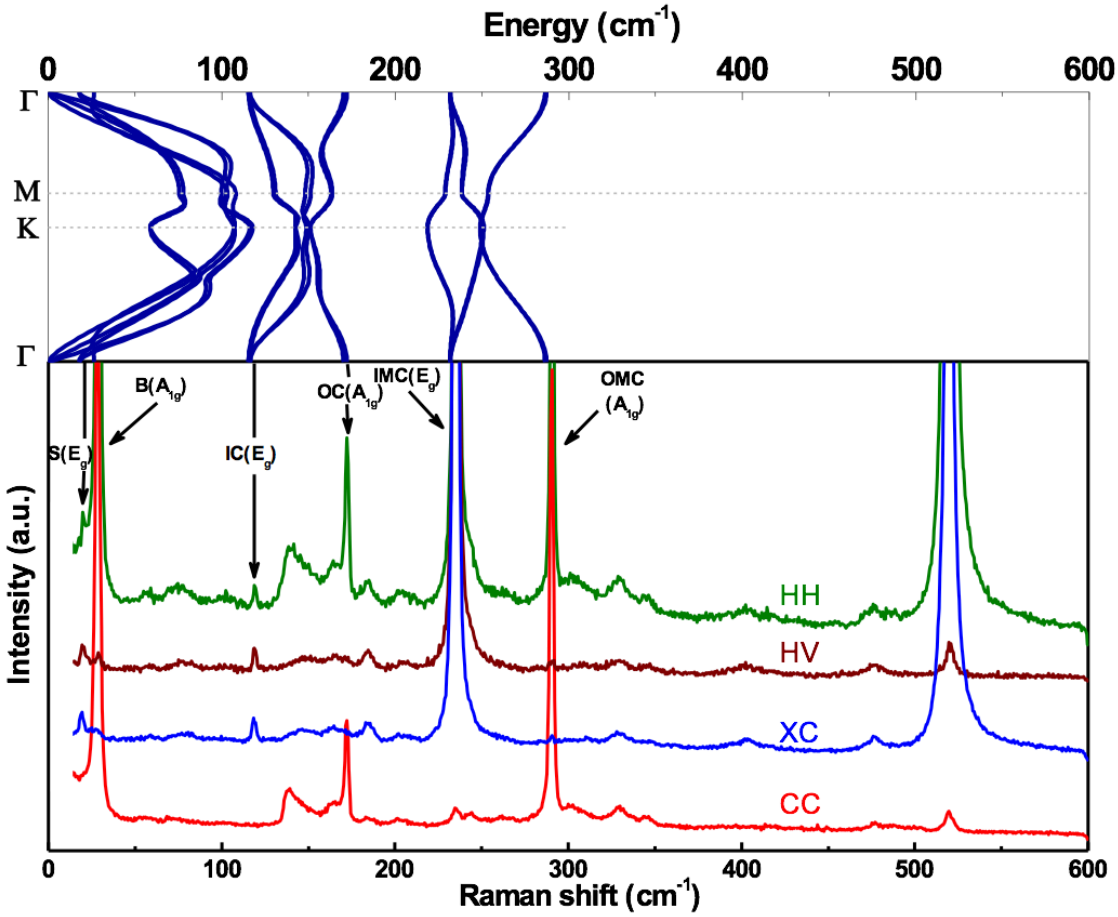

Figure 0.3: Polarization-resolved Raman spectra of 2L H-$MoTe_2$, matching well with the phonon dispersion acquired by DFT calculation.

The observed polarization dependence of Raman intensity is a direct consequence of the selection rule in Raman tensors, enable us to determine the phonon symmetry of each phonon mode. Briefly, in the nonresonant condition, the Raman cross section can be estimated by the equation given by

$$A\sum_{j=1}^{d}\left|\langle\varepsilon_o|R_j|\varepsilon_i\rangle\right|^2, \quad \text{(Eq. 3.1)}$$

where A is a scaling constant, R_j are tabulated Raman tensors, j is the index counting from 1 to the total degeneracy d, ε_i and ε_o are polarization states of the incoming and outgoing light [44]. The Raman tensor is related to the phonon symmetry and thus provide a route to identify the crystal symmetry. In addition, we summarize the Raman tensors of the normal modes of TMDC in Appendix A; the complete list can be found in Ref. [44].

For 2L H-$MoTe_2$, the OC/OMC/breathing modes we observed in Figure 0.3 are in A_{1g} symmetry; the IC, IMC and shear modes are in E_g symmetry. The corresponding Raman tensors are given as $\begin{bmatrix} a & 0 & 0 \\ 0 & a & 0 \\ 0 & 0 & b \end{bmatrix}$ for A_{1g}, and $\begin{bmatrix} f & 0 & 0 \\ 0 & -f & d \\ 0 & d & 0 \end{bmatrix}\begin{bmatrix} 0 & -f & -d \\ -f & 0 & 0 \\ -d & 0 & 0 \end{bmatrix}$ for E_g which is doubly degenerated.

In HH configuration, we assume $\varepsilon_i = \varepsilon_o = \begin{bmatrix} 1 \\ 0 \\ 0 \end{bmatrix}$, the intensity can be calculated straightforward as

$$\sum_{j=1}^{d}\left|\langle\varepsilon_o|A_{1g}|\varepsilon_i\rangle\right|^2 = a \text{ for OC/OMC/breathing modes;}$$

$$\sum_{j=1}^{d}\left|\langle\varepsilon_o|E_{g,j}|\varepsilon_i\rangle\right|^2 = f^2 + 0 = f^2 \text{ for IC/IMC/shear modes;}$$

In HV configuration, by assuming. $\varepsilon_i = \begin{bmatrix}1\\0\\0\end{bmatrix}$, $\varepsilon_o = \begin{bmatrix}0\\1\\0\end{bmatrix}$;

$$\sum_{j=1}^{d}\left|\langle\varepsilon_o|A_{1g}|\varepsilon_i\rangle\right|^2 = 0 \text{ for OC/OMC/breathing modes;}$$

$$\sum_{j=1}^{d}\left|\langle\varepsilon_o|E_{g,j}|\varepsilon_i\rangle\right|^2 = 0 + (-f)^2 = f^2 \text{ for IC/IMC/shear modes.}$$

In CC configuration, we assume the incident and outgoing light are in the same circular polarization, i.e. $\varepsilon_i = \varepsilon_o = \frac{1}{\sqrt{2}}\begin{bmatrix}1\\-i\\0\end{bmatrix}$;

$$\sum_{j=1}^{d}\left|\langle\varepsilon_o|A_{1g}|\varepsilon_i\rangle\right|^2 = a \text{ for OC/OMC/breathing modes;}$$

$$\sum_{j=1}^{d}\left|\langle\varepsilon_o|E_{g,j}|\varepsilon_i\rangle\right|^2 = f^2 + (fi)^2 = 0 \text{ for IC/IMC/shear modes.}$$

In XC configuration, $\varepsilon_i = \frac{1}{\sqrt{2}}\begin{bmatrix}1\\-i\\0\end{bmatrix}$ while $\varepsilon_o = \frac{1}{\sqrt{2}}\begin{bmatrix}1\\i\\0\end{bmatrix}$;

$$\sum_{j=1}^{d}\left|\langle\varepsilon_o|A_{1g}|\varepsilon_i\rangle\right|^2 = 0;$$

$$\sum_{j=1}^{d}\left|\langle\varepsilon_o|E_{g,j}|\varepsilon_i\rangle\right|^2 = \frac{1}{2}(f^2 - (fi)^2) = f^2.$$

The above calculations are consistent with the experimental results presented in Figure 0.3: The OC/OMC/Breathing modes only show up in HH and CC configurations while the IC/IMC/Shear modes only show up in HH, HV and XC configurations. The polarization selection rule can be further generalized by introducing θ and φ, the angles between the polarization of incident and outgoing light respected to the principal axis of

crystal, respectively. That is $\varepsilon_i = \begin{bmatrix} cos\theta \\ sin\theta \\ 0 \end{bmatrix}$ and $\varepsilon_o = \begin{bmatrix} cos\varphi \\ sin\varphi \\ 0 \end{bmatrix}$. This generalization is important when working with the anisotropic crystal, such as the T'-TMDC. We will discuss more detail in Chapter 4 and 5.

3.4 Raman Signatures of the Atomic Layered H-TMDCs

The polarization dependence as well as the energy of the Raman modes provide a handy tool for characterization of the family of atomic layered H-TMDC. The discussion of the polarization in previous section only depends on the phonon symmetry thus quite robust for all family of atomic layered H-TMDCs. Figure 0.4 demonstrates the Raman spectra of H-$MoTe_2$ from 1L to 5L. All six peaks show layer dependent energy shift: OC and shear modes show the blue shift while IMC and breathing modes show the red shift with the increasing number of layer. In shear/breathing/OC modes, we observed those modes split when the thickness increases to five layers. The peak splitting can be understood by the group theory analysis as listed in Table 0.1: for OC modes, there are $(N+1)/2$ normal modes for $N = 3$ and 5 layers and $N/2$ normal modes for $N = 4$ layers; for shear and breathing modes, there are $(N-1)/2$ normal modes for $N = 3$ and 5 layers and $(N-2)/2$ normal modes for $N = 4$ layers. This splitting is known as Davydov splitting due to interlayer interactions [45]. However, theoretically such splitting should also occur in other modes such as OMC, IMC and IC modes. We speculate that this is because the splitting is not large enough compared with the line-width of the relevant phonon bands.

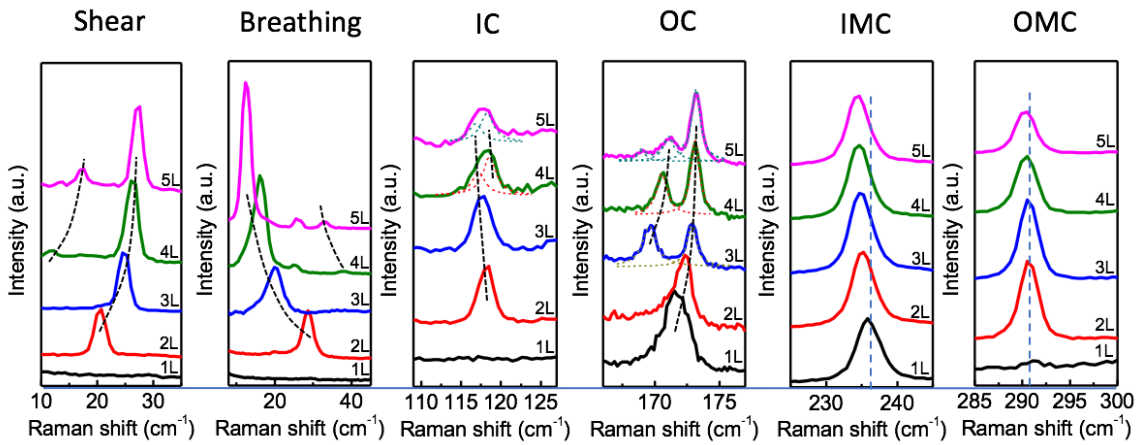

Figure 0.4: Layer dependent Raman spectra of few layer H-$MoTe_2$. The distinct peak energies provide signatures of number of layer.

The layer dependent energy shift is also observed with other members in H-TMDC. providing the signatures of number of layer. Figure 0.5 displays the helicity-resolved layer dependence of OC and IMC modes of (Mo, W)(S, $Se)_2$. As expected all the OC modes have the same helicity as the incident while the IMC modes occur only in spectra of opposite helicity. The OC modes of MoS_2 and WS_2 have similar energies 410±10 cm^{-1} [43,45–51], reflecting the fact that they both involve only sulfur atoms and that there is only a slight difference between the bond strength (spring constant) in the two materials. Similarly OC modes in $MoSe_2$ and WSe_2 have energies of 245±5 cm^{-1} which are lower due to the larger mass of selenium atoms [43,50,52–55]. For the IMC modes, the inverse of the reduced mass is given by the sum of the inverse mass of one metal atom and that of two chalcogen atoms. The light mass of sulfur atoms (2×32) thus make IMC in MoS_2 and WS_2 have higher energy (370±15 cm^{-1}) than in $MoSe_2$ (Mo: 96; 288 cm^{-1}) and WSe_2 (W: 184; Se: 2×79; 250cm^{-1}). In particular, in monolayer WSe_2, the IMC and the OC modes become accidentally degenerate. The phonon energies of H-

TMDC is summarized in Appendix B, serving as a reference to determine the number of layer.

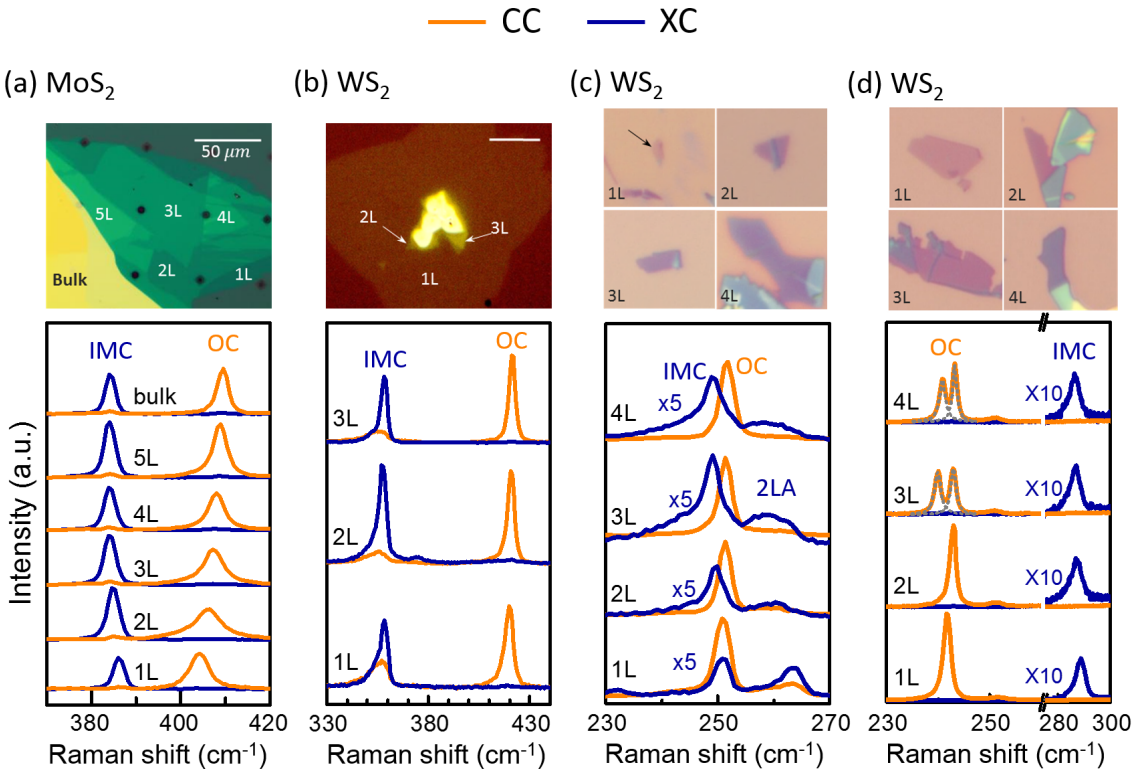

Figure 0.5: The optical images and the layer dependent Raman spectra of OC and IMC of atomically thin (Mo, W)(S, Se)$_2$.

In addition to the OC and IMC, we also perform the polarization-resolved low wavenumber Raman spectroscopy to learn the layer dependence of the shear and breathing modes. As can be seen in Figure 0.6, the spectra are strongly layer thickness dependent, with the shear (breathing) mode stiffening (softening) with increasing number of layers, and absent in monolayer TMDC as expected. This sensitive dependence, similar to that observed in multi-layer graphene [56–58], has been interpreted by a linear chain model and provides a sensitive fingerprint for TMDC atomic layer number

identification. The advantage of helicity-resolved measurement can be seen in 3L TMDCs where the B and S modes have very similar energies. The capability to separately resolve S and B modes using helicity-dependent Raman provides higher accuracy in distinguishing the subtle mode energy differences, as compared with unpolarized or linearly polarized measurements [43,47] in which the B partially overlaps with the S mode and can only be analyzed *via* multi-peak fitting.

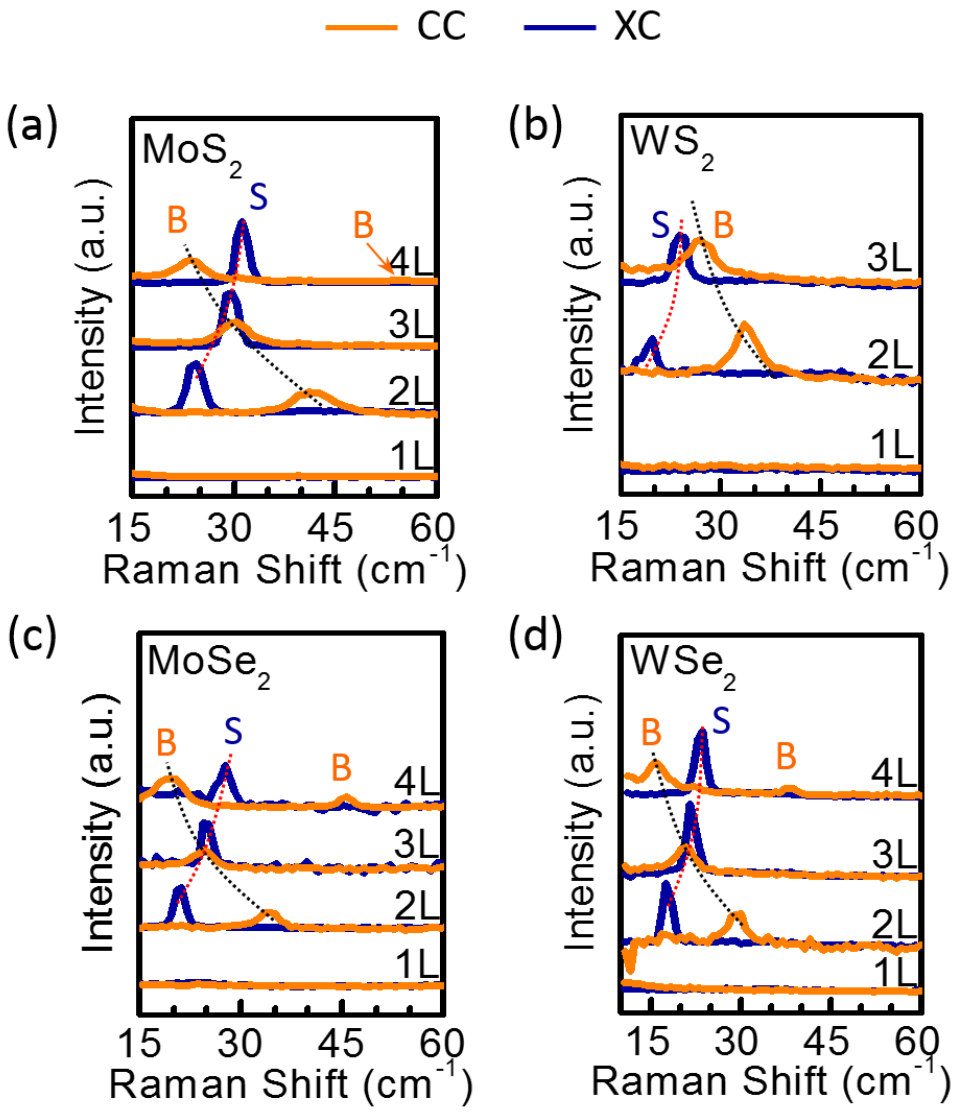

Figure 0.6: The layer dependent shear and breathing modes of atomically thin (Mo, W)(S, Se)$_2$.

3.5 Discussion

The helicity selection rule of Raman scattering is found to be robust and generic from bulk to monolayer for all the H-TMDCs. Moreover, comparing with unpolarized or linearly polarized Raman scattering, helicity-resolved Raman spectroscopy is more advantageous in distinguishing and assigning phonon modes: OC, OMC and breathing modes only show up in the same helicity as the excitation photon while IMC, IC and shear modes are opposite. In 1L H-TMDCs, due the breaking of inversion symmetry in crystal structure, the valley DoF is coupled to the photon helicity. Specifically, optical excitation of excitons in the two valleys requires angular momentum transfer of $\pm\hbar$ only when at the K points and when the conduction (valence) band is purely composed of d_{z^2} ($\frac{1}{\sqrt{2}}[d_{x^2-y^2} \pm id_{xy}]$) orbitals. This is however, not exactly true. Tight binding and density functional theory calculations show that the electron wavefunctions do have finite albeit small contributions from the *s* and *p* orbitals of the chalcogen atoms [21,59]. Another contributing factor is the wavevector dependent Berry curvature that leads to changes of lattice orbital angular momentum away from the K points. In addition, the Raman spectra we shown in previous sections are taken with off-resonant exciton of photon energy 2.33 or 2.54 eV, far from the 1*s* exciton energy. The higher excitation photon energy may also excite the high-energy states contributed from *p* and *s* orbitals, which don't follow the valley-helicity selection rule. In light of these considerations, observing both σ^+ and σ^- from the same valley is not completely surprising.

Another interesting question then arises: is the IMC mode switching the valley index of photo-excited carrier, i.e., is there inter-valley scattering during this Raman process? To understand this, we first note that the IMC is a Brillouin zone center phonon,

while inter-valley scattering requires large momentum transfer (~10^8 cm^{-1}) that is three orders of magnitude larger than the photon momentum (~10^5 cm^{-1}). Thus, conservation of momentum dictates that the IMC Raman process can only occur within the same valley, despite that the photon helicity is switched. Our data consequently point to the conclusion that in semiconducting TMDCs, even for the monolayer, photons emitted from the *same* valley can have either σ^+ or σ^- polarization, and the valley-photon helicity selection rule can only be approximately true.

3.6 Summary

In summary, we study helicity-resolved Raman scattering of the TMDC atomic layers. The switching of photon angular momentum by zone-center optical phonons is interpreted as a result of phonon symmetry, instead of intervalley scattering and spin flip, providing new insights into the relation between photon helicity and valley pumping. Comparing with unpolarized or linearly polarized Raman scattering, helicity-resolved Raman scattering provides more accurate measurements for assignment the phonon modes especially in the presence of accidental degenerate. The low wavenumber shear and breathing modes have been demonstrated as a sensitive tool to probe number of layer in the atomically thin TMDCs. We further anticipate that, from the generic symmetry considerations presented here, the helicity-resolved Raman spectroscopy is applicable as a powerful tool for characterizing the interlayer polymorphs by probing breathing modes, shear modes, layer stacking etc. in all 2D layered materials.

CHAPTER 4

RAMAN SIGNATURES OF THE INVERSION SYMMETRY BREAKING IN T'-$MoTe_2$

4.1 The Weyl Semimetal Candidates: T'-TMDCs

Distorted octahedral (T') transition metal dichalcogenides (TMDCs) are predicted to possess topologically nontrivial electronic bands that host quantum spin Hall states [60] and type II Weyl fermions [14] in the vicinity of the Fermi energy, which has sparked much recent interest in understanding this class of topological layered compounds. As a nonmagnetic material system, an important condition for the existence of Weyl nodes is the breaking of inversion symmetry [14]. In particular, T'-$MoTe_2$, as a promising candidate for studying novel type II Weyl physics, has both centrosymmetric and non-centrosymmetric polymorphs.

In addition to the H phase which is the focus in Chapter 3, $MoTe_2$ has another two octahedral metastable phases as illustrated in Figure 0.1: the centrosymmetric monoclinic (T'_{mo}) phase at room temperature (RT) and the non-centrosymmetric orthorhombic (T'_{or}) phase at low temperature (LT) below 150K. The latter was recently predicted to be a type II Weyl semimetal. The cousin of T'-$MoTe_2$, WTe_2 also a Weyl semimetal candidate, having a stable non-centrosymmetric phase T'_{or} phase in all temperature range. However, the T'_{mo}-$MoTe_2$ was predicted having much larger separation between Weyl points of opposite chirality [61], making the Weyl fermions presumably easier to access experimentally with tools such as angle resolved photon emission spectroscopy. This has led to intense experimental studies of T'-$MoTe_2$, revealing its rich fundamental properties

related to superconductivity, electronic band structure, Fermi surface, lattice vibrations, charge transport, etc. [62–71].

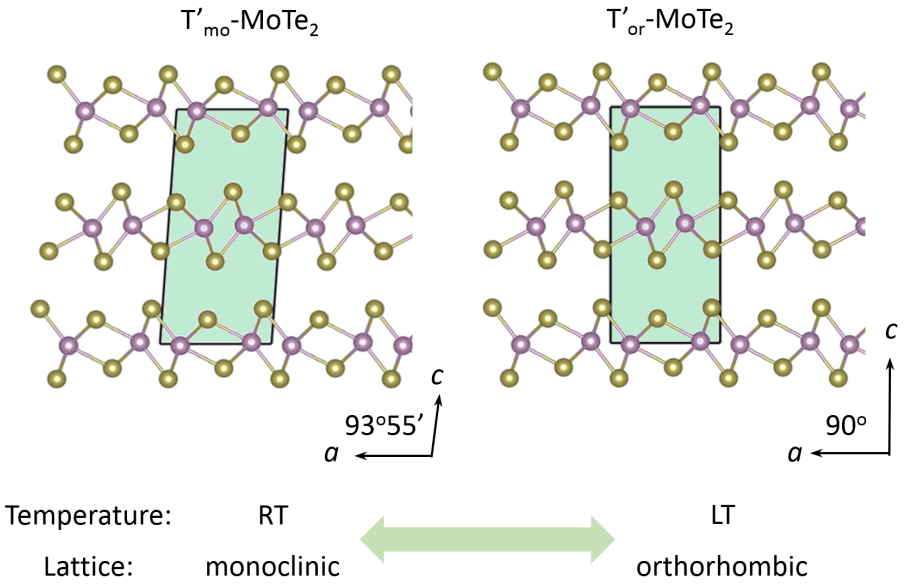

Figure 0.1: An example of bulk T'-$MoTe_2$ interlayer polytypes. The schematic phase transition from RT T'$_{mo}$ to LT T'$_{or}$ phases induced by lowering temperature across the critical temperature.

In this chapter, we first synthesize T'-$MoTe_2$ by CVT method followed by thermal quenching to generate the needle-like crystal in a metastable phase. We then investigate the vibrational properties of the selected single crystal with Raman spectroscopy, density functional theory and symmetry analysis. Compared to the results from RT T'$_{mo}$ phase, four new Raman bands emerge in the LT T'$_{or}$ phase, providing the signature of phase transition. Furthermore, the crystal-angle-dependent, light-polarization-resolved measurements indicate that all the observed Raman peaks belong to two categories: those vibrating along the zigzag Mo atomic chain (*z*-modes) and those vibrating in the mirror plane (*m*-modes) perpendicular to the zigzag chain. Interestingly

the low energy shear *z*-mode and shear *m*-mode, absent from the T'_{mo} spectra, become activated when sample cooling induces a phase transition to the T'_{or} crystal structure. We interpret this observation as a consequence of inversion-symmetry breaking, which is crucial for the existence of Weyl fermions in the layered crystal.

4.2 Bulk T'-$MoTe_2$ Synthesis and the Raman Characterization

The T'-$MoTe_2$ crystal used in this work is grown *via* chemical vapor transport method using bromine as the transport agent. High purity Mo, Te, and $TeBr_4$ powders are placed in a fused silica tube, 18 mm in diameter and 300 mm in length. The purity of the source materials are Mo 99.9 %, Te 99.997 %, and $TeBr_4$ 99.999 % (Sigma Aldrich). Total Mo and Te are kept in a stoichiometric 2:1 ratio with sufficient $TeBr_4$ to achieve a Br density of 3 mg/cm^3. The tube is pump-purged with ultra-high purity argon gas and sealed at high vacuum prior to growth.

We apply a three-zone tube furnace with 1 inch diameter to perform the growth. The three-zone furnace enable us to maintain the temperature gradient between the source end and growth end. The high temperature reaction zone and a low temperature growth zone were kept at 1000 °C and 900 °C respectively for 100 hours. At the end of the growth, the whole fused silica tube as well as the crystal attached on the wall is thermally quenched in a cold water bath to keep the crystal from transitioning into the hexagonal phase.

The as-grown layered crystals have needle-like shape (Figure 0.2a and b), with typical lengths of about 10 mm (along the *a*-axis) and widths of about 1 mm (along the *b*-axis). This elongated shape is a result of in-plane anisotropy of the crystal: as illustrated

in Figure 0.2c for a monolayer, the strong bonding strength between the Mo-Mo atoms distorts the crystal lattice, forming zigzag Mo atomic chains (purple zigzags) to lower the free energy of the crystal, resulting in atomic scale periodic buckling. In Figure 0.2c we also illustrate a mirror symmetry plane (*m*, thick red horizontal line) that is perpendicular the zigzag chains. The zigzag (*z*) chain and the mirror (*m*) provide useful classification in T'-TMDC and facilitate the discussion of phonons (vibrations along the zigzag chain: *z*-modes; in the mirror plane: *m*-modes) that we will use throughout this chapter and Chapter 5.

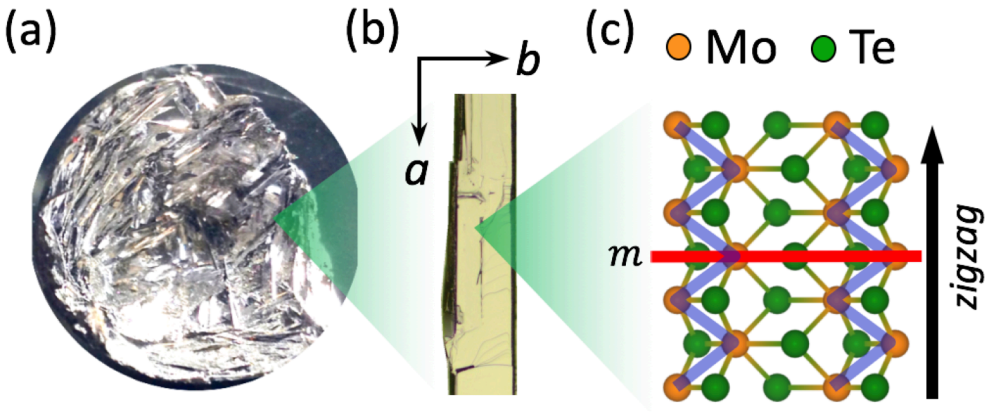

Figure 0.2: (a) Picture of a grown T'-$MoTe_2$ sample composed of many needle-like single crystals. (b) A zoomed-in optical image of a T'-$MoTe_2$ single crystal. The needle direction is along the *a*-axis. (c) Top view of atomic arrangement of a monolayer T'-$MoTe_2$. The *a*-axis points along the Mo-Mo zigzag chain (purple zigzags); and the *b*-axis lies in a mirror plane (thick red horizontal line) perpendicular to the zigzag chains.

Figure 0.3 compares the typical Raman spectra of bulk T'$_{mo}$-MoTe$_2$ at 300 K comparing with its counterpart, bulk H-MoTe$_2$. The three sharp peaks in bulk H-MoTe$_2$ have been assigned as shear, OC and IMC modes from left to right following the convention we used in Chapter 3 for H-TMDCs. However, T'$_{mo}$-MoTe$_2$ displays distinct Raman bands, directly pointing out that the Raman scattering is highly sensitive to the intralayer polytypes. In contrast to H-MoTe$_2$ which has 24 symmetry operations (D_{6h}), the distortion in Mo atoms lowers the crystal symmetry down to 4 symmetry operations (C_{2v}) left. As the results, the size of unit cell become twice bigger, doubling the phonon modes.

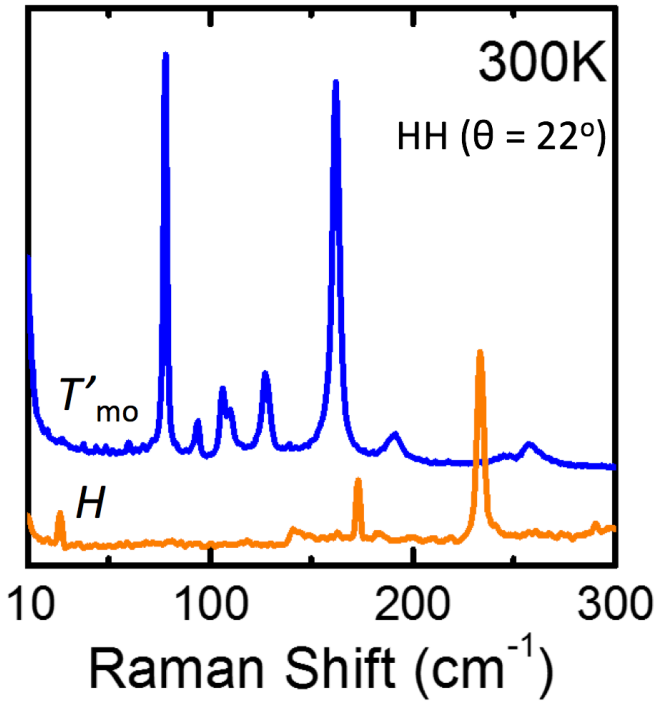

Figure 0.3: Typical Raman spectra of T'$_{mo}$ and H bulk MoTe$_2$.

Figure 0.4 displays the Raman spectra of our bulk T'-$MoTe_2$ sample at 78K and 296K with various polarization configurations. The crystal orientation dependence of mode intensity (defined by θ: the angle between crystal a-axis and light polarization) can be explained by polarization selection rules, similar to the works have been done in the section 3.3. Figure 0.4b-e show detailed RT and LT T'-$MoTe_2$ Raman bands with $\theta = 45°$ and $0°$ in HV scattering geometry. The $\theta = 45°$ spectra selectively reveal the m-modes (8 for the LT orthorhombic T'$_{or}$ phase and 6 for the RT monoclinic T'$_{mo}$ phase), and the $\theta = 0°$ spectra select the z-modes (5 for LT T'$_{or}$ and 3 for RT T'$_{mo}$ phase). Interestingly, in the LT T'$_{or}$ phase, four additional Raman bands become activated as compared with the RT T'$_{mo}$ phase; two of these new bands appear at low energies whereas the other two appear at high energies, as highlighted by the yellow bands in panels (b) and (c). The two new high energy modes are further displayed in the zoomed-in panels (d) and (e) with the spectra being measured by triple additive scattering, enabling us to resolve the two overlapped peaks. These four peaks provide the signature of different phases in T'-$MoTe_2$. In particular, the two low wavenumber modes which are attributed the two shear modes, m_{or} at 12.6 cm^{-1} and z_{or} at 29.1 cm^{-1}, directly link to the inversion symmetry, i.e. these two shear modes become Raman inactive in T'$_{or}$ due to the inversion symmetry is broken [29].

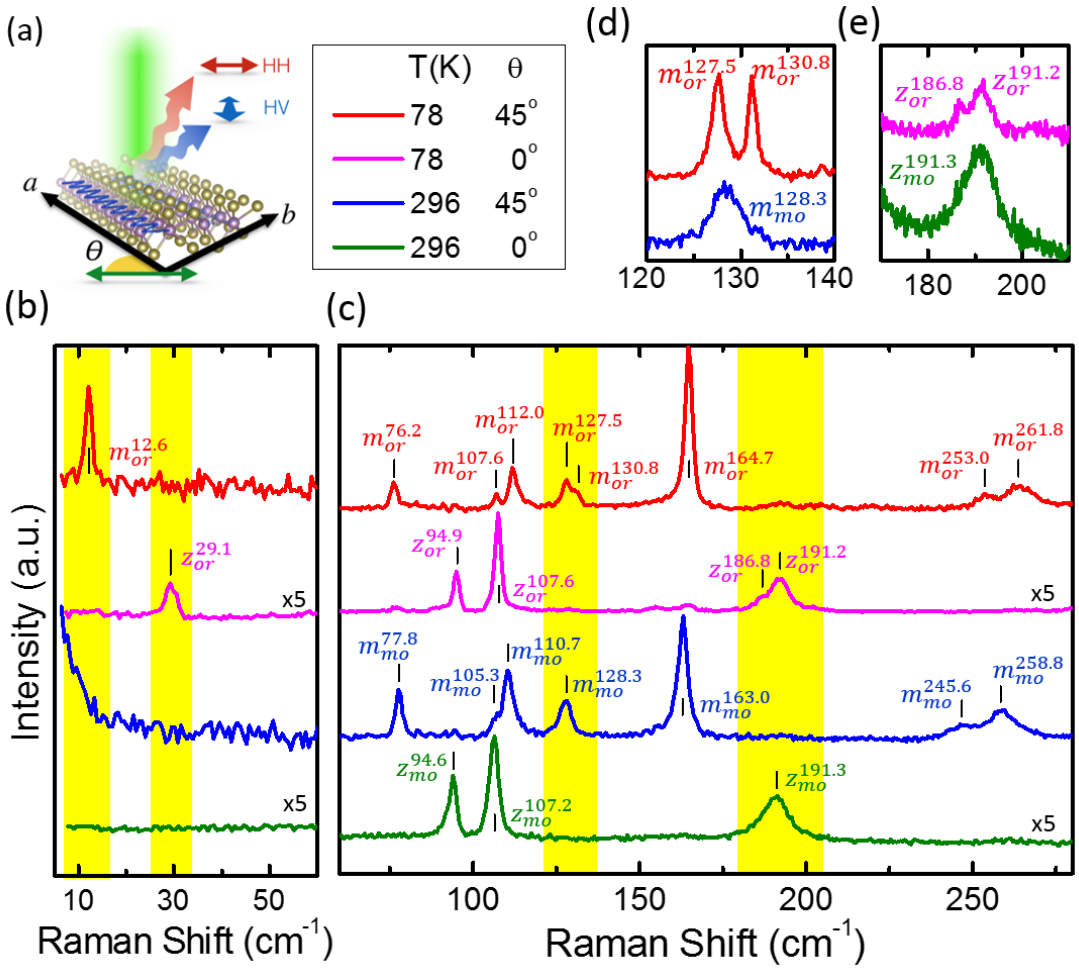

Figure 0.4: (a) Schematic of linear polarization-resolved Raman spectroscopy. The θ is defined as the angle between crystal *a*-axis and incident light polarization. (b&c) The Raman spectra of T'-$MoTe_2$ at 78 K and 296 K in HV with $\theta = 45°$ and 0°. The yellow bands highlight the four emerging new modes at 78 K. Panels (d) and (e) show the zoomed-in spectra of the two new high energy modes.

For θ between 0° and 45°, both the m- and the z-modes have finite intensity. Table 0.1 displays the detailed Raman intensity dependence on angle θ for 13 T'_{or} modes and 9 T'_{mo} modes in HH and HV configurations, enabling us to categorize the phonons into two generic groups, z-modes and m-modes: z-modes indicate the vibration along the zigzag direction while m-modes is the vibration mode in the mirror plane (more discussion will be shown by DFT calculation in section 4.3).The angular dependence for m-modes in HH scattering is highly sensitive to specific lattice vibration, while in HV all the mode intensities display four-fold symmetry, with the m-mode peaks at $\theta = 45°$ and z-mode peaks at $\theta = 0°$, as evidenced by spectra in Figure 0.4b to 4.4e.

Table 0.1: The angular dependence (with respect to the *a*-axis) of Raman intensity of m_{or}, z_{or}, m_{mo} and z_{mo} modes. The polarization configurations (HH or HV) and the mode energies are noted in each panel. The solid curves are fits using Eq. 4.1–4.4 in Chapter 4.3.

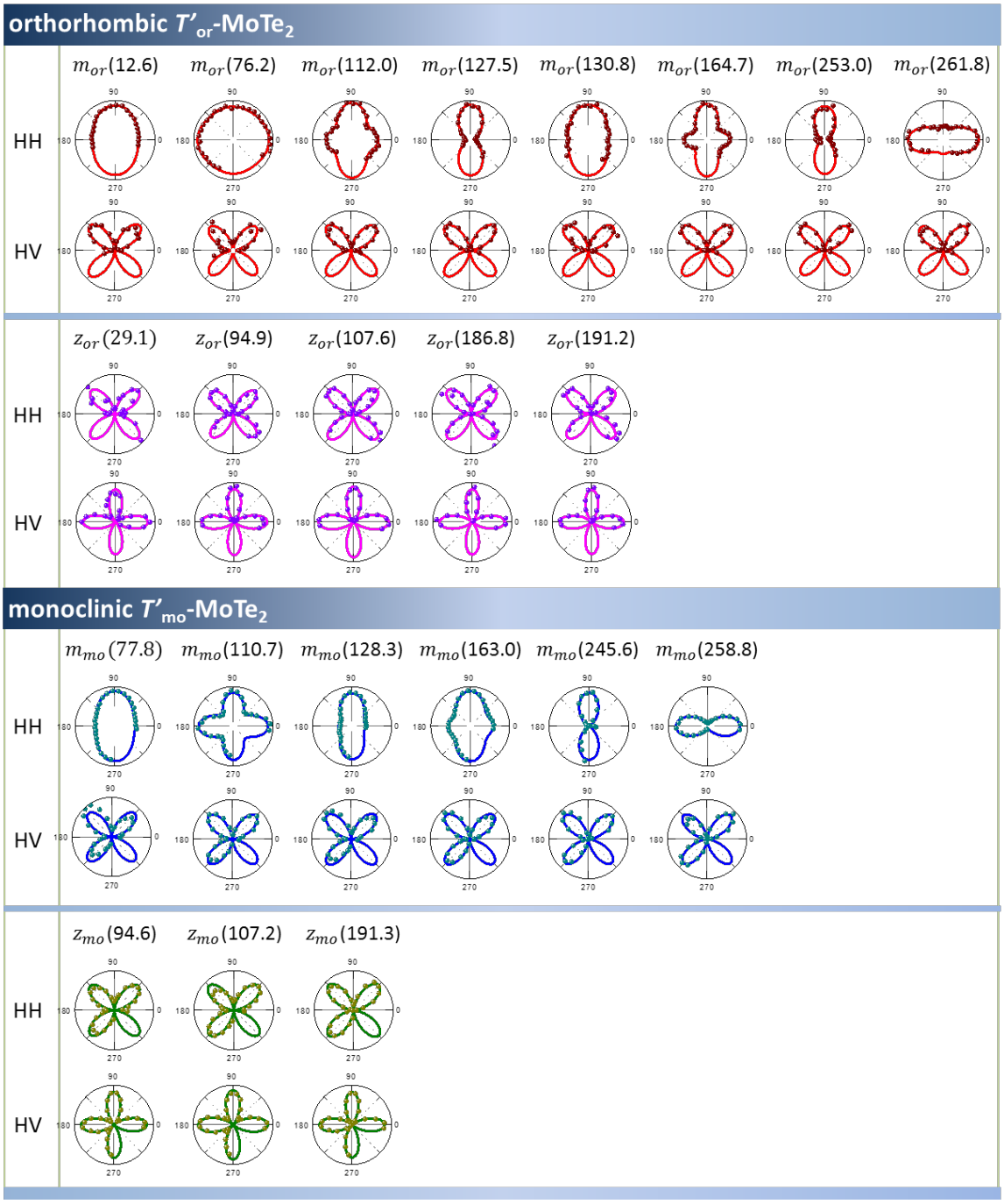

4.3 Symmetry Analysis and DFT Calculation on T'-$MoTe_2$ Phonons

Below we explain the experimental observations with symmetry analysis and density functional theory (DFT) calculations. We have chosen in Figure 0.2 the in-plane *a*- and *b*- axes as along the zigzag Mo chain and parallel to the mirror plane respectively. The out-of-plane *c*-axis is also parallel to the mirror plane *m*, and is thus perpendicular to the *a*-axis; meanwhile its angle made with the *b*-axis depends on the crystal phase, which is 93.44° in T'_{mo} (Figure 0.5a) and 90° in T'_{or} (Figure 0.5b). The difference in the *c*-axis direction has important consequences for crystal symmetry. To understand this, we first examine the crystal symmetry as illustrated in Figure 0.5.

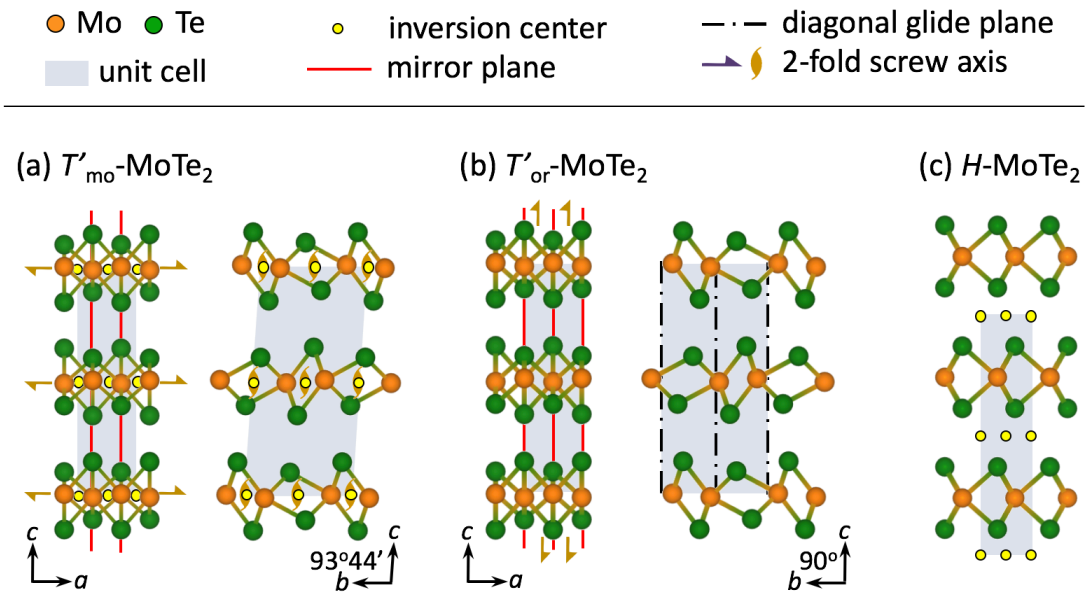

Figure 0.5: Atomic arrangement of (a)T'_{mo} (b) T'_{or} and (c) H-phase $MoTe_2$.

The T'_{mo} phase has three symmetry operations in addition to translations along the primitive lattice vectors, including: inversion (*i*), a mirror plane (*m*), and a screw axis along the zigzag Mo chain (2_1^z), where the superscript *z* stands for 'zigzag' (the symbols

are consistent with the International Table for Crystallography) [72]. In contrast, the T'$_{or}$ phase only shares the mirror plane symmetry (m) with the T'$_{mo}$ phase. The two other symmetry operations for T'$_{or}$ $MoTe_2$ are a screw axis along c-axis (2_1^c), and a glide plane perpendicular to the b-axis (n). The symmetry group of T'$_{mo}$ and T'$_{or}$ $MoTe_2$ are thus C_{2h} (No.11 $P2_1/m$) and C_{2v} (No.31 $Pmn2_1$) respectively [72–74]. For facilitate the discussion of the shear modes later, we also illustrate in Figure 0.5c the H-$MoTe_2$ unit cell and its inversion centers for comparison.

Since both T'$_{mo}$ and T'$_{or}$ $MoTe_2$ contain two layers of $MoTe_2$ and 12 atoms in the unit cell (shaded area in Figure 0.5a & Figure 0.5b), each crystal hosts 36 phonon branches. We use plane-wave density functional theory (DFT) as implemented in the Vienna *Ab Initio* Simulation Package (VASP) [75] to calculate the 36 phonon branch dispersions. As standard DFT functionals fail to describe interlayer van der Waals bonding correctly, we used the non-local optB86b van der Waals functional [76,77], which reproduces the equilibrium geometry of $MoTe_2$ accurately [29,78]. Table 0.2 and Table 0.3 show the results of DFT calculation, including first Brillouin zone, phonon dispersion, character table for symmetry group, and zone center normal modes with their calculated energies as well as the vibrational symmetry representations for both bulk T'$_{mo}$ and T'$_{or}$ $MoTe_2$, respectively. We note that all the DFT calculated zone-center optical phonons have different energies; this is because the irreducible representations of both C_{2h} and C_{2v} are one dimensional, in contrast to the hexagonal phase we displayed Chapter 3, in which all in-plane phonons are doubly degenerate [28,79]. The symmetry analysis from Figure 0.5 also shows that the mirror plane reflection symmetry m is shared both in the T'$_{mo}$ and T'$_{or}$ bulk $MoTe_2$ crystals. This provides a generic classification of lattice

vibrations in T'-TMDC: one-third of the vibrations along the zigzag chain are odd under *m* operation(*z*-modes); and two-third of the vibrations parallel to the mirror plane are even (*m*-modes). To make this clear, we group the 12 *z*-modes and 24 *m*-modes in Tables 4.2 and 4.3. We note that this rule can also apply to the atomically thin T'-TMDC layers, as we present in Chapter 5.

Table 0.2: DFT calculation results of T'$_{mo}$-$MoTe_2$, including first Brillouin zone, phonon dispersion, character table for C_{2h} symmetry group, and the schematics of zone center normal modes with their calculated energies as well as the vibration symmetry representations.

monoclinic phase

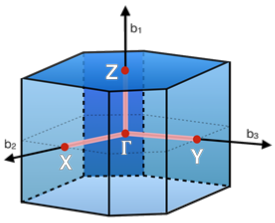

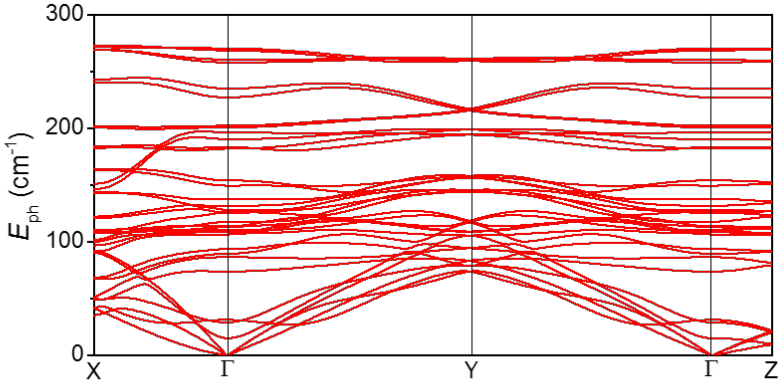

character table

C_{2h}	E	2_1^z	i	m
A_g	1	1	1	1
B_g	1	-1	1	-1
A_u	1	1	-1	-1
B_u	1	-1	-1	1

E: identity
2_1^z: screw axis along zigzag axis
i: inversion
m: mirror plane

z-mode

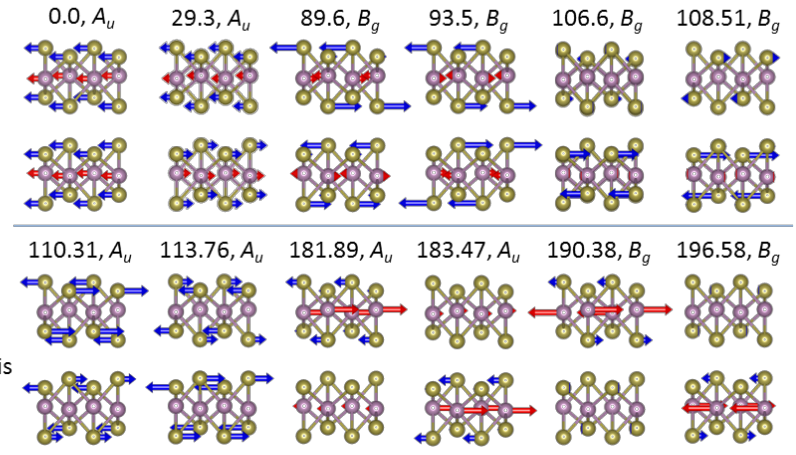

m-mode

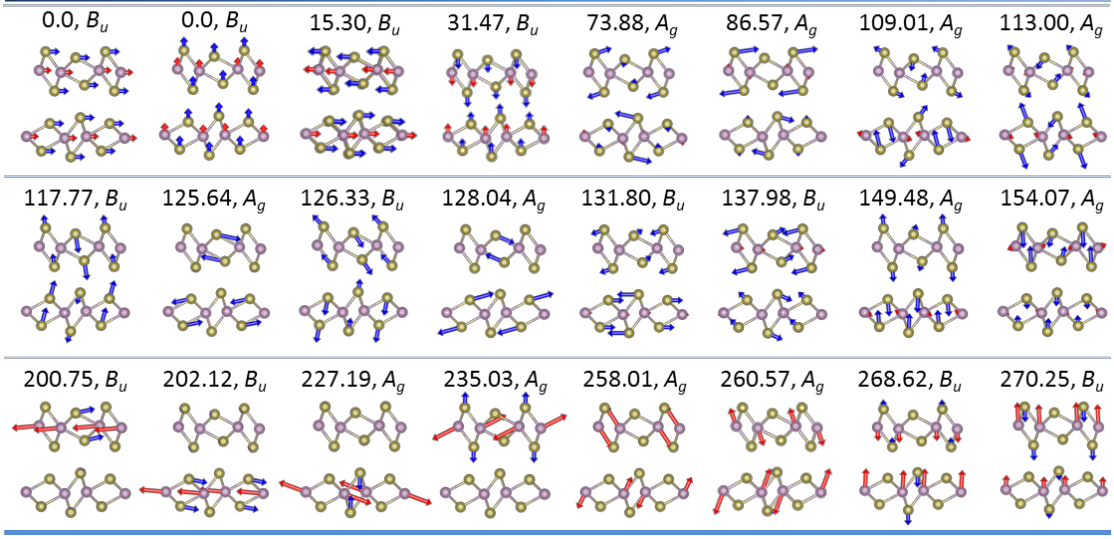

Table 0.3: DFT calculation results of T'$_{or}$-MoTe$_2$, including first Brillouin zone, phonon dispersion, character table for C_{2v} symmetry group, and the schematics of zone center normal modes with their calculated energies as well as the vibration symmetry representations. The four new modes, $z_{or}^{29.1}$, $z_{or}^{186.8}$, $m_{or}^{12.6}$ and $m_{or}^{130.8}$ are highlighted in yellow.

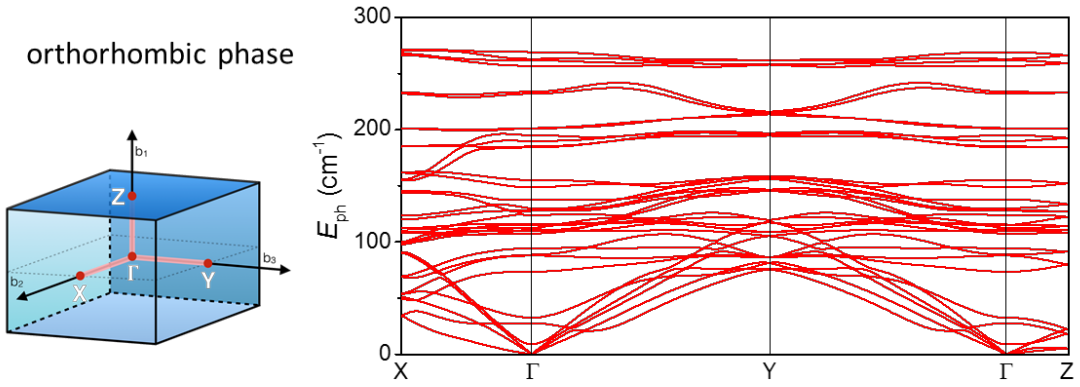

character table

C_{2v}	E	2_1^c	n	m
A_1	1	1	1	1
A_2	1	1	-1	-1
B_1	1	-1	1	-1
B_2	1	-1	-1	1

E: identity
2_1^c: screw axis along c-axis
n: diagonal glide plane
m: mirror plane

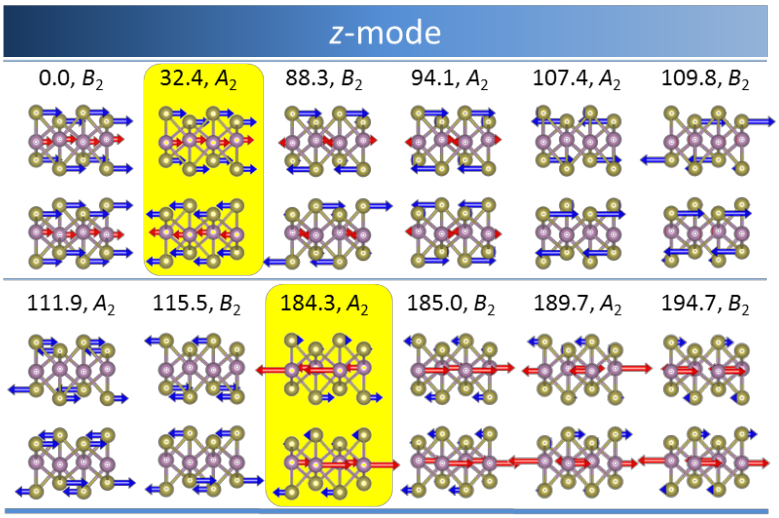

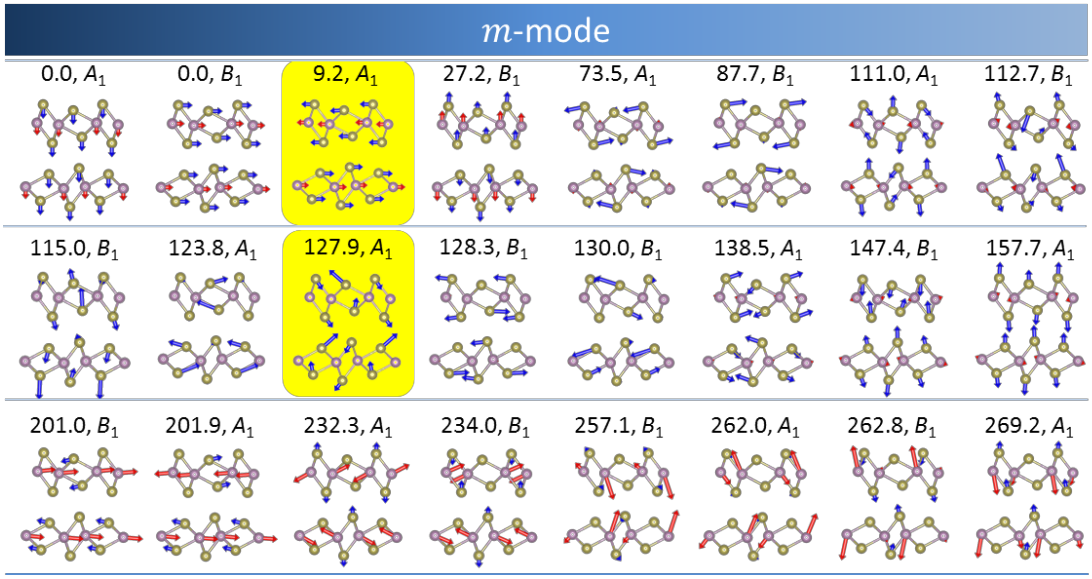

With the understanding of the crystal symmetry, we are able to figure out the polarization selection rules by applying the corresponding Raman tensors (See Appendix A). In the back-scattering geometry, the Raman active m-modes have A_g symmetry in T'$_{mo}$ and A_1 symmetry in T'$_{or}$; similarly the Raman active z-modes have B_g symmetry in T'$_{mo}$ and A_2 symmetry in the T'$_{or}$ phase. The in-plane Raman tensor is thus given by [44](In back scattering geometry, we can consider only x and y axis for simplicity): for the m-modes, $\mathfrak{R}_m = \begin{bmatrix} d & 0 \\ 0 & e \end{bmatrix}$ (A_g of C_{2h} for T'$_{mo}$ and A_1 of C_{2v} for T'$_{or}$); for the z-modes, $\mathfrak{R}_z = \begin{bmatrix} 0 & g \\ g & 0 \end{bmatrix}$ (B_g of C_{2h} for T'$_{mo}$ and A_2 of C_{2v} for T'$_{or}$). The intensity of a Raman-active lattice vibration is given by $I = A|\langle \epsilon_i | R^T \cdot \mathfrak{R} \cdot R | \epsilon_o \rangle|^2$, where A is a constant, ϵ_i and ϵ_o are polarizations of the incident and outgoing light respectively, $\mathfrak{R}$ is the effective Raman tensor linked to $\mathfrak{R}_m$ or $\mathfrak{R}_z$, R and R^T are the rotation matrix and its transpose that account for rotation of crystal or equivalently, light polarization. The rotation matrix is given by $R = \begin{bmatrix} \cos(\theta) & -\sin(\theta) \\ \sin(\theta) & \cos(\theta) \end{bmatrix}$.

In HV scattering, $\epsilon_i = \begin{bmatrix} 1 \\ 0 \end{bmatrix}$, $\epsilon_o = \begin{bmatrix} 0 \\ 1 \end{bmatrix}$. The Raman intensities are given by:

$$I_{HV}^{m}(\theta) = \left|\frac{d-e}{2}\right|^2 \sin^2(2\theta), \quad \text{(Eq. 4.1)}$$

$$I_{HV}^{z}(\theta) = |g|^2 \cos^2(2\theta). \quad \text{(Eq. 4.2)}$$

In HH scattering, $\epsilon_i = \begin{bmatrix} 1 \\ 0 \end{bmatrix}$, $\epsilon_o = \begin{bmatrix} 1 \\ 0 \end{bmatrix}$. The Raman intensities are given by:

$$I_{HH}^{m}(\theta) = |d \cos^2\theta + e \sin^2\theta|^2, \quad \text{(Eq. 4.3)}$$

$$I_{HH}^{z}(\theta) = |g|^2 \sin^2(2\theta). \quad \text{(Eq. 4.4)}$$

In HV scattering, the intensities of *m* and *z* modes are expected to depend on θ as $\sin^2(2\theta)$ and $\cos^2(2\theta)$, providing convenient classification of the two types of Raman bands. We have taken advantage of this fact in Figure 0.4b-e to selectively display *m*-modes with HV $\theta = 45°$, and *z*-modes with HV $\theta = 0°$. We note that due to in plane anisotropy in dielectric constant and absorption, *d*, *e*, and *g* in the effective Raman tensors are allowed to be complex [80–82]. Thus in HH scattering, the *z*-mode scales as $\sin^2(2\theta)$ while the angular dependence of the *m*-mode is sensitive to the phase difference between *d* and *e*, and can exhibit different shapes for different phonons with the same symmetry. These are in good agreement with the angular patterns seen in Table 4.1 and support our experimental classification and assignment of *m* and *z* mode vibrations. With this thorough understanding of symmetry representation and lattice classification, we can unambiguously assign m_{or} at 12.6 cm^{-1} as the shear mode vibrating along the *b*-axis, and z_{or} at 29.1 cm^{-1} as the shear mode vibrating along the *a*-axis in T'$_{or}$-$MoTe_2$.

4.4 Raman Signature of Inversion Symmetry Breaking in T'-$MoTe_2$

In this section, we demonstrate that Raman spectroscopy is not only sensitive to the intralayer polytypes but also can be a tool to probe the inversion symmetry breaking. Conventionally, few methods have been applied to determine the inversion symmetry of bulk crystal. First, the microscopy technique with atomic resolution, such as Transmission Electron Microscopy (TEM), can directly see the lattice structure. However, the specimen preparation for such measurement is extremely complicated and is limited to few atoms in thickness and few nanometer in size. Second harmonic generation(SHG) measurement is an optical measurement which is sensitive to the inversion symmetry of crystal [83]. However, the cross-section of SHG signal is typical small and hence it requires specialized sub-ps pulsed laser with high instantaneous power. Raman spectroscopy is a non-invasive optical measurement and has been widely used in 2D materials community. With the polarization-resolved Raman scattering setup, we will able to determine the inversion symmetry by seeing the low wavenumber shear and breathing modes.

With an overall picture of the lattice vibrations as described above, we build an intuitive link between inversion symmetry breaking and Raman scattering of the two shear modes in the T'-$MoTe_2$ crystals. We first note that T'$_{mo}$-$MoTe_2$, like the T'$_{or}$ phase, has two layers of $MoTe_2$ in its unit cell. The monoclinic crystal thus also supports two shear vibrations: one *m*-mode along the *b*-axis and one *z*-mode along the *a*-axis. The reason why these modes evade in Raman scattering measurements at room temperature is closely linked to the inversion symmetry and the position of inversion centers. The presence of inversion symmetry in T'$_{mo}$-$MoTe_2$ dictates that all the zone-center lattice

vibrations have either even or odd parity, and the odd ones are Raman inactive due to selection rules. With the inversion centers located inside the $MoTe_2$ atomic layers (Figure 0.5a), we observe that the two shear modes calculated to be at 15.3 and 29.3 cm^{-1} in Table 4.2 are odd under the inversion operation. This explains why at RT the T'-$MoTe_2$ Raman spectra do not show shear modes in Figure 0.4b. It is interesting to note that bulk H-$MoTe_2$ displays its shear mode at 27.5 cm^{-1} in Figure 0.3, in spite of being inversion symmetric. This is because for H-TMDC the inversion centers are located in-between the atomic layers (as shown in Figure 0.5c), making the shear modes centrosymmetric even under the inversion operation and thus are Raman active.

Since the shear modes in T'$_{mo}$-$MoTe_2$ have odd parity, the emergence of shear Raman intensity at low temperatures is an indication of cooling induced structural phase transition that breaks the inversion symmetry. The process of inversion symmetry breaking can be monitored by measuring the evolution of the Raman spectra as the temperature changes. Figure 0.6 shows typical evolution of *m*-mode Raman spectra with energies less than 150 cm^{-1} when the sample is cooled down from RT to 78 K and then warmed back up to RT. The Raman bands between 70 and 130 cm^{-1} appear at all temperatures, with slight changes in peak position and linewidth due to cooling or warming. The two new *m*-modes at 12.6 and 130.8 cm^{-1} which only occur in the T'$_{or}$ phase are found to be sensitive to whether the temperature is going down or up; at 236 K, the peak intensity is much larger during warming than during cooling. This suggests that there is significant hysteresis in the T'$_{mo}$ → T'$_{or}$ → T'$_{mo}$ phase transition.

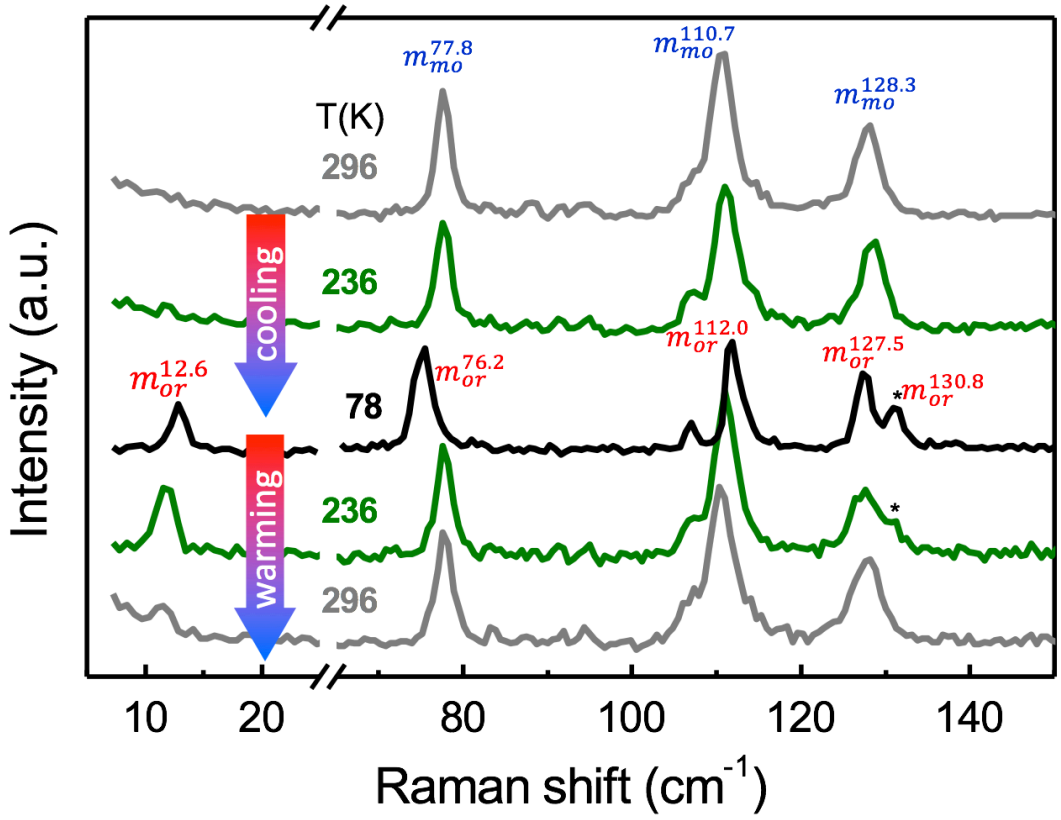

Figure 0.6: The T'-$MoTe_2$ *m*-modes shown up in Raman spectra with energy less than 150 cm^{-1} under different thermal cycles. The Raman spectra collected here are dispersed by a single grating. Two modes $m_{or}^{12.6}$ and $m_{or}^{130.8}$ emerge when the sample cools down from 296 K to 78 K and persist during warming up to 296 K.

In Figure 0.7 we have plotted the temperature dependence of the peak intensity for the shear mode $m_{\mathrm{or}}^{12.6}$ during cooling and warming. The originally missing $m_{\mathrm{or}}^{12.6}$ persists up to RT when we warm up from LT and we had to heat the crystal up to 339K to make it completely disappear. At low temperatures, the peak intensities of $m_{\mathrm{or}}^{12.6}$ tend to stabilize below 200 K and become independent of cooling or warming. This indicates that the crystal is stabilized in pure T'$_{\mathrm{or}}$ phase, without any admixture from the T'$_{\mathrm{mo}}$ at low temperatures, making it suitable for probing type II Weyl physics. The shear mode has low energy and requires relatively specialized Raman system to perform the

measurement; however, the alternative mode at 130.8 cm^{-1} (highlighted by an asterisk in Figure 0.7), which should be easily accessible to most Raman setups, displays behavior similar to the shear $m_{or}^{12.6}$: it appears only in the T'$_{or}$ phase and has hysteresis in concert with the $m_{or}^{12.6}$. We thus conclude that the $m_{or}^{130.8}$ mode provides the most convenient signature for monitoring the inversion symmetry breaking and the phase transition to the T'$_{or}$ structure. One could, in principle, use instead $z_{or}^{29.1}$ and $z_{or}^{186.8}$ modes; however we have found that these peaks are much weaker than $m_{or}^{12.6}$ and $m_{or}^{130.8}$ in our experimental setup.

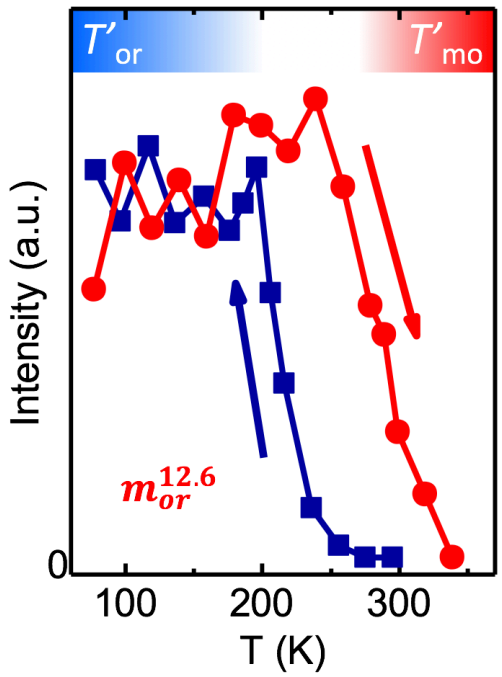

Figure 0.7: Temperature dependent intensity of $m_{or}^{12.6}$ mode during cooling (dark blue) and warming (red). The hysteresis means that T'$_{mo}$ and T'$_{or}$ phases can coexist in certain temperature range.

4.5 Summary

In conclusion, we have probed with Raman scattering the inversion symmetry and the crystal phase transition of T'-$MoTe_2$. Our investigation provides a generic approach for analyzing and detecting the lattice *m*-mode and *z*-mode vibrations. The two new shear modes that we observed and systematically analyzed were found to be directly linked to inversion symmetry breaking in the T'_{mo}–T'_{or} structural phase transition in the crystal. The two concomitant high energy modes, especially the $m_{or}^{130.8}$ mode, provide a convenient Raman fingerprint for the T'_{or} phase that has raised much recent interest for studying type II Weyl fermions. Finally, the thermally-driven stacking changes could also occur in atomically-thin T'-$MoTe_2$, raising interesting questions regarding stacking-dependent vibrational, optical and electronic properties.

CHAPTER 5

PROBING THE DEGRADATION OF 1L T'-(MO, W)TE_2 BY RAMAN SPECTROSCOPY

5.1 Research Objective and Motivation

It is of both fundamental and practical interest to develop a thorough understanding of T'-(Mo, W)Te_2 at the monolayer level. Theory calculations predict the quantum spin Hall (QSH) effect in T' monolayers, a foundation for developing topological quantum computing devices, inspiring several experimental studies on thin films [84,85] (~10 nm thick) of T'-(Mo, W)Te_2. In addition, 1L T'-TMDC can serve as a bottom-up starting point for understanding multi-layered and intercalated T'-TMDCs, which have been used in the applications for solid state battery electrodes, electrochemical capacitors, and hydrogen evolution reactions [86,87]. As it turns out 1L T'-TMDC is relatively challenging to work with due to the rapid sample degradation in air [88,89]. For this reason, recent optical and electrical studies on T'-TMDCs [84,85,89] are limited to multi-layers; and despite recent efforts [90–92], a thorough Raman characterization of 1L T'-TMDC is still lacking.

In this chapter, we focus on the realization of the complete Raman signatures of well-protected high quality 1L T'-(Mo, W)Te_2, exhibiting sharp and robust intrinsic

Raman bands. We also discovered that less protected samples show coexistence of phonon spectra of T'-$MoTe_2$ and its degradation products; the two types of Raman features exhibit drastically different symmetry properties, and can be unambiguously distinguished by light-polarization and crystal-angle resolved Raman tensor analysis.

5.2 Sample Preparation and Microscopic Characterization

The 1L T'-$MoTe_2$ studied in this work is grown by chemical vapor deposition (CVD) on 300 nm SiO_2/Si substrate [71]. To achieve the growth of metastable T' phase, the sample is rapid thermal quench from 700°C to RT [71]. Figure 0.1 shows the optical image of a typical sample. The CVD grown 1L T'-$MoTe_2$ flakes have a bamboo-leaf like shape. The step-height from substrate to the monolayer is about 0.8 nm as shown by AFM measurements in Figure 0.1b, which is consistent with the 0.7–0.8 nm per layer thickness from previous studies [93].

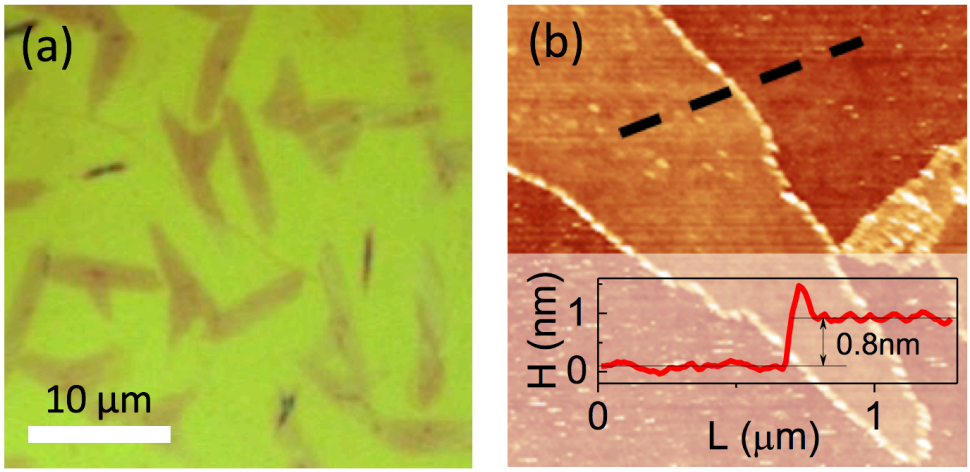

Figure 0.1: (a) The optical micrograph of a typical CVD grown 1L T'-$MoTe_2$ sample. All bamboo-leaf like flakes on the image are 1L T'-$MoTe_2$, and the small dark dots near center of the flakes are multilayer crystals. (b) AFM image of a monolayer flake. The step height is 0.8 nm.

The as grown 1L T'-$MoTe_2$ flakes were transferred onto a commercial holey-carbon TEM grid using a typical wet transfer method for further microscopy characterization. he TEM was performed with a JEOL ARM 200CF equipped with a CEOS corrector and a high-angle annular dark field detector. The operation voltage is kept below 80 kV to avoid sample damage. As shown in the Figure 0.2a and b, the crystal grows preferentially along the zigzag chains, which we denote as the *a*-axis. This can be seen from the TEM diffraction pattern (Figure 0.2b): the rectangular reciprocal lattice is in accord with the rectangular real space unit cell (light blue rectangle in Figure 0.2c), from which we determine the in-plane unit vector lengths of the crystal to be a = 3.42 Å, b = 6.34 Å. For later description of the lattice vibrations we also show in Figure 0.2c the mirror plane and zigzag chains, in line with the definition we used for bulk T'-$MoTe_2$ in Chapter 4.

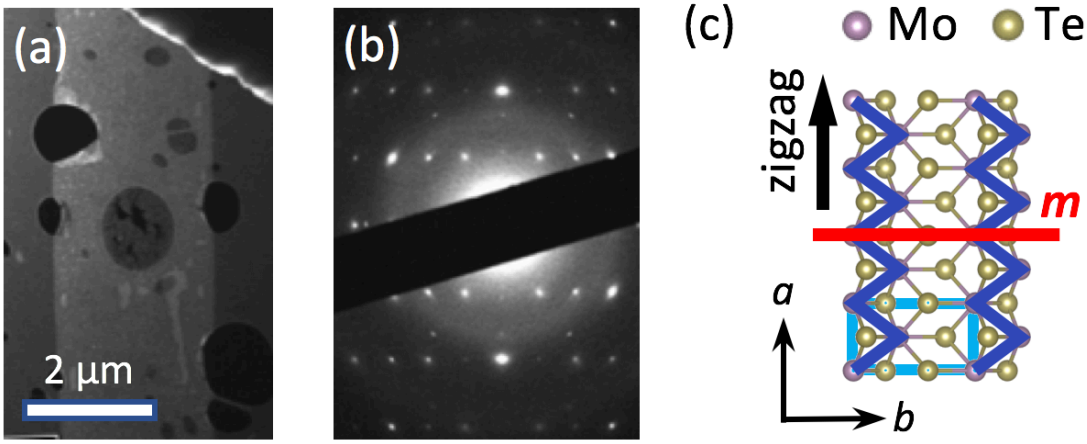

Figure 0.2: (a) Dark field TEM image of a 1L T'-$MoTe_2$ flake transferred on top of holey carbon film. (b) The selected-area electron diffraction image of a suspended 1L T'-$MoTe_2$, exhibiting rectangular diffraction patterns. (c) Schematic top view of the 1L T'-$MoTe_2$ crystal. The *a*-axis is aligned with the zigzag direction. The Mo-Mo zigzag chains are highlighted by blue lines. The mirror plane which is perpendicular to zigzag chains is shown as a red line. The unit cell is denoted as a light-blue rectangle.

We note that the 1L T'-TMDCs are extremely sensitive to the air, especially to the water. We thus need to passivate the flakes by covering by either graphene or hBN flakes. For CVD sample, we apply the CVD graphene for passivating 1L T'-$MoTe_2$, which is firstly grown on a Cu foil substrate by CVD. It was then transferred off the Cu foil substrate by bubble transfer method with a NaOH solution and left afloat in a DI water bath. Following the growth of 1L T'-$MoTe_2$ by CVD, the sample is briefly dipped inside the DI water bath and the graphene is instantly pulled over the chip to cover the 1L T'-$MoTe_2$. The graphene/1L T'-$MoTe_2$ stack is then immediately dried with N_2 gun. Through this quick passivation method, the 1L T'-$MoTe_2$ flakes are in air and water for a handful of seconds which minimizes the degradation. For exfoliate sample, we protect sample by covering fL-hBN flakes with dry transfer technique, as we mentioned in Chapter 2.1. After passivation, the sample is then transferred to a microscopy cryostat and pump to high vacuum (10^{-6} Torr) for further protection by removing the residue water molecules in/on the SiO_2.

5.3 Raman Fingerprint of High-quality 1L T'-TMDCs

With the knowledge of the zigzag atomic chain direction, we proceed with Raman scattering measurements on the 1L T'-TMDCs, paying special attention to the angular dependent intensity of modes under different angle between directions of the $MoTe_2$ *a*-axis and the light polarization. In Figure 0.3 we display the representative polarization resolved Raman spectra of 1L T'-TMDC in four different scattering configurations of HV and HH at $\theta = 0°$ and 45°. (See Chapter 2.2.3 for experimental setup and notations) Following the naming conventions used in Chapter 4 for bulk T'-$MoTe_2$, we are able to

assign all the Raman active peaks we observe in the high quality samples. In 1L T'-$MoTe_2$, we observe in total nine zone-center optical phonons, including six 'm-modes' (m^{85}, m^{113}, m^{128}, m^{164}, m^{253} and m^{270}) and three 'z-modes' (z^{92}, z^{102} and z^{190}); in 1L T'-WTe_2, there are six 'm-modes' (m^{86}, m^{120}, m^{136}, m^{164}, m^{213} and m^{217}) and three 'z-modes' (z^{88}, z^{109} and z^{163}). The high-quality of samples enable us to reveal the complete set of nine even-parity zone-center optical phonons, providing reliable fingerprints for 1L T'-TMDCs.

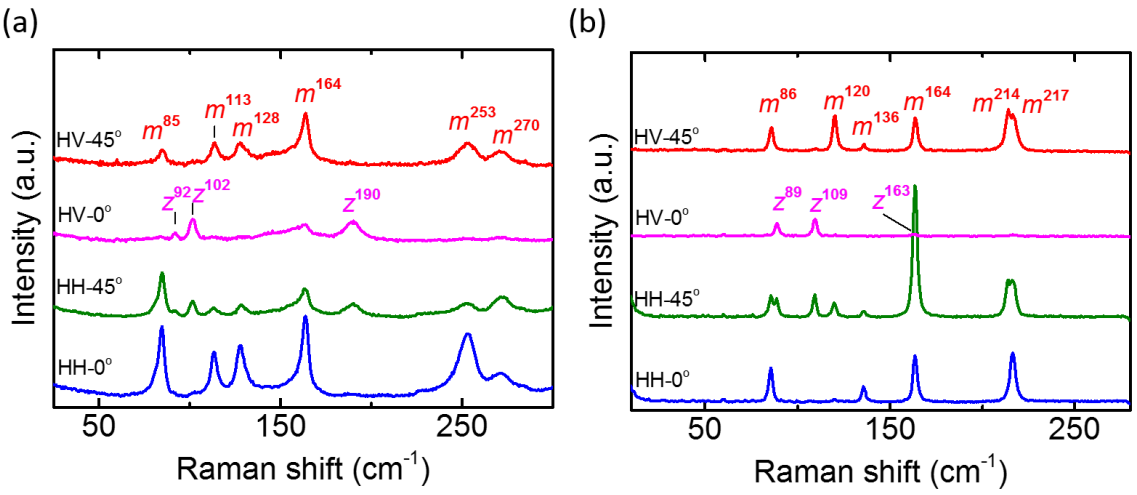

Figure 0.3: Polarization resolved Raman spectra of (a) CVD 1L T'-$MoTe_2$ and (b) exfoliated 1L T'-WTe_2.

The assignment and classification for the nine Raman bands can be understood from symmetry considerations. In Figure 0.4a we plot the top and side views of 1L T'-$MoTe_2$ together with its unit cell and symmetry operations. The primitive unit cell, denoted as the shaded area, contains six atoms, resulting in 18 Brillouin zone center (Γ) phonons. The atomic displacements of these phonons are illustrated in Figure 0.4c. Symmetry operations of the crystal include, in addition to translations, identity (*E*), inversion (*i*), mirror reflection (*m*), and a screw axis along the zigzag Mo chain (2_1^z) that form the C_{2h} group. Similar to the bulk T'$_{mo}$-$MoTe_2$, 1L T'-TMDC is centrosymmetric with its inversion centers in the center of atomic layer (yellow dots in Figure 0.4a). For this reason, half of the 18 zone-center vibrations have even-parity and the other half have odd-parity. Since in crystals with inversion centers the even Raman-active and the odd infrared-active modes are mutually exclusive, the nine modes we observe are in fact, the maximum number of zone-center optical phonons that are allowed to appear in the Raman spectra. Another important symmetry of 1L T'-$MoTe_2$ is the mirror reflection operation (the mirrors are parallel to the *b*-*c* plane perpendicular to the zigzag direction; see red lines in Figure 0.4a). We note that this mirror plane operation is also shared by fL and bulk T'-TMDC polytypes [29], and thus provides a generic way to categorize phonons as: *m*-modes, atomic vibrations in the mirror plane; and *z*-modes, atomic vibrations perpendicular to the mirror plane.

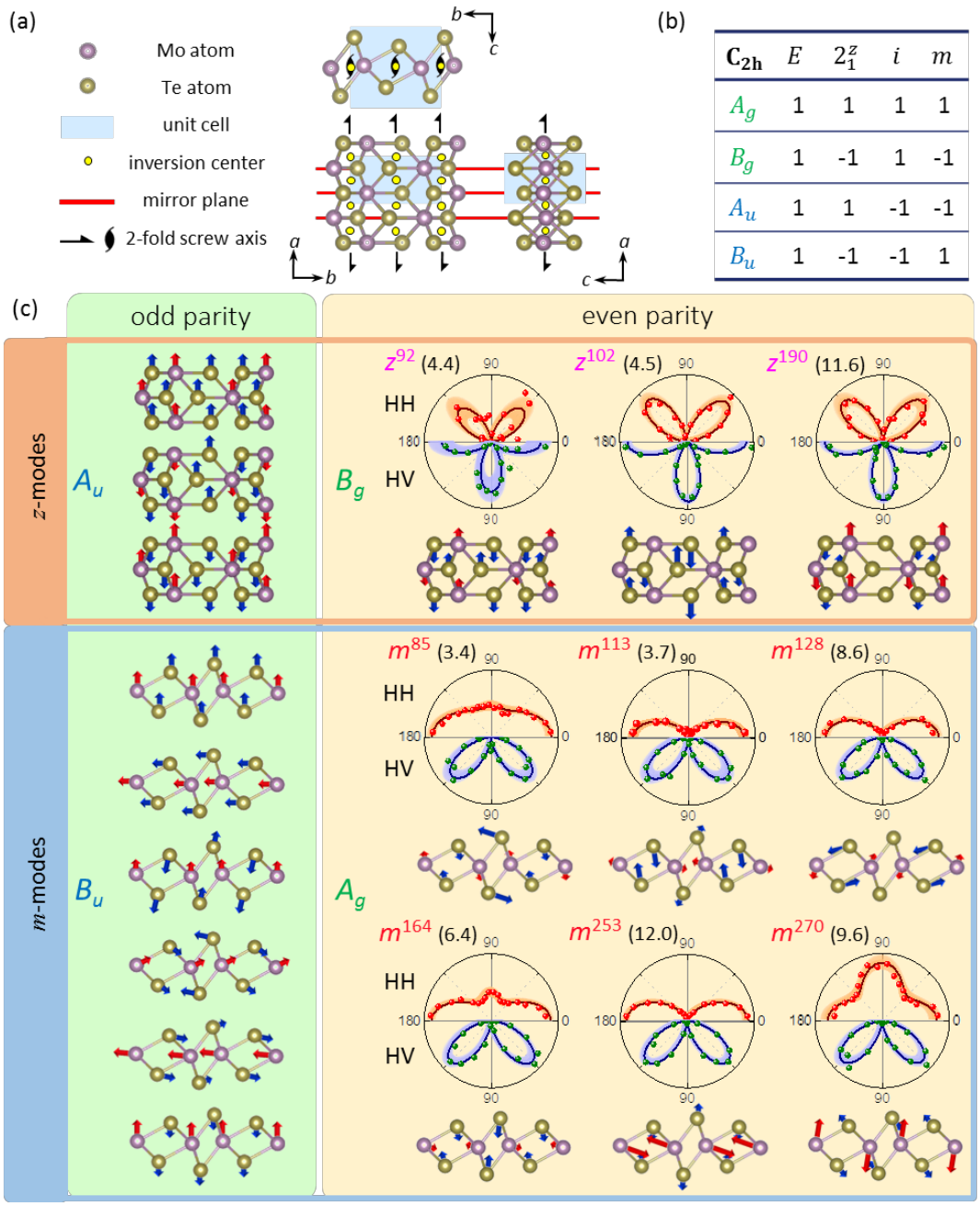

C_{2h}	E	2_1^z	i	m
A_g	1	1	1	1
B_g	1	-1	1	-1
A_u	1	1	-1	-1
B_u	1	-1	-1	1

Figure 0.4: (a) Top and side views of 1L T'-$MoTe_2$ atomic arrangement. The unit cell and the symmetry operations are illustrated on top of the schematic drawings. (b) Character table of the C_{2h} group. (c) The schematics of all zone-center normal modes categorized into 4 groups with different symmetry: *z*-modes with odd parity belong to A_u symmetry; *z*-modes with even parity belong to B_g symmetry; *m*-modes with odd parity belong to B_u symmetry; and *m*-modes with even parity belong to A_g symmetry. The intensity angular dependences of the 9 Raman-active modes are plotted above the corresponding lattice vibrations. The FWHM of each mode is included in the parentheses.

5.4 Raman Signature of Degradation in 1L T'-$MoTe_2$

The Raman data in Figure 0.3 are taken on flakes with the best quality. We have found that there is a correlation between optical contrast and sample quality: as can be seen in Figure 0.1a, the atomic flakes on the Si/SiO_2 substrate have similar shape but different darkness, and in general darker samples are of better quality. The variations of optical contrast and sample quality in certain areas on the silicon chip are likely due to non-uniform passivation from either water residue left during the transfer process or incomplete protection due to the voids and cracks in the CVD graphene that were either innate from growth or created during the transfer process.

Raman spectroscopy has been demonstrated in great success to probe the defects in atomic layered graphene [94]: i.e. the intensity of D band and the linewidth of G band provide signatures of sample quality. However, for atomic layered TMDCs, the Raman spectroscopic evidence for sample degradation is still lacking. In this section, we study the Raman spectra from four selected flakes from S1 to S4 as shown in a which exhibit different optical contrast. The relation between optical contrast and sample quality is commonly employed in other air sensitive 2D materials [95,96]. In the lower panel of Figure 0.5b, we display the Raman spectra of four flakes with different optical contrast from S1 to S4 denoted in panel a. Sample S1 is has `best' contrast and the Raman features are similar to the data in Figure 0.3, indicating the high sample quality. In contrast, sample S4, which is poorly passivated and has `poorest' contrast, displays distinct Raman spectra from S1: the intrinsic Raman features of 1L T'-$MoTe_2$ are vanishing and instead, two intense new peaks (labeled as A to B) between 100 and 150

cm^{-1} show up. Meanwhile, samples S2 and S3 displays coexistence of Raman features from 1L T'-$MoTe_2$ and from the sample degradation.

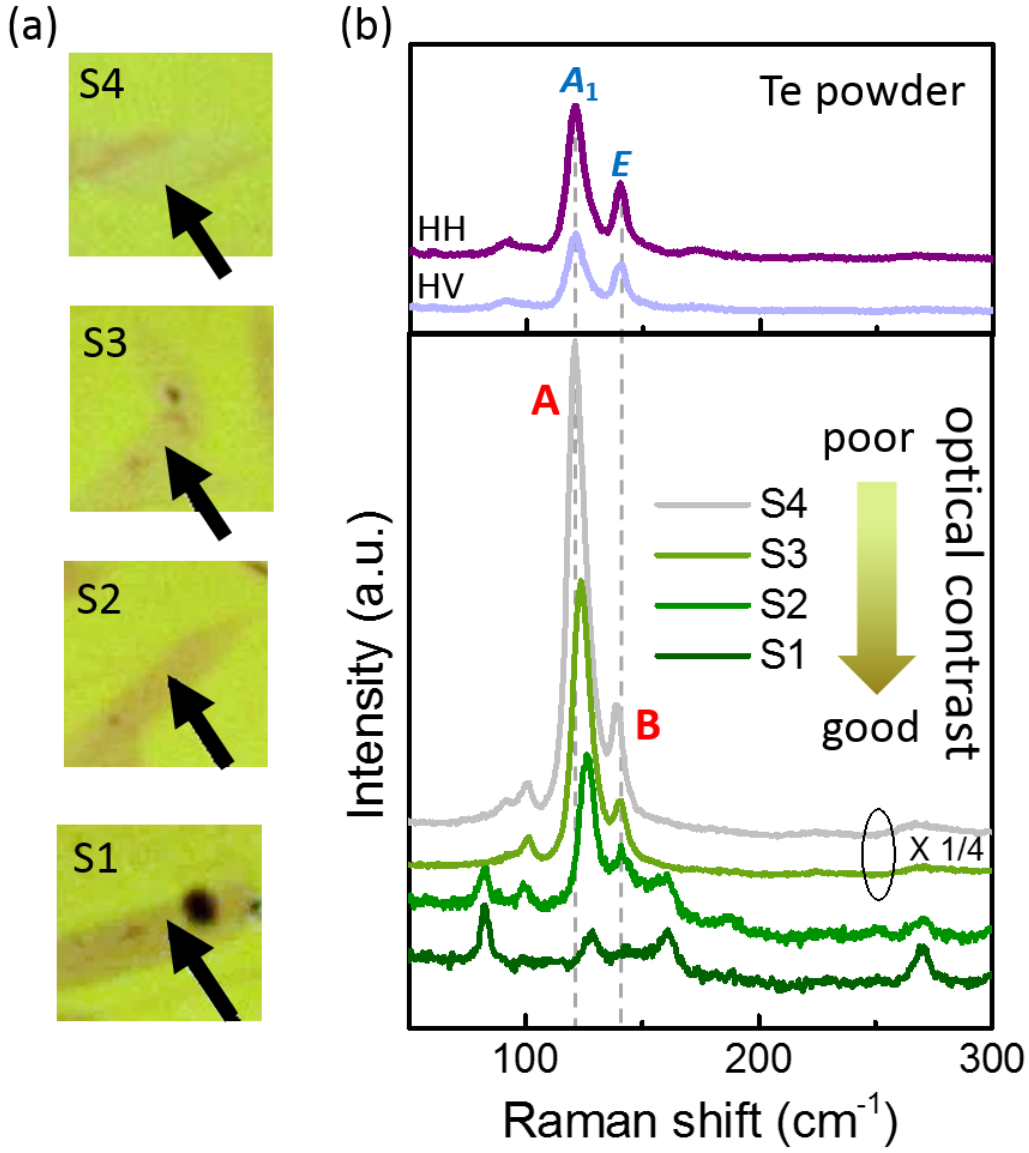

Figure 0.5: (a) Optical micrographs of selected 1L T'-$MoTe_2$ with different optical contrast: S1 to S4 from good to poor contrast. The arrows point to the positions where Raman spectra were collected. (b) Lower panel: the Raman spectra for samples S1 to S4. The spectra are shifted vertically for clarity. The Raman spectra from Te powder are plotted for comparison in the upper panel.

To understand the origin of these new peaks, we also measure the Raman spectra of tellurium powder (Sigma-Aldrich 99.997%); see the upper panel of Figure 0.5b The Raman spectra of Te powder show two prominent modes A_1 and E (following the naming convention in literatures), [97,98] corresponding to the Te breathing vibration in the basal plane and asymmetric stretching vibration along the c-axis, respectively. These are consistent with the A and B modes we observe in sample S4, suggesting that Te metalloids are likely a by-product of $MoTe_2$ degradation. We note that there are some small energy differences between the Raman peaks in Te powder and degraded $MoTe_2$: peak A has slightly higher energy in degraded $MoTe_2$ and redshifts from 128 cm^{-1} in S2 to 122 cm^{-1} in S4, approaching the 121 cm^{-1} peak in Te powder, suggesting different Te cluster sizes in S2 to S4 [99,100]. We note that this peak could overlap with the m^{128} mode in 1L T'-$MoTe_2$; however the former is typically much more intense and thus might be mistakenly assigned to the intrinsic Raman feature of 1L T'-$MoTe_2$ [101]. While the Te-like side peak B (~142 cm^{-1}) shows up in the energy range which is spectrally clean in the intrinsic spectrum (this is also true for WTe_2), acting as a handy tool to gauge the sample quality in bulk and atomically thin T'-(Mo, W)Te_2.

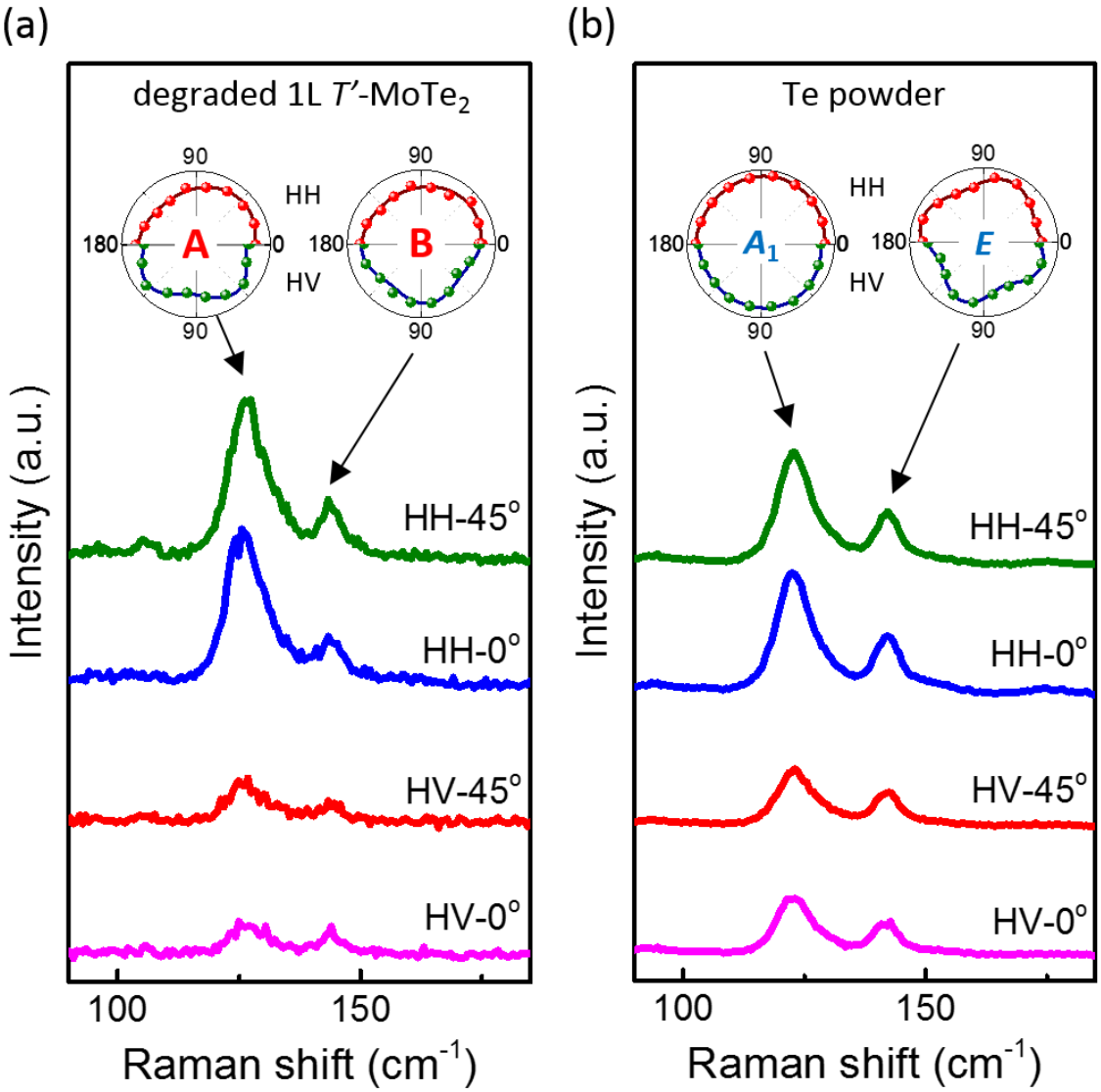

Figure 0.6: The Raman spectra of (a) the poor quality 1L T'-$MoTe_2$ and (b) Te powder in HH or HV configuration with $\theta = 0°$ and 45°. The angular dependences of intensity for peaks A and B of degraded 1L T'-$MoTe_2$ and A_1 and E for Te powder are shown in the inset.

To confirm that the Raman peaks A and B are indeed due to sample degradation we thus collect polarization and angular dependent data from the degraded sample. As can be seen in Figure 0.6a, the spectra taken at $\theta = 0°$ and $45°$ are almost identical in either HH or HV, similar to the ones we acquired on Te Powder (Figure 0.6b), but in drastic contrast to intrinsic 1L T'-$MoTe_2$ peaks. The detailed angular dependence of peaks A and B are shown in the insets of Figure 0.6a; these are to be compared with the angular dependence of the *z*- and *m*-modes in Figure 0.4c, confirming that peaks A and B have very different symmetry properties. We also performe similar polarization-resolved measurements on the A_1 and E modes of Te powder as shown in Figure 0.6b, which reflect the polycrystalline nature of the Te powder. The angular dependences of the two are similar, substantiating our speculation that the new peaks A and B in degraded T'-$MoTe_2$ are due to chemical reactions that generate clusters of Te metalloid.

5.5 Excitation Power Control of the Degradation

To further understand the degradation rate of samples in different quality, we perform a set of controlled experiments using *in situ* Raman scattering to monitor sample degradation in ambient conditions. Figure 0.7a and b show the time evolution of Raman spectra of a 'good' and a 'poor' sample. The spectra are recorded continuously in 30-second step for 5 minutes and the laser power is kept at 1mW focused to a spot size of about 1μm. In both samples, we observe increasing intensity of Te-like modes A and B as time goes but with different rates. For the 'good' sample, the intensity of Te-like modes grows while that of peaks due to 1L T'-$MoTe_2$ decreases slowly. For the 'poor' sample, those 1L T'-$MoTe_2$ modes disappear almost completely after the first 30 seconds; while

the Te-like modes keep increasing and getting more and more intense, reaching more than twice the intensity of silicon peak in five minutes.

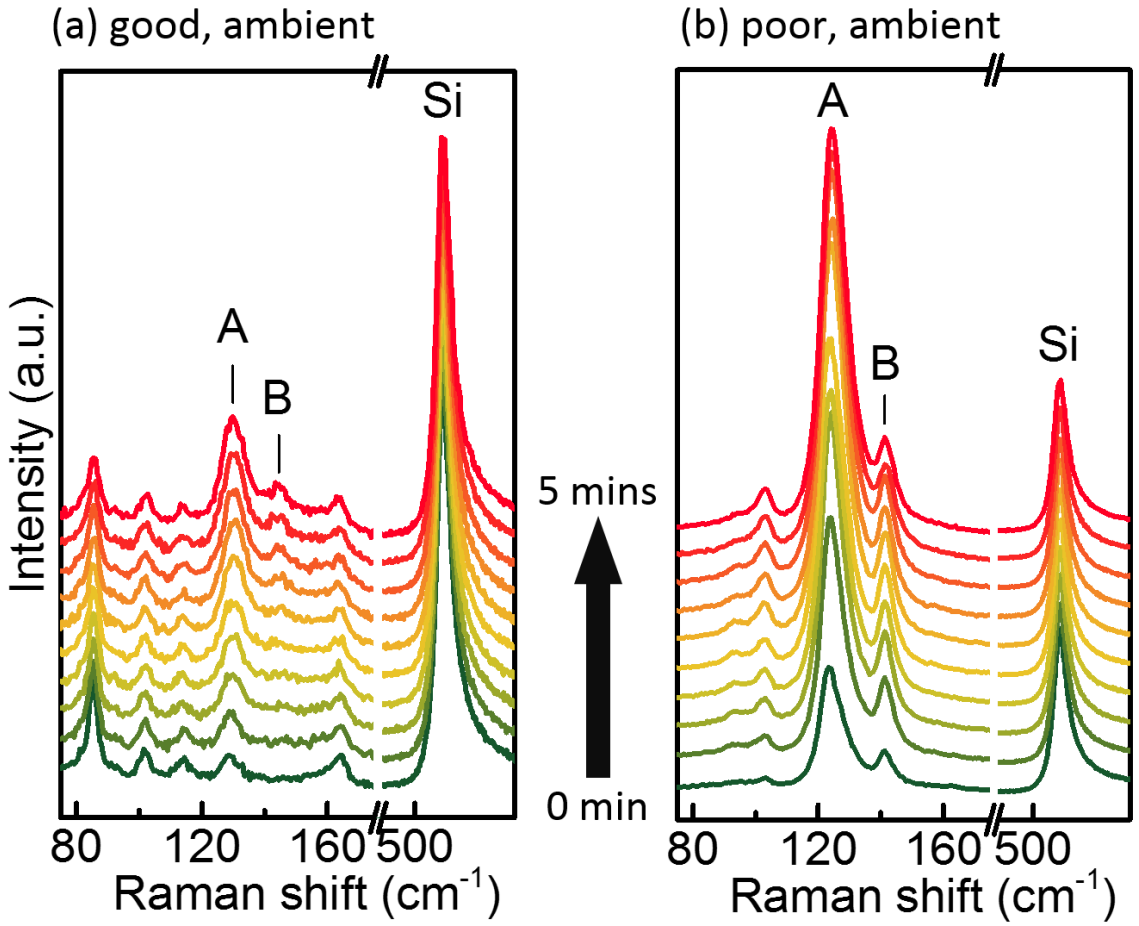

Figure 0.7: Spectral evolution of samples with (a) good (similar to S1 in Figure 0.5a) and (b) poor (similar to S4 in Figure 0.5b) optical contrast in ambient.

Quantitatively, we summarize in Figure 0.8a the evolution of the intensity ratio of mode A to the silicon phonon at 520 cm^{-1} for the three *in situ* Raman measurements. For the 'good' sample the Te(A)/Si ratio increases slowly; for the 'poor' sample, the Te(A)/Si ratio increases rapidly and saturates after 4 minutes. As a controlled comparison, we also conduct similar *in situ* Raman monitoring on a 'good' sample that was placed in the high

vacuum pumped for a week at 3×10^{-6} torr. In this sample, no additional Te-like modes were seen in 5 minutes, indicating negligible degradation. Furthermore, we also examine the linewidth and intensity of the m^{85} mode in Figure 0.8b. The increase of FWHM from 3.4 to 4.6 cm^{-1} during the 5 minutes indicates the degradation of sample crystallinity, correlated with the intensity decrease which is consistent with previous degradation studies of air sensitive 2D materials [90,102,103].

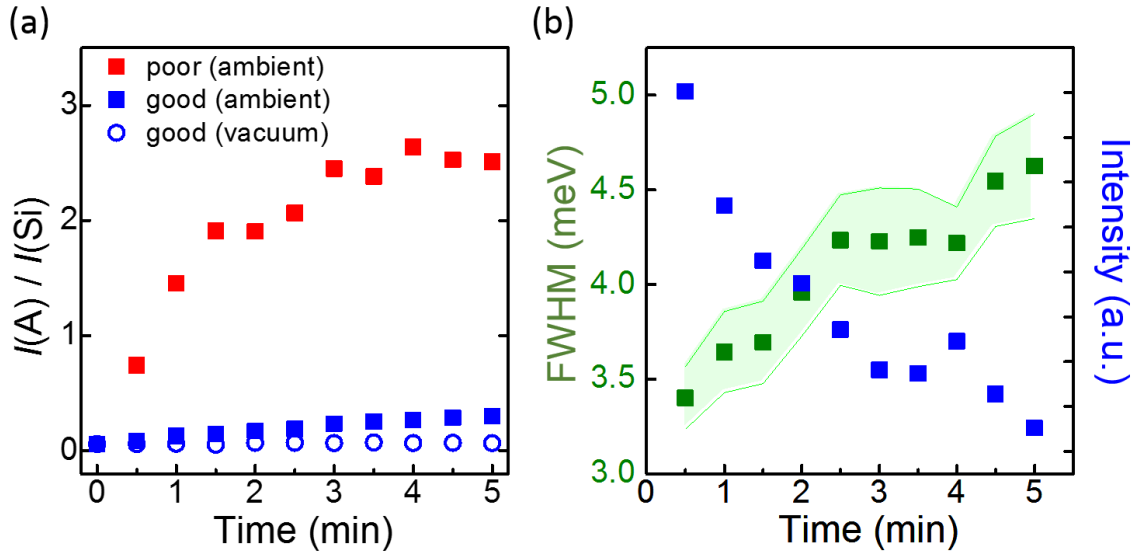

Figure 0.8: (a) The intensity ratio of peak A to the silicon mode plotted as a function of laser exposure time. (b) the evolution of FWHM and intensity of the m^{85} mode.

5.6 Summary

In conclusion, the lattice dynamic of CVD 1L T'-$MoTe_2$ and exfoliated 1L T'-WTe_2 are investigated by the polarization and crystal orientation resolved Raman spectroscopy. We observed the complete set of zone-center Raman-active modes including 3 *z*-modes and 6 *m*-modes, providing Raman fingerprints for high-quality 1L T'-TMDCs. By monitoring the intensity of Raman features due to sample degradation, which are attributed to the Te-metalloid like phonons, we are able to quantitatively gauge the quality the 1L T'-$MoTe_2$ crystal. Our work represents a solid advance in understanding the fundamental properties of T'-TMDC and provides a metrological tool for monitoring the quality of electrochemical and/or topological devices developed with T'-$MoTe_2$.

CHAPTER 6

MULTI-PARTICLE BOUND EXCITONIC STATES IN 1L-WSE_2

6.1 Introduction and Motivation

Many-body correlation is a fascinating topic that has attracted decades of experimental and theoretical investigation. In condensed matter systems, *ab initio* simulations are so far lacking for addressing complexes with three or more charged particles; and experimentally light emissions due to exciton molecules, or biexcitons, are only revealed in a few systems, such as carbon nanotubes, GaAs, CuCl and GaN [104–107]. In addition, the multi-particle bound states more than 4 particles are never realized experimentally. In this chapter, we demonstrate that 1L-WSe_2 is an outstanding platform to investigate the many-body interaction. We report the experimental observation of optical features due to multi-particle bound states in 1L-WSe_2. We observe that the four-particle biexciton as well as the five-particle exciton-trion. Several controlled experiments have been demonstrated to confirm our assignments, including power dependent, charge doping dependent, temperature dependent and magnetic field dependent PL. Most interestingly, the magnetic field dependent PL reveals the unique spin and valley configurations for biexciton (exciton-trion): a dark exciton in one valley and a bright exciton (intravalley trion) in another valley. This unique intervalley configurations for biexciton and exciton-trion result in the anomalous valley polarization that has an opposite sign compared to the well-known bright exciton in a magnetic field [108,109]. Our findings shed new light on many-body physics of transition metal

dichalcogenides, and pave way for developing new valleytronic devices and spin-valley entangled photon sources.

6.2 Many-body Correlated Excitonic States in 1L-WSe_2

Figure 0.1 shows a typical luminescence emission spectrum at 4 K from a high-quality hBN/1L-WSe_2/hBN sample. We observe several intrinsic features from the sample in the energy range of 1.64–1.72 eV. The peak with the highest energy is the two-particle bright exciton X (full width half maximum (FWHM): 3.4 meV, which is among the narrowest for WSe_2 monolayers [110–112]), consisting of an electron and a hole residing in the same valley with opposite spins (see Figure 0.2 for the corresponding spin-valley configurations). This spin-zero bound state has been widely studied, which carries opposite angular momentum of $\pm\hbar$ in the K and K' valleys, giving rise to valley-selective coupling with circularly-polarized optical excitation [10].

The bright exciton can further bind an electron in the same or the opposite valley to form negative trions (noted as T_1/T_2 in Figure 0.2). Our as-made sample is slightly electron doped, and indeed, we observe T_1 and T_2 emissions at 29 and 36 meV below X (FWHM: 3.6 and 3.7 meV for T_1 and T_2 respectively), attributable to the negatively charged trions [113]. The 7 meV difference in energy has been attributed to that the electron-electron interaction induced splitting in the intravalley and intervalley trions [114]. Furthermore, the bright exciton can also bind a hole and form the positive trions T^+ with the binding energy about 20 meV.

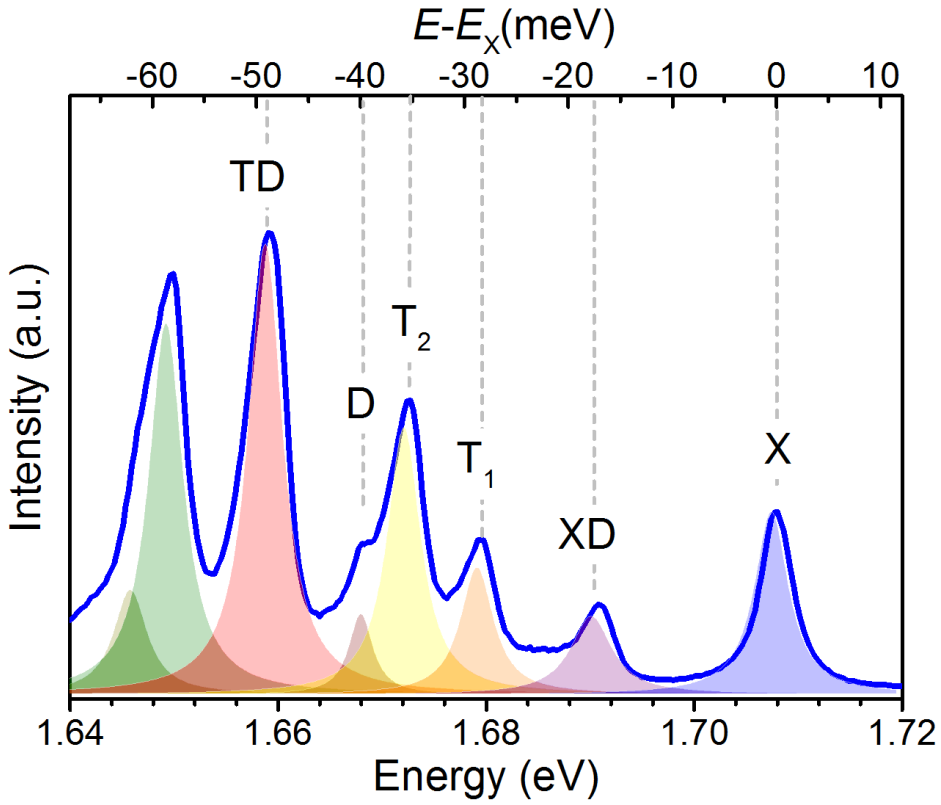

Figure 0.1: The typical luminescence spectrum of 1L-WSe_2 excited by 2.33 eV at 4K. Several bound excitonic states are assigned from high to low energy as bright exciton (X), biexciton(XD), negative trions (T_1/T_2), dark exciton (D) and exciton-trion (TD).

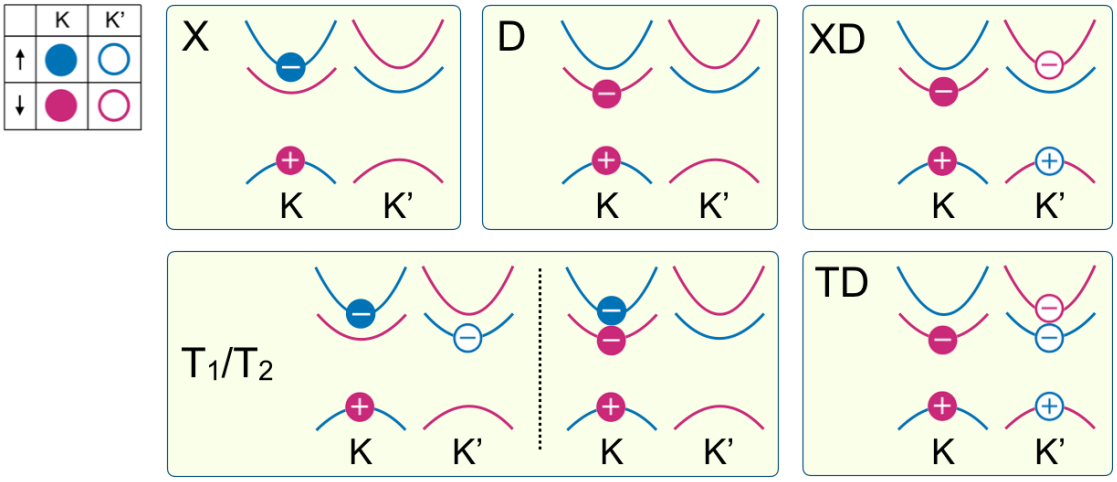

Figure 0.2: The corresponding valley-spin configurations of the bound states shown in Figure 0.1. The spin and valley are encoded by different colors and symbols: blue(red) for spin up (down); close (open) for K (K') valley.

While being the most prominent and well-known optical feature in transition metal dichalcogenides [11,12,115], it is important to note that energetically in 1L-WSe_2, the bright exciton X is not the two-particle ground state of the system due to the particular spin ordering of the conduction band with respect to that of the valence band [21]. Instead, the dark exciton D, the electron and hole have the same spin and reside in the same valley, is energetically more favorable [116]. In the out-of-plane direction, the dark exciton is optically silent (hence the name). However, with finite in-plane magnetic field [22] or momentum [24], D becomes visible. While our experimental setup is in back-scattering geometry, the finite collection solid angle (numerical aperture NA=0.35) and the high quality of our sample enabled us to observe this optical feature in Figure 0.1, located about 40 meV below X (FWHM: 2.0 meV), as a result of the conduction band splitting and the distinct many-body interactions [22].

The remainder two emission features in Figure 0.1, denoted as XD at 18 meV and TD at 49 meV below X (FWHM: 3.6 and 3.9 meV for XD and TD respectively), are assigned as the biexciton four-particle state and the exciton-trion five-particle state respectively. XD peak, observed in the first time, can only be resolved in the high-quality sample. We assign it as a 4-particle bound state composed by a bright exciton in one valley and a dark exciton in another valley. The TD peak, however, has been observed in a previous study and attributed to the biexciton [117]. This assignment however, is being debated due to the inconsistency with theoretical calculations, in particular the anomalously large binding energy [118–122]. As illustrated in Figure 0.2, instead of biexciton, we assign TD as a five-particle bound state involving a dark exciton in one valley and an intravalley trion in another valley.

6.3 Power Dependence of XD and TD Emission

The nonlinear relation of the emission and excitation power is the one characteristic has been observed in the biexciton in other system [104–107]. In Figure 0.3, we plot the normalized PL spectra under various excitation power density from 0.32, 3.2 to 130 W/cm^{-2}. As can be seen, the XD and TD peaks are vanishing in lowest power and grow nonlinearly with higher power. Quantitatively, we further extract the intensity of X, XD and TD as a function of the incident laser power in log-log scale as shown in Figure 0.3b. In contrast to X whose intensity is nearly proportional to the incident power, both XD and TD intensities rise more steeply (black dashed and dotted lines in Fig.1c are drawn as $P \propto I$ and $P \propto I^2$ respectively). providing a first evidence that they arise from higher order complexes in the system. Meanwhile it is quite extraordinary that these nonlinear features are readily observable with continuous wave (cw) laser excitation as low as 10 μW.

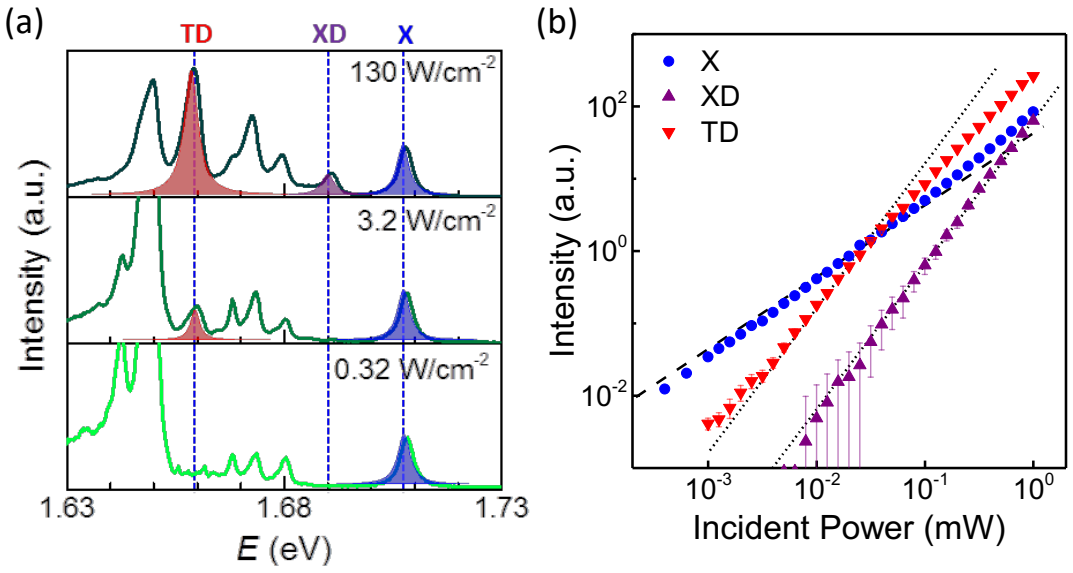

Figure 0.3: (a) The PL spectra with excitation power of 0.32, 3.2 and 130 W/cm^{-2}. The spectra are normalized by the intensity of X to show the nonlinearity of the XD and TD. (b) The intensity of X, XD and TD bound states plotted as a function of excitation power. The dashed (dot) lines in the figure are the guide of $P \propto I$ ($P \propto I^2$).

6.4 Gate Dependence of XD and TD Emission

To gain further insights into the nature of XD and TD, we fabricate a field effect transistor (FET) device using the bottom hBN as the gate dielectric and a graphene as a back gate electrode. (see the device schematic in Figure 0.4a) and investigate the gate voltage dependence of its luminescence. By applying the voltage on the gate electrode, we can modify the charge density in the material, which can be approximately modeled by the parallel capacitor model. Figure 0.4b displays gate voltage and emission energy mapping of the luminescence intensity at 100 μW excitation power over a wide tuning range from –2 to 1 V. It is evident from these mappings that all the emission features are intrinsic from 1L-WSe_2 and highly sensitive to charge doping. Similar to the sample in Figure 0.1, our FET device also has minor electron doping at $V_g = 0$ V, and we observe strong T_1, T_2 and TD emissions in the absence of any gate induced charge carriers. As we remove electrons from the crystal by applying a negative gate voltage, T_1, T_2 and TD rapidly decrease in intensity while X becomes stronger as the sample becomes more charge neutral. Concomitantly, the dark exciton D and the biexciton XD also become prominent. At even more negative gate voltage, D and XD disappear, and X becomes significantly broadened, accompanied by the appearance of a new emission peak at about 1.71 eV attributable to the positive trion excitation, indicating that the sample is doped by holes in this gate voltage range [123]. These observations suggest that XD is a charge neutral entity while TD is associated with electron doping.

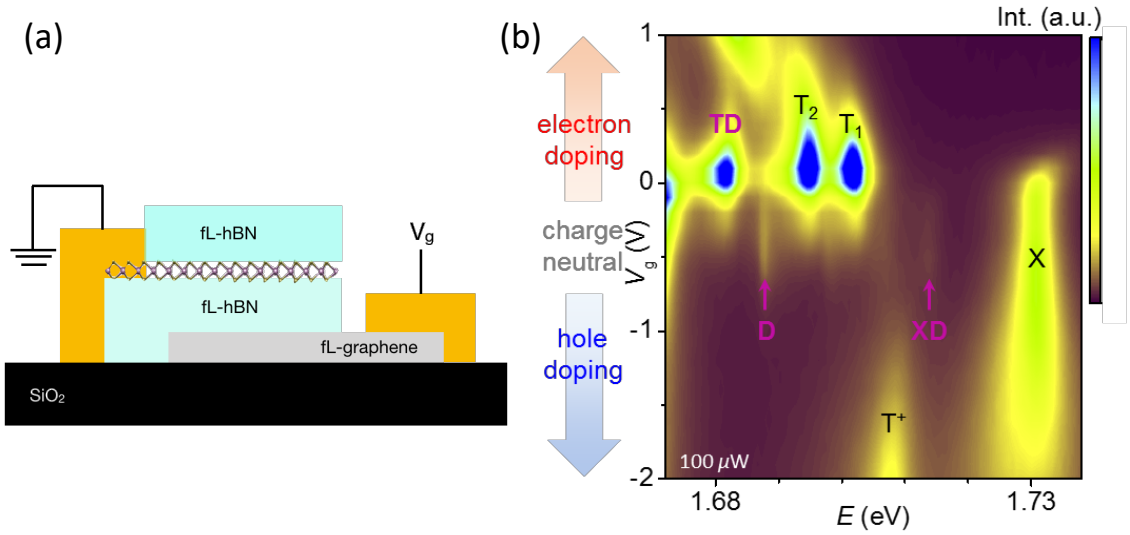

Figure 0.4: (a) Schematic of graphene back gate FET device. (b) The color map of PL spectra excited at 2.33 eV at 3K plotted as a function of gate voltage. The assignments of exciton complex are denoted on the figure.

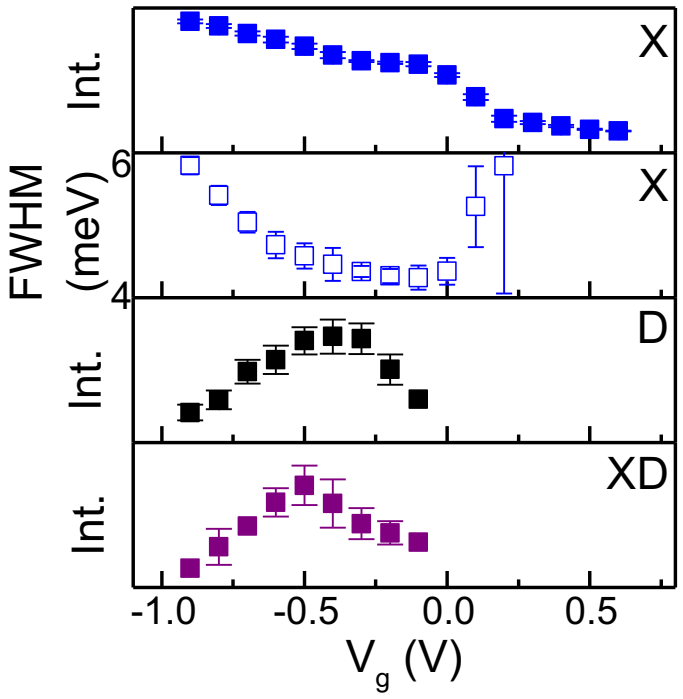

Figure 0.5: The extracted gate dependent intensity of X, D and XD. The last panel shows the gate dependent FWHM of X.

To be more quantitative, we have extracted the intensity of various emission features as a function of gate voltage in Figure 0.5. XD is found to appear only when the X linewidth is narrow and its intensity scales with that of D. Combined with the fact that XD is a charge neutral nonlinear optical feature, we attribute it to be a biexciton consisting of a bright and a dark exciton. This assignment is distinct from previous FWM measurements [124,125] where two bright excitons are involved. Our biexciton is unlikely to arise from the binding of two X excitons. For a cw excitation power of about 10 μW focused to a 2 μm spot, assuming an absorption of about 10% and X exciton lifetime of 2 ps [126,127], the bright exciton density is estimated to be 1.7×10^{8} cm^{-2}. Equivalently, the average X-X separation is 0.77 μm, which gives little chance for the bright excitons to meet each other before decaying through other channels. The dark exciton, on the other hand, is the lowest energy 2-particle state in the system (the intervalley version of D has the same kinetic energy, but the exchange interaction raises its energy by ~10 meV above D), and its lifetime is several orders of magnitude longer than that of the bright exciton [22]. It is thus quite reasonable to conjecture that multi-particle bound states prefer to involve D excitons at low temperatures. We rule out the possibility of the XD emission to be two D excitons bound together, since the emission energy is higher than the D exciton which would otherwise suggest a negative binding – a state that is energetically unfavorable. The assignment of XD as a charge-neutral biexciton is further supported by theoretical calculations. Several independent simulations have consistently found that the biexciton binding energy in WSe_2 is about 18–20 meV [118–122], which agrees well with our observed XD to be ~18 meV below X.

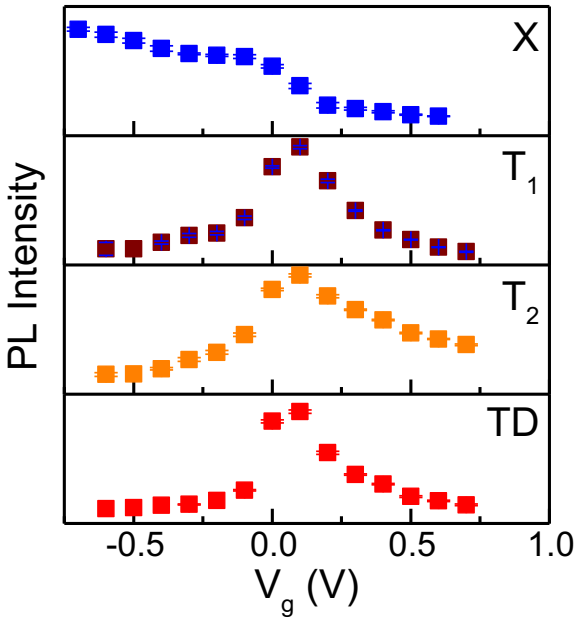

Figure 0.6: The extracted gate dependent intensity of X, T_1, T_2 and TD.

Now we turn to the gate dependence of the TD peak. From our data in Figure 0.6, the intensity of TD follows the rising and lowering of the intensities of T_1 and T_2, suggesting that the underlying excitation is linked to the trions. Because D is the two-particle ground state as discussed above, we conjecture that TD results from the binding of a trion with a dark exciton. Theoretically the binding energy of the exciton-trion five-particle state in 1L-WSe_2 has been calculated to be ~12–15 meV [120]. We note that if we count the TD binding energy from the X emission, the value of 49 meV is three to four times too large compared to the theory. However, we believe this is not a legitimate counting since the TD complex does not involve X directly. Instead, the TD binding energy should be given by $\Delta_{TD} = E_T + E_D - E_{TD}$. We assume that the emission we observe is due to the dissociation of TD into a dark exciton and a trion, which radiatively recombines subsequently. Thus, the emission energy is given by $\hbar\omega_{TD} = E_{TD} - E_D =$

$E_T - \Delta_{TD} = \hbar\omega_T - \Delta_{TD}$, i.e., the TD binding energy needs to be counted from the trion emission energy. Indeed, the energy separation between TD and T_2 is 13 meV, in excellent agreement with theoretical calculations.

6.5 Temperature Dependence of XD and TD Emission

The binding energies of XD and TD are further confirmed by thermal activation measurements. In Figure 0.7, we plot the temperature dependence of 1L-WSe_2 photoluminescence. The XD and TD peaks are found to be highly sensitive to sample heating and they disappear in the temperature range of 100 to 130 K. In contrast, the neutral exciton and the negative trion emissions survive to much higher temperatures. The comparatively more robust trion emission suggests that the binding energies of both XD and TD are smaller than that of the trions, further challenging the speculation that the TD peak is bound with respect to X.

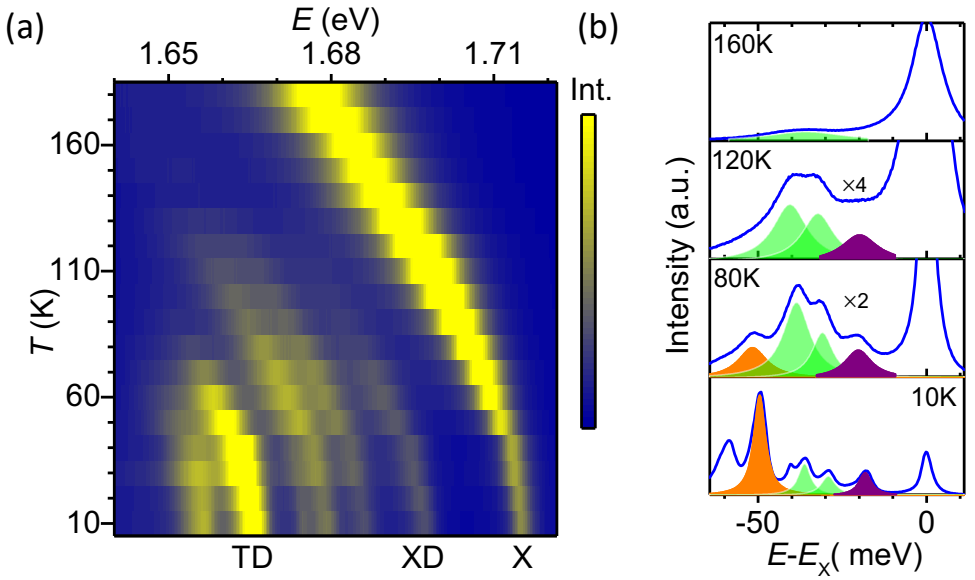

Figure 0.7: (a) The color map of PL spectra excited at 2.33eV at temperature ranging from 3K to 180K. (b) The selected spectra at different temperature showing the evolution of TD (orange) and XD (purple) states.

Quantitatively the temperature dependence of XD and TD intensities are impacted by both the formation and the disassociation dynamics of these highly-correlated complexes. The D exciton is the lowest energy state in the system; for temperatures below 130 K, we can assume that there are plenty of dark excitons in the crystal. This is reflected in the dramatic dropping of X intensity at low temperatures [31,116], as well as our observation of relatively strong dark exciton emission in a backscattering optical setup with relatively small NA. The formation process can thus be assumed to be determined by the population of the minority species, namely XD by X and TD by T in the system, which we approximate by the luminescence emission intensity of the neutral and charged excitons. By normalizing the intensity of XD and TD to the intensity of X and T respectively, we quantitatively characterize the thermal dissociation of XD and TD as a function of temperature in Figure 0.8. This thermally activated disassociation can be captured by using the thermal activation equation considering only one binding energy:

$$I = \frac{I_0}{1+Ae^{-\frac{E_b}{k_B T}}} \qquad \text{(Eq. 6.1)}$$

where I_0 is the intensity at 0 K, E_b is the binding energy, k_B is Boltzmann constant, and A is a fitting constant. Using Eq. 6.1 to fit our experimental data, we find that the binding energy of XD and TD to be 18–23 meV and 13–20 meV respectively. These values are in reasonable agreement with the theoretical calculations [118–122] as well as the binding energy counting alluded above.

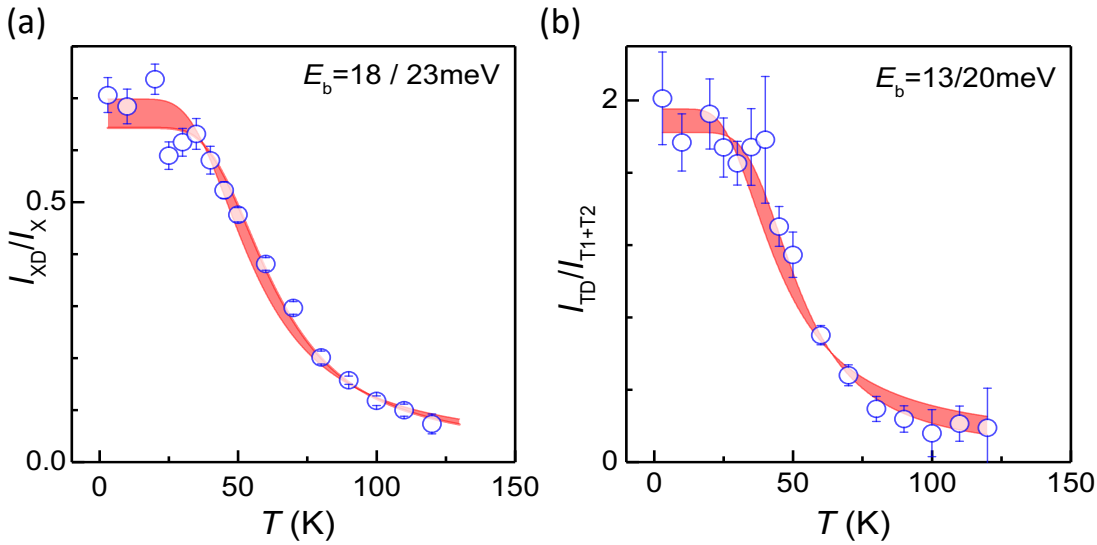

Figure 0.8: The normalized intensity of (a) XD and (b) TD are plotted as a function of temperature. The decrease of intensity reveals the thermal activated dissociation with corresponding binding energies.

6.6 Zeeman Effect: The Magnetic Dipole Moments in 1L-WSe_2

The biexciton and the exciton-trion complexes possess remarkable valleytronic properties. In the magnetic field control experiments, we use a linearly-polarized laser at 2.33 eV to excite our sample placed in an out-of-plane magnetic field, and collect the resultant luminescent emission in a circular-polarization resolved optical spectroscopy setup (see Figure 0.9c and Ref [27]) The off-resonance laser excitation with linear polarization populates K and K' valleys of 1L-WSe_2 equally with electrons and holes. The electronic states at the K and K' valleys are degenerate and can be lifted in an out-of-plane magnetic field because the electronic states in two valleys have opposite magnetic dipole moment [108,109]. The resulting Zeeman splitting then leads to valley polarized charge distribution, similar to the imbalanced spin occupation in a magnetic material, which can be monitored by the optical response of the system to photons of opposite circular polarization by virtue of the valley-helicity optical selection rules [10]. The

emission intensities from different channels thus reflect the degree of valley polarization of the corresponding underlying excitonic species.

Figure 0.9 shows the intensity map of σ^- luminescence for magnetic fields ranging from –8 to 8 Tesla. Both XD and TD emissions obey well the valley-helicity selection rule, namely, only the K' valley electron-hole recombination is allowed in the σ^- channel, similar to X, T_1 and T_2. In contrast, this valley-helicity locking is broken for the D exciton, and both K and K' dark exciton recombination shows up in the σ^- luminescence emission, giving rise to the cross pattern in Figure 0.9. This observation reiterates the fact that the valley-helicity locking is for angular momentum that is perpendicular to the atomic layer [10]. Instead, the D emission arises from radiation with momentum that is not perfectly perpendicular to the atomic layer; the projection of exciton spin and angular momentum to the light propagation direction allows for coupling of D in each valley to both σ^+ and σ^- radiation.

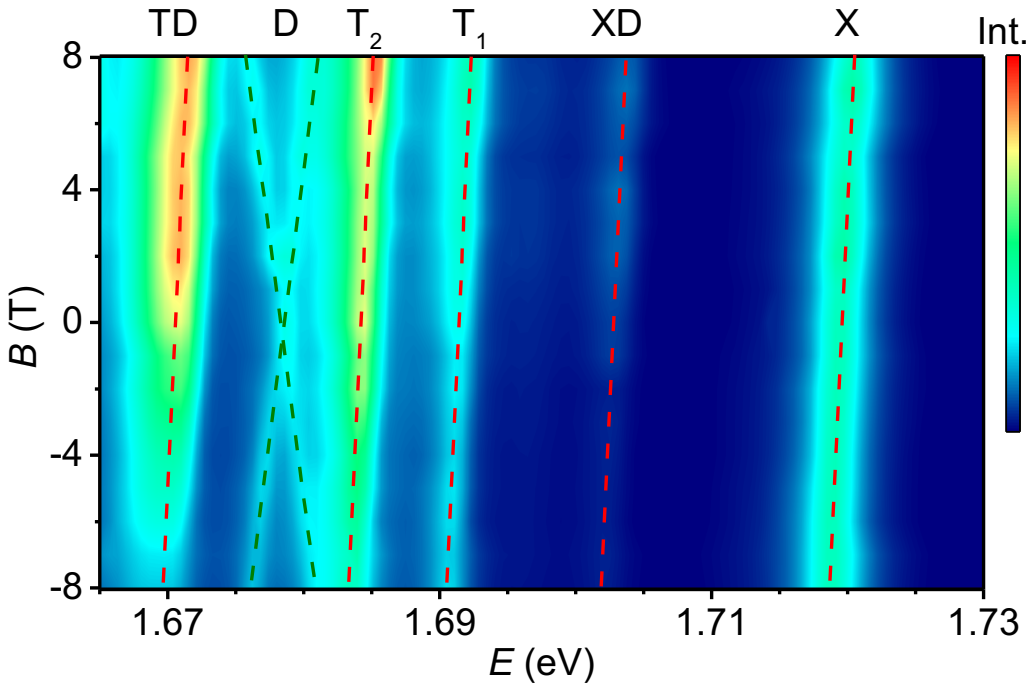

Figure 0.9: The color map of σ^- PL spectra excited at 2.33 eV in the perpendicular magnetic field from –8 to 8 Tesla.

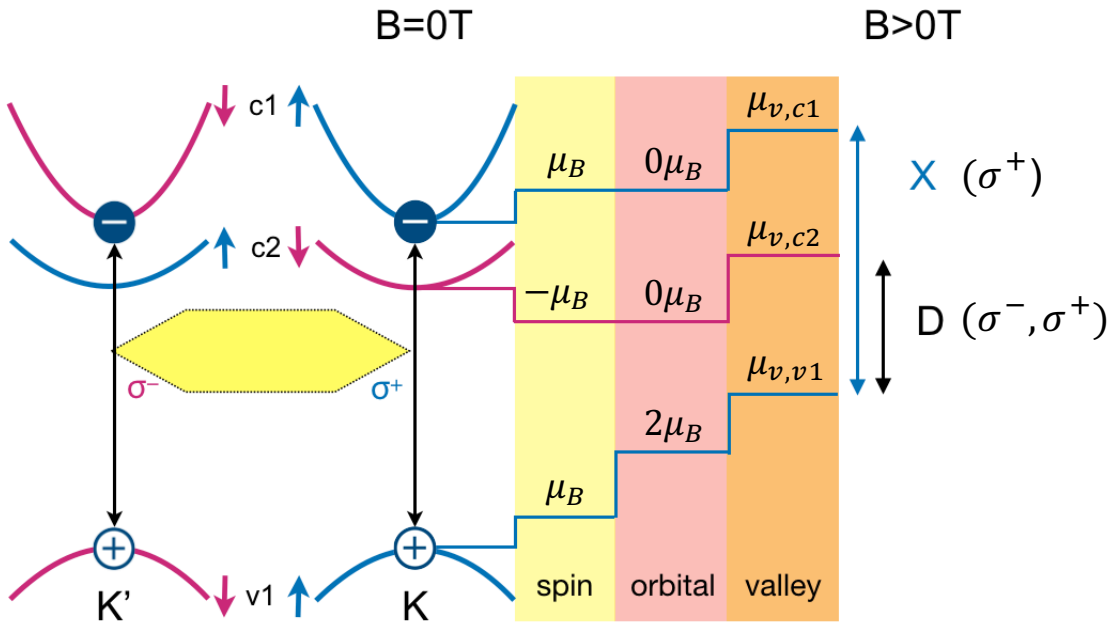

Figure 0.10: The schematic of spin-valley configurations and the Zeeman shift of X and D states at $B = 0$ T and $B > 0$ T.

The magnetic field dependent energy shift in Figure 0.9 is governed by the Zeeman effect $E_Z = \mu_{total} B,$ where μ_{total} is the total magnetic moment of the exciton in 1L-WSe_2, composing of three components from the spin, the atomic orbital, and the valley. As illustrated in Figure 0.10, $\mu_{total} = \mu_s + \mu_o + \mu_v,$ where $\mu_s = 2s\mu_B$, $\mu_o = m\tau\mu_B$; $\mu_v = \beta\tau\mu_B$; s, m and τ are quantum number of spin ($s = \pm 1$, for spin up/down), orbital (m is determined by the angular momentum of the atomic orbitals) and valley ($\tau = \pm 1$ for K or K' valley), respectively; β is the orbital contribution calculated from Barry curvature; $\mu_B = 0.058$ meV/T is the Bohr magneton. For the spin terms, the parallel spin alignment of the conduction and valence bands in the bright exciton cancel out the net magnetic dipole moment, yielding 0 μ_B for both K'/K valley. However, for dark excitons, the opposite spin configuration contributes ± 2 μ_B for K'/K valley. The total orbital terms sum up the contribution from lowest conduction band (c1) and top valence band(v1). The first principle calculation reveals that in 1L-WSe_2, c1 and c2 band are dominant by d_{z^2} ($m = 0$) orbital while the v1 band is dominant by $d_{x^2-y^2} + d_{xy}$ ($m = 2$) [21], yielding ± 2 μ_B contribution for K'/K valley. The magnetic moments contributed by the valley term are originated from the Barry curvature induced the self-rotation of electron wavepacket. Here, we apply a three-band model and assume the parabolic bands. The contribution of the magnetic moments from the Berry curvature is approximated by $\mu_v = \beta\tau\mu_B = (\frac{m_*}{m_0})\tau\mu_B,$ where m_* is the effective mass calculated for each band, m_0 is the free electron mass. By plugging the number 0.28 m_0, 0.39 m_0 and 0.36m_0 for m_{*-c1}, m_{*-c2} and m_{*-v1}, yielding the total magnetic moments in K'/K valley are ± 0.08 μ_B for X and ∓ 0.03 μ_B for D [128]. Summarizing all the contributions in Figure 0.10, we predict the *g*-factor of X and D is about 2.08 and 3.97 μ_B, respectively.

Experimentally, we can derive the *g*-factors by fitting the slopes in Figure 0.9. XD and TD have the same slope as X, T_1 and T_2, and $g = 2.17$; while g is 4.58 for D. These results are in the same trend as our prediction but slightly off in magnitude based on our models. The valley-helicity locking and the Zeeman *g*-factors of XD and TD emission exclude the physical picture where XD and TD emissions arise from radiative recombination of the disassociated dark exciton with finite in-plane momentum, and provide further evidence that the radiative emission of these four- and five-particle bound states are linked to either bright excitons or trions, supporting our interpretation of their formation and disassociation process as well as their binding energy.

6.7 Valleytronic Properties of XD and TD

Another important information regarding the valleytronic properties of XD and TD is encoded in the intensity of the Zeeman-split peaks. The off-resonance laser excitation with linear polarization we use populates both valleys of 1L-WSe_2 equally with electrons and holes. However due to the breaking of valley degeneracy, the formation probability of multi-particle bound states in the two valleys are non-equal and occupation of lower energy states is preferred. The emission intensities from different channels thus reflect the degree of valley polarization of the corresponding underlying excitonic complex.

Figure 0.11 plots the spectral intensities of X, D, XD and TD in σ^+ and σ^- channels at 8 T. For X we observe that the σ^+ emission at K valley is more intense than σ^- at K': this is understandable since the K valley bright exciton has lower energy at positive magnetic fields. For XD and TD in Figure 0.11c&d, we also observe that the σ^+

emissions have lower energy than the σ^-, confirming again the origin of the radiatively recombined electron and hole. What the unusual is their intensities: the lower energy σ^+ emission for XD and TD are significantly weaker than the higher energy σ^- emission. This somewhat counter-intuitive observation is a manifestation that XD and TD are intervalley complexes, as we discuss below.

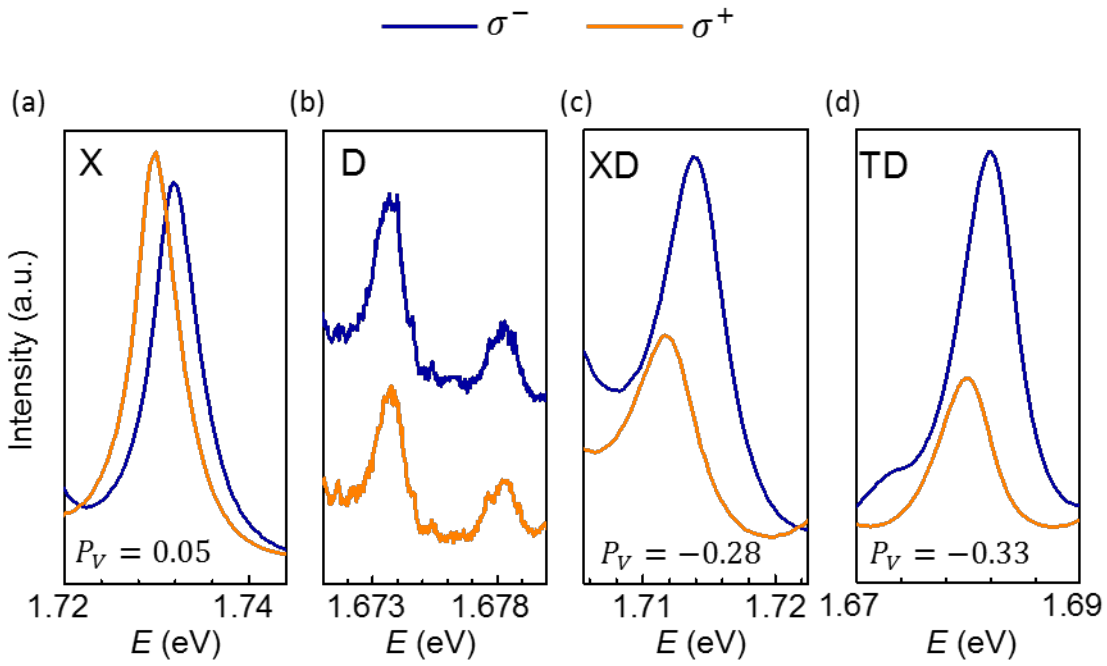

Figure 0.11: The luminescence spectra of X, D, XD and TD emission features in σ^+ and σ^- helicity at 8 T. Valley polarization is defined as $P_V = (I^{\sigma^+} - I^{\sigma^-})/(I^{\sigma^+} + I^{\sigma^-})$.

Following the convention established by previous studies [11,12,115], we quantify the valley polarization by:

$$P_V = \frac{I^{\sigma^+} - I^{\sigma^-}}{I^{\sigma^+} + I^{\sigma^-}} \qquad \text{(Eq. 6.2)},$$

where the I^{σ^+} and I^{σ^-} are the integrated emission intensity from the σ^+ and σ^- channels respectively. Using Eq.(6.2), we find P_V to be 0.05 for X, -0.28 for XD and -0.33 for TD. The negative P_V indicates that the dark excitons involved in XD and TD reside in the opposite valley from that of X and T; see the schematic illustrations in Figure 0.2. In the presence of a magnetic field, there exist lower Zeeman D excitons, which due to the intervalley nature of XD and TD, necessarily bind to the higher Zeeman X and T. As we discussed above, the radiation process of XD and TD involves the disassociation of the D exciton, and the X and T left behind then radiatively recombine. Hence the higher energy XD and TD emissions are more intense.

We note that using Eq. 6.2 for the dark exciton in Figure 0.11b, one would obtain a zero P_V, reflecting that in the absence of valley-helicity locking [10]. Nevertheless, the different intensities of the lower energy and higher energy Zeeman peaks I^L and I^H by summing up the σ^+ and σ^- contributions, still reflect the population difference of the Zeeman split dark excitons, and as expected I^L is larger than I^H, similar to the bright exciton X. If we define the dark exciton valley polarization as $P_V' = \frac{I^L - I^H}{I^L + I^H}$, we find P_V' to be 0.5. This value is much larger than the 0.05 P_V for X, due to the larger Zeeman splitting of D, as well as the absence of Maialle-Silva-Sham intervalley exchange interaction [129] that has been shown to cause valley depolarization of X [31]. It is also interesting to note that P_V' is larger, but reasonably close to the absolute value of P_V for

XD and TD. This provides yet another evidence that D is involved in XD and TD that we observe, and its valley distribution plays a dominant role in the large valley polarization of the four- and five-particle states, as compared to the bright excitons.

6.8 Summary

In summary, we observed six intrinsic low-energy emission features arising from bound quantum states in 1L-WSe_2. The presence of strong Coulomb interaction and the high quality of our sample enabled observation of the four-particle XD and five-particle TD bound states under a non-resonant continuous wave excitation. We assign XD as the intervalley biexciton composed of a spin-1 dark exciton and a spin-0 bright exciton, and TD as the intervalley exciton-trion consisting a spin-1 dark exciton and a negatively charged trion. These assignments may also impact the current understanding of biexciton and exciton-trion complexes in similar systems such as MoS_2, $MoSe_2$, and WS_2 in which the assignment of nonlinear optical features [26,130–132] is also being debated. Luminescence measurements at finite magnetic fields reveal the unusual negative valley polarization for the XD and TD emission, highlighting the role of dark excitons in forming the multi-particle bound states and their intervalley nature. Our results reveal rich many-body correlated excitonic physics and pave way to novel applications such as those involving valley encoded quantum information.

CHAPTER 7

LUMINESCENT EMISSION FROM RYDBERG EXCITONS OF 1L-WSE_2 IN HIGH MAGNETIC FIELDS

7.1 Introduction and Motivation

Exciton, one of the fundamental excitation in the solids, is composed by an electron and a hole bound by Coulomb attraction. Excitons in the solid-state materials can interact with lattices as well as other quasiparticles, providing an informative tool to study the material properties and the many-body interactions. For example, ground-state 1*s* exciton in 1L-TMDCs can be viewed, from many perspectives, as a benchmark for optical features of these atomic layers. It has a size and binding energy in-between the Wannier-Mott and Frenkel types of excitons because of the anisotropic dielectric screening. In addition, exciton-polariton and the interlayer exciton are extensively studied to demonstrate the Bose-Einstein condensation of exciton or biexciton.

In Chapter 6, we have shown the observation of the multi-particle bound states for the 2D excitons at lower energies. However, the relatively large 1*s* exciton binding energy opens a decent energy window of a few hundred meV below the free particle bandgap for studying excited exciton states. Analogue of hydrogen atom, exciton has several quantized excited states encoded by the principal quantum number (n), angular momentum quantum number (l), and magnetic quantum number (m). The highly-excited Rydberg states can be extensively populated up to few μm in space and thus can have longer radiative lifetime due to the wide separation of electron and hole

wavefunctions [133]. Studying excited states of Rydberg exciton have its fundamentally interests, such as the size dependence of the Coulomb exchange interaction [31] and Coulomb blockade effect between excitons with different energy states which has been investigated in conventional 3D semiconductors [133–135].

Previous studies have demonstrated using the detection of energy separation of Rydberg states to estimate the binding energy by differential reflectance (DR), second harmonic generations (SHG) and photoluminescence excitation (PLE) [17–19]. However, due to the sample variation and the uncertainty of measurements, the peak assignments are still under debates, resulting in the ambiguous estimation of binding energy. In this chapter, we demonstrate for the first time the observation of luminescent emission up to 4*s* excited states of the Rydberg excitons in the high quality hBN sandwiched 1L-WSe_2 sample. By measuring the diamagnetic shift, we confirm the assignment of Rydberg excitons at different principle quantum numbers up to 4*s* exciton. This also enables us to estimate the 1*s* exciton binding energy is about 170 meV, which is significantly smaller than most previous studies. In addition, the Zeeman splitting of the 1*s* to 3*s* states exhibits a monotonic increase of *g*-factor, reflecting nontrivial magnetic-dipole-moment differences between ground and excited excitons. We interpret this observation as a result of the joint action of the different spreading of the exciton states in the momentum space and the *k*-dependent magnetic dipole moment.

7.2 Magneto-optical Measurements on the Rydberg Excitons in 1L-WSe_2

Photoluminescence (PL) spectroscopy is a popular technique that has been widely employed to study the excitonic physics in H-TMDCs. While it is straightforward to observe the 1s exciton emission from TMDC monolayers, radiative emission from excited Rydberg states such as the 2s exciton is relatively challenging due to Kesha's rule: photon emission quantum yield is appreciable only for the lowest energy excited state, which for the charge neutral exciton, is the 1s exciton. In literatures, Rydberg excitons of 2D-TMDCs have been studied in high magnetic fields before, using both differential reflectance (DR, $\Delta R/R$) and magneto-PL spectroscopy [136–139]. These two techniques have different advantages and disadvantages. In reflectance/absorption spectroscopy, by performing high-order derivatives on heavily averaged and smoothed spectra, originally small and subtle features can be brought visible, and excited Rydberg states have been revealed this way even at zero magnetic field and room temperature [18,140]. On the other hand, due to the multi-layer structure (e.g. SiO_2 and hBNs) that causes multiple reflections and interference, the spectra are typically distorted and have large sloping background, making accurate determination of Rydberg state energy challenging. The PL typically gives much better-defined emission peaks that make the peak energies straightforward to determine. However, due to Kesha's rule, radiative emission from excited excitons is difficult to observe, as a result of their lower population density and smaller radiation dipole moment, as well as the strong competition from other intrinsic and extrinsic decay channels. Another disadvantage of PL spectroscopy is the typical existence of a Stokes shift between PL and absorption due to disorder [141]. This is especially important in the context of our investigation of Zeeman and diamagnetic shifts

here, as the unknown magnetic field dependent Stokes shift may complicate the interpretation of data. These disadvantages of PL spectroscopy are alleviated in our hBN-sandwiched 1L-WSe_2 sample due to the superior sample quality.

To ensure the reliability of our measurement and analysis, we performed both PL and DR measurements at NHMFL with a cryostat designed for free space light coupling integrated with a 17 T superconducting magnet (See Figure 0.10 for the setup). In Figure 0.1, we plot the PL spectra along with the DR spectra as well as its 2nd derivative (2DDR) at 5 K and 17 T. For 1*s* exciton, the strong signal enables us to determine the peak energy by all three methods unambiguously. The energy obtained using the three different methods are consistent, indicating *near-zero* Stokes shift. For excited Rydberg states, we can see 2*s* and 3*s* exciton peaks clearly in the PL spectrum. The DR spectrum also shows the 2*s* and 3*s* absorption dips quite clearly. However, there is a large sloping background and the significant distortion due to the interference effects induced by the multiple dielectric layers in our hBN/1L-WSe_2/hBN sample on an SiO_2/Si chip make assignment of the absolute peak position less accurate. The sloping background can be removed by performing the 2nd derivative of the $\Delta R/R$ spectra (2DDR), and we can extract the peak energy by fitting the dominant peak with Gaussian functions; see Figure 0.1. Note that in the 2DDR spectra, several sharp and tiny artifacts show up in the 3*s* energy range (presumably coming from either the optics or light sources; we tried both supercontinuum laser and halogen lamp) and cannot be averaged out. The amplitude of these features is about 0.2%, making the accurate extraction of 3*s* and 4*s* dip positions challenging. We thus focus on the 2*s* exciton to compare the magnetic shifts measured by PL and DR methods.

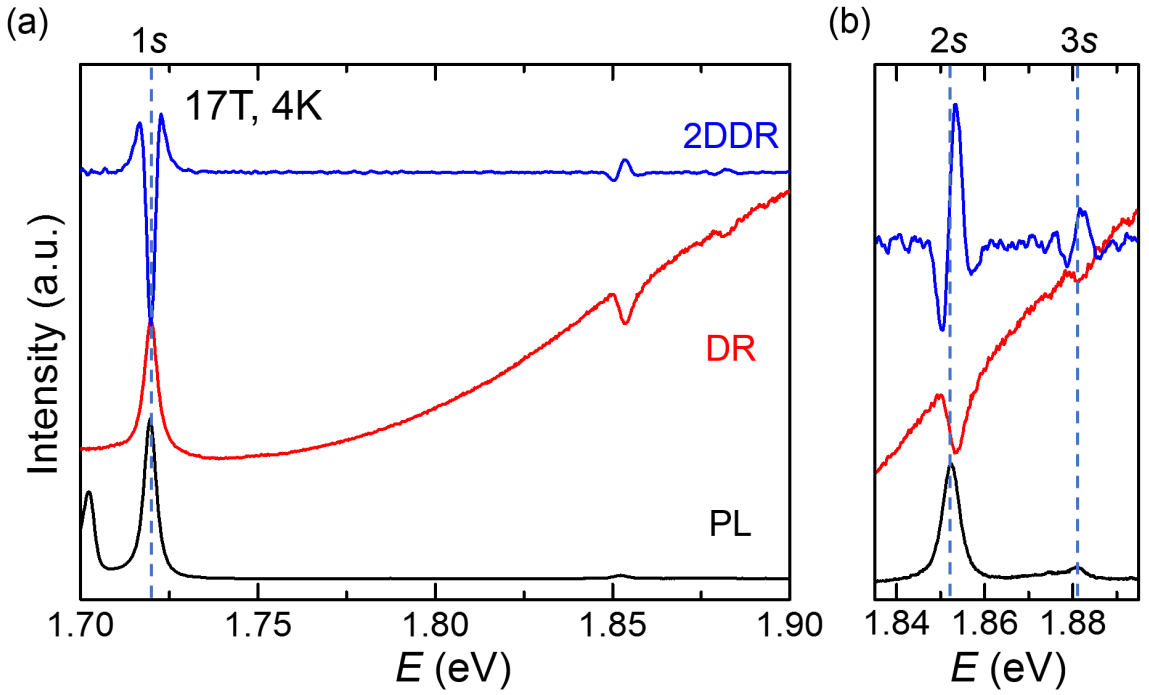

Figure 0.1: (a) The comparison of the PL, differential reflectance (DR) and the 2nd derivative differential reflectance (2DDR) spectra at 17 T. The dashed lines indicate the peak energy extracted from PL spectra. (b) The zoom-in spectra for 2*s* and 3*s* excitons.

Although the spectral distortion results in a sizable artificial blue shift in the 2*s* DR and 2DDR spectra as demonstrated in Figure 0.1b, the extraction of magnetic shifts are still quite reliable. The 17 T system allows us to measure both σ^- and σ^+ helicity photons at the same magnetic field. We extract the Zeeman-split 2*s* exciton energies and calculate their difference ΔE and average E_{avg}, which are the quantity related to the Zeeman and diamagnetic shifts respectively (see Eq. (7.1) below). Figure 0.2a & b compare the results extracted from PL and 2DDR. We observe that, aside from the artificial overall blue shift due to distortion effect in DR spectra, the results are quite consistent in both Zeeman and diamagnetic shift analysis. In Figure 0.2a, the two data sets overlap well and give the same slope with an uncertainty less than 2%. Figure 0.2b, both data set can be well fitted by the same quadratic curves with uncertainty of about ~ 4% in the quadratic coefficient (the two fits in Figure 0.2b used the same quadratic coefficient). Given that the analysis of PL and reflection measurement is consistent, we focus below on the magneto-PL data which are measured up to 31 Tesla, and enables more reliable determination of the energy of Rydberg excitons.

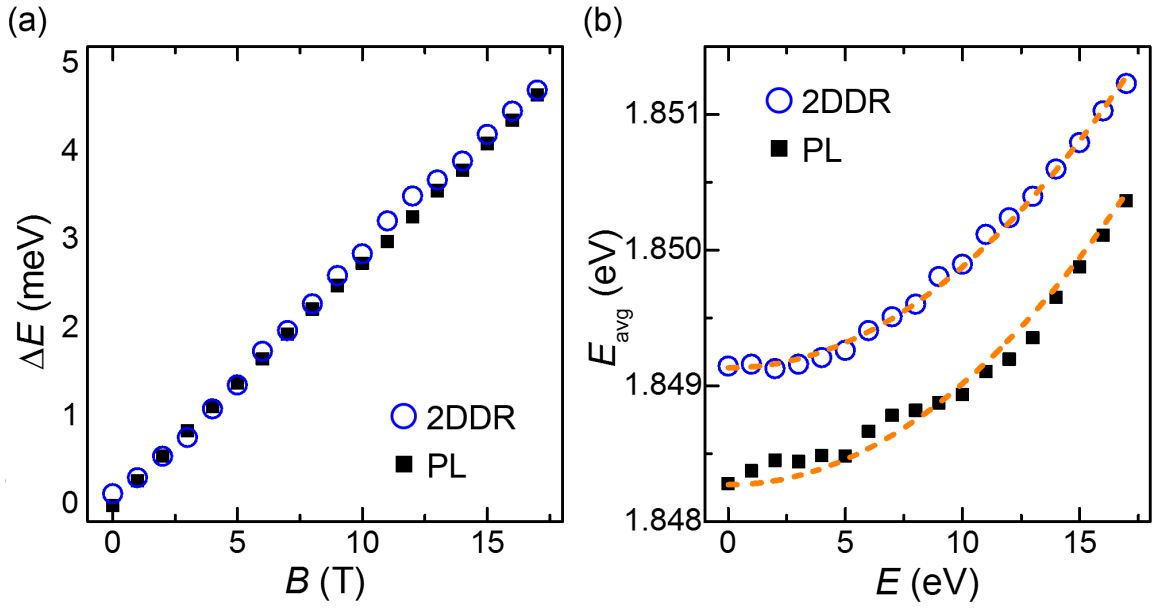

Figure 0.2: (a) The magnetic field dependent energy difference of 2*s* exciton of σ^- and σ^+ signals extracted by PL and 2DDR spectra. (b) The magnetic field dependent average energy of 2*s* exciton of σ^- and σ^+ signals extracted by PL and 2DDR spectra.

7.3 Diamagnetic Shift of the Rydberg Excitons in High Magnetic Fields

With the confidence of our data analysis, we can analyze the data quantitatively for the Rydberg excitons. At our maximum field of 31 T, the cyclotron energy $\hbar\omega_c \approx \hbar eB/m_e$ of the electrons is given by 7.2 meV. This is much smaller than the binding energy of the exciton, which is about 170 meV for 1*s* exciton. In this weak field limit, the magnetic field dependence of exciton energy can be described by

$$E(B) = E_0 - (\mu_{c1} - \mu_{v1})B + \frac{e^2}{8m_r}\langle r^2\rangle B^2, \qquad \text{Eq. (7.1)}$$

where E_0 is the exciton energy at zero field; μ_{c1} and μ_{v1} are the total magnetic moments of the lowest conduction and top valence electron states respectively; $m_r = \frac{m_e^* m_h^*}{m_e^* + m_h^*}$ is the reduced mass of the exciton; $\langle r^2\rangle = \langle\Psi|r^2|\Psi\rangle$ is the expectation value calculated over the exciton's wavefunction which provides a measurement of the exciton size. The first term is called Zeeman shift which is linear in *B* and the second term is the diamagnetic shift which is quadratic. We thus can separately extract the two contributions from the exciton energy vs. magnetic field plot by calculating the difference and average energies of PL of opposite helicity in the same field (see Figure 0.2) or PL of same helicity under opposite magnetic field.

Figure 0.3 displays the 2D map of PL intensity as a function of magnetic field *B* ranging from -31 to 31 T. The intense peak shown in the left subpanel at about 1.73 eV is the 1*s* exciton, whose peak position evolution is dominated by the Zeeman shift; the peak energy shifts linearly with B field. In the higher energy region from 1.85 to 1.95 eV, at low fields, we observed a well-defined peak at 1.86 eV and a broad feature centered around 1.88 eV. The peak at 1.86 eV has been assigned as the PL from 2*s* exciton [31];

here its prominent deviation from the linear Zeeman shift as compared to the 1*s* exciton indicates the sizable contribution from the quadratic term, providing a smoking-gun evidence that it has larger diameter than 1*s*. The ~1.88 eV broad feature has been attributed as the 3*s* exciton before [142]. From Figure 0.3, this feature becomes better defined at high fields, and its energy versus *B* is even more curved than 2*s*. This suggests that at low fields only part of the spectral weight of the broad feature is due to the 3*s* exciton, while at high fields 3*s* dominates the spectra. The strong magnetic fields are indeed helpful for resolving the excited Rydberg excitons. As seen in the spectra at −31T in Figure 0.3, we observe a well-defined peak attributable to the 4*s* exciton at around 1.925 eV, in accordance with its even larger curvature vs. *B* (dashed white curve).

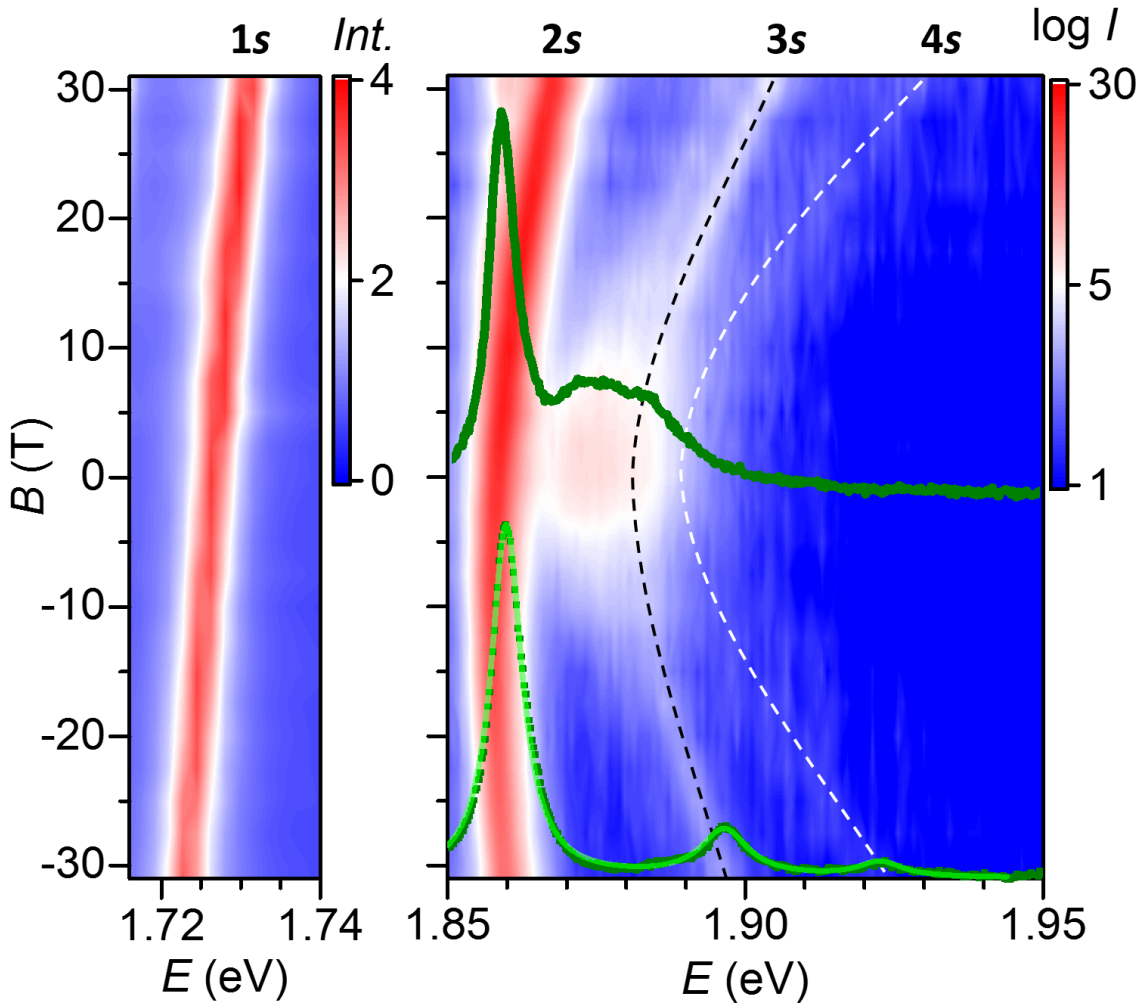

Figure 0.3: The 2D contour plot of PL spectra as a function of magnetic field from −31 to 31 Tesla. The 1*s*, 2*s*, 3*s* and 4*s* excitons are denoted on the top of the panel. The black and white dashed curves on 3*s* and 4*s* excitons are guided by eye. We also include the spectra taken on 0 T and −31 T on the right panel.

7.3 Diamagnetic Shift of the Rydberg Excitons in High Magnetic Fields

In Figure 0.4a we have plotted the average energy of the σ^- PL emission at positive and negative fields as a function of B^2. Defining $E_{dia} = \alpha B^2 = \frac{e^2}{8m_r}\langle r^2\rangle B^2$, we find α to be 0.5, 5.8, and 17.6 $\mu\text{eV}/T^2$ for 1s to 3s excitons, which provide quantitative measurement of the size-mass ratio for these Rydberg exciton species. By extrapolating the diamagnetic shifts to zero field as shown in Figure 0.4, we find E_0 to be 1.727(1), 1.858(1), 1.884(1) eV for 1s to 3s exciton, respectively, evidently showing that the binding energy of 1s exciton is at least larger than 157 meV. Our data can be well fitted by the theoretical model by assuming a quasi-particle gap of 1.9 eV and a reduced mass of $0.22m_0$, where m_0 is the bare electron mass. As demonstrated in Figure 0.4b, we find that the calculated exciton energy: 1s, 1.731 eV; 2s, 1.859 eV; and 3s, 1.882 eV, in reasonable agreement with experimental data. This also suggests that the binding energy of ground state exciton can be estimated around 170 meV. This binding energy is close to a recent DR measurement at high magnetic fields [143], but is significantly smaller than previous zero field DR results [18], which might be due to the different dielectric environment.

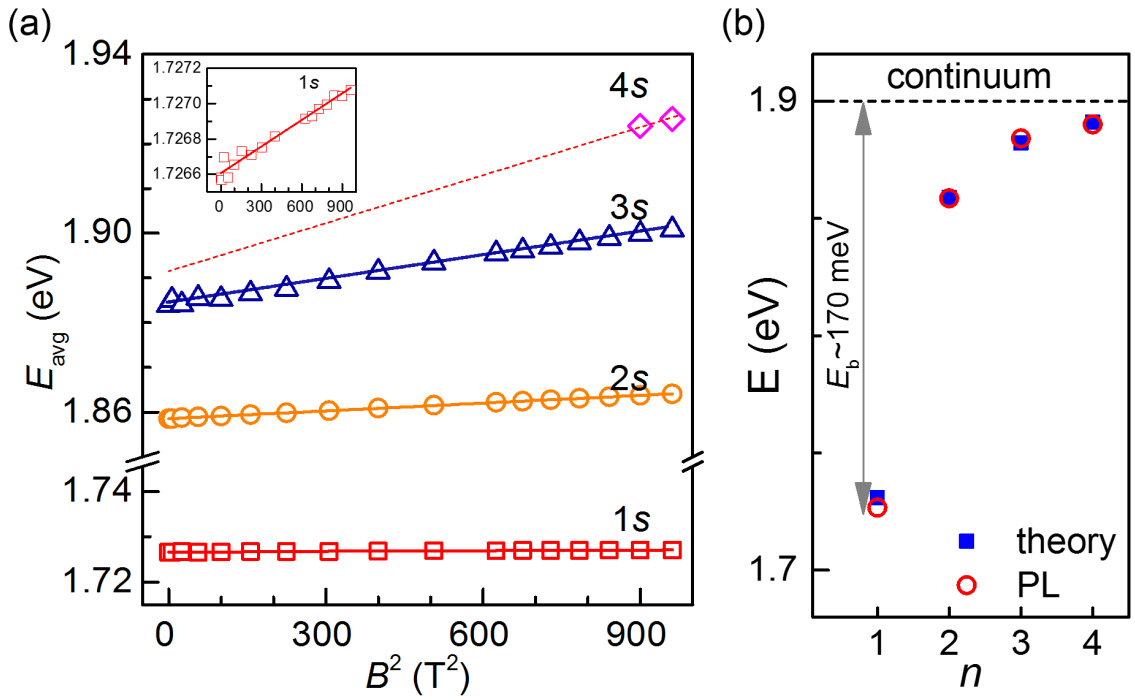

Figure 0.4: (a) The extracted energy of Rydberg excitons plotted as a function of B^2. (b) The theoretical and experimentally extrapolated energies of Rydberg excitons at $B = 0$ T

7.4 Reduced Mass and Radius of Rydberg Excitons in 1L-WSe_2

The quantity α extracted in Figure 0.4a only fix the relation of the reduced mass m_r and radius for different excited states. In our experiment, we did not directly measure the exciton reduced mass. In literature, the effective mass measurements on 1L-WSe_2 have been demonstrated by several different techniques while the results are still in debate. Magneto-transport measurements have been demonstrated on high quality hBN-sandwiched 1L-WSe_2 [144,145]. By fitting the cyclotron frequency extracted from Shubnikov-de Hass oscillations, the effective mass of hole has been estimated as $m_h = 0.45$ to $0.5\, m_0$, which is consistent with the value reported in *ab-initio* calculation [21,128]. In addition, a recent magneto-optical measurement probes the inter-Landau level transition in K/K' valley separately by the helicity-resolved reflection spectroscopy [146]. The reduce effective mass of exciton can thus be estimated from $m_r = 0.27$ to $0.31 m_0$; the variation comes from the screening effect of Coulomb interaction driven mass normalization. Above discussion implies that the effective mass may have strong sample to sample variation and sensitive to the dielectric environments. By assuming the $m_e \sim m_h$ (the measurement on m_e is still lacking), we can summarize the m_r is ranging from 0.22 to $0.31 m_0$ based on literatures. Using the same reduced mass in the fittings of Rydberg exciton spectra, $m_r = 0.22\, m_0$, we thus can determine the radii of exciton as 2.1, 7.2 and 12.6 nm for 1*s*, 2*s*, and 3*s* exciton, respectively.

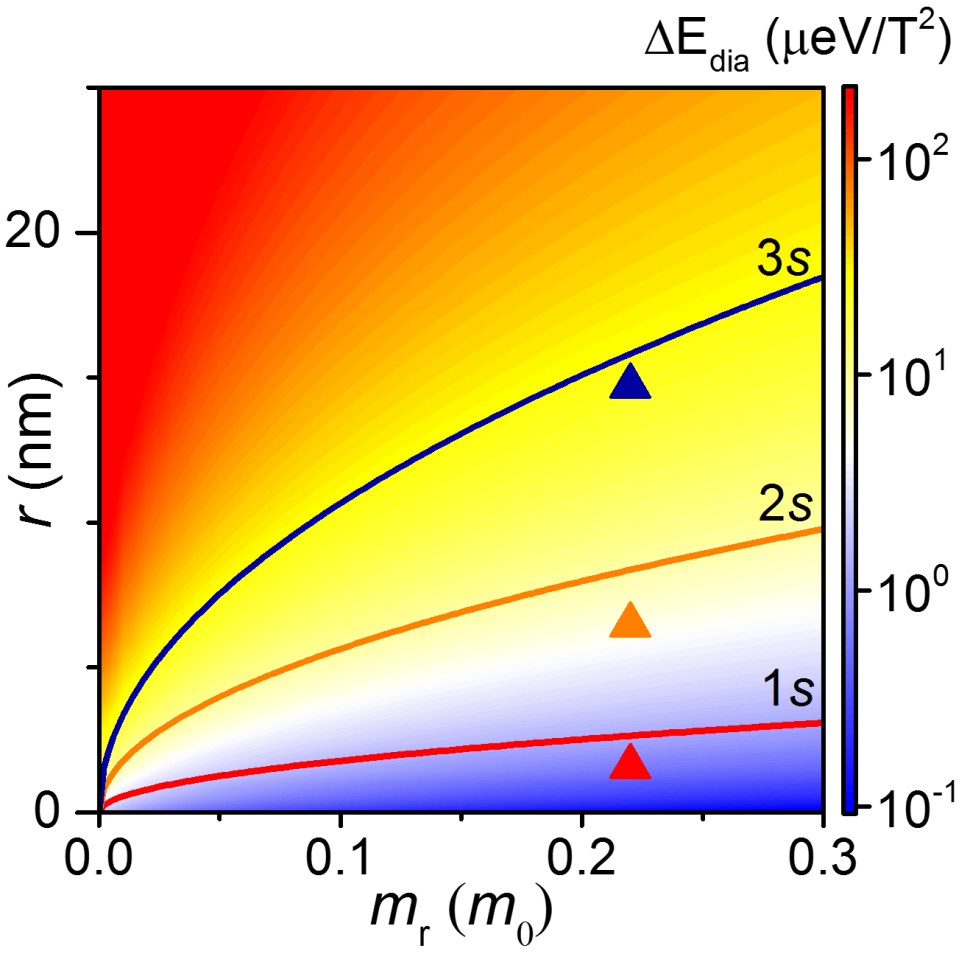

Figure 0.5: The contour plot showing the relation of reduce mass and radius and the corresponding α (in log scale). The triangular dots indicate the calculated radii of 1s to 3s exciton by using $m_r = 0.22\ m_0$.

Although the energy is quite consistent with our theoretical model, we cannot perfectly match our experimental data of diamagnetic shift with under the same theoretical framework. In Figure 0.5, the solid curves on the color map describing the relation of reduce mass and radius for 1s to 3s excitons with the corresponding α we acquired experimentally; the magnitude of α is encoded in colors. In the same plot, we also include few data points by applying m_r as 0.22 m_0 and calculating the radius of the 1s to 3s Rydberg excitons. As can be seen, the theoretical value in general underestimate the radius size comparing with the experimental results. This could be explained by the wave function we used in our model is approximated by the 2D hydrogenic wave functions. It is expected that to be improved if the proper exciton wave functions, obtained by numerical diagonalization of the Hamiltonian are used instead.

7.5 Size Dependent Magnetic Dipole Moment of Rydberg Excitons

We now discuss the Zeeman shift of the different Rydberg excitons, which is obtained by subtracting the peak energies at positive and negative magnetic fields to eliminate the contribution from the diamagnetic shift: $\Delta E_Z = \frac{E(B)-E(-B)}{2} = g\mu_B B$, where μ_B is Bohr magneton and g is the normalized factor to quantify the exciton magnetic dipole moment. Figure 3d displays ΔE_Z as a function of magnetic field for σ^- emission which is linked to excitons in the K' valley. As expected, the energy shift is linearly proportional to the magnetic field. Interestingly, we observe that the magnitude of g-factor monotonically increases from 2.15 for 1s exciton to 2.53 for 3s exciton. This systematic increase of g-factor for larger excitons is real, and it indicates nontrivial difference of the total magnetic moments in different Rydberg states.

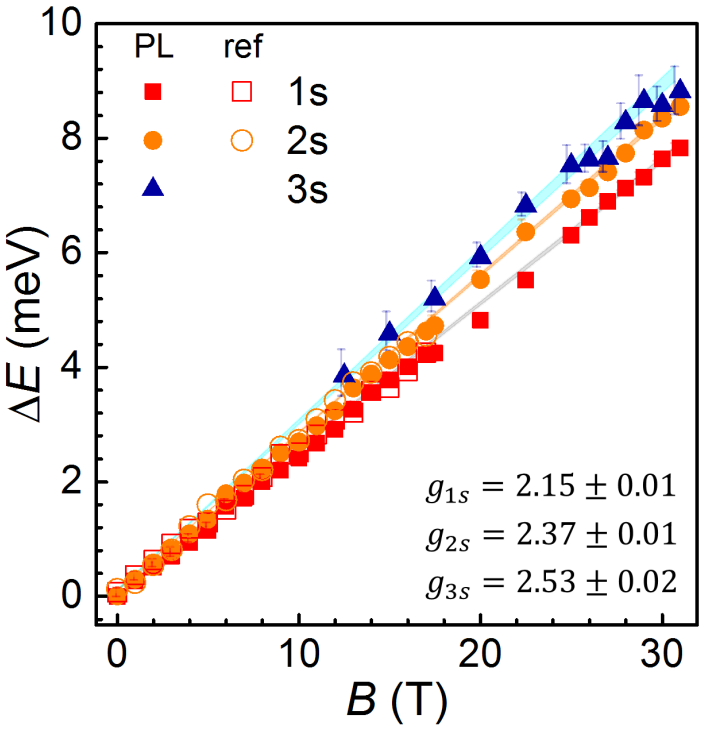

Figure 0.6: Zeeman shift of Rydberg excitons extracted by different measurement method. The *g*-factors are extracted by linear fitting of the slope.

As has been discussed in several previous studies as well as in Chapter 6.6, the magnetic moment of the exciton in 1L-WSe_2 is composed of three components originating from the spin, the atomic orbital, and the valley: $\mu_{total} = \mu_s + \mu_o + \mu_v$, where $\mu_s = 2s\mu_B$, $\mu_o = m\tau\mu_B$; $\mu_v = \beta\tau\mu_B$; s, m and τ are quantum number of spin ($s = \pm 1$, for spin up/down), orbital (m is determined by the angular momentum of the atomic orbitals) and valley ($\tau = \pm 1$ for K or K' valley), respectively; β is the orbital contribution calculated from Barry curvature. We calculate the contribution of the three parts separately in the K' valley (K valley is the time-reversal pair), corresponding to the σ^- emission in our data. For bright excitons, the spin term is contributed nothing due to spins for electron and hole are aligned. The total orbital terms sum up the contribution

from lowest conduction band (c1) and top valence band(v1), which give the contribution about $2\mu_B$ in K' valley.

The first principle calculation [128] reveals that in 1L-WSe_2, c1 band is dominant by d_{z^2} $(m = 0)$ orbital while the v1 band is dominant by $d_{x^2-y^2} + d_{xy}$ $(m = 2)$ The net contribution induced by orbital magnetic moments in K' valley is $2\mu_B$. The magnetic moments contributed by the valley term are originated from the Barry curvature induced the self-rotation of electron wavepacket. In our data, the magnitude of g-factor for 1s to 3s excitons is larger than $2\mu_B$, indicating the finite contribution from the valley terms: $\mu_v = \mu_{v,c1} - \mu_{v,v1}$. In contrast to the spin and orbital terms, we note that the Barry curvature is peaked at the band edge of K/K' point and is changing sharply with the finite k distribution. As a result, the magnitude of μ_v should be sensitive to the wavefunction extension in k-space for different Rydberg states, contributing a nontrivial difference in Zeeman terms. Because of its tightly bound nature of 1s exciton in 1L-WSe_2, we anticipated that the μ_v contribution of 1s exciton will be quite deviated from others.

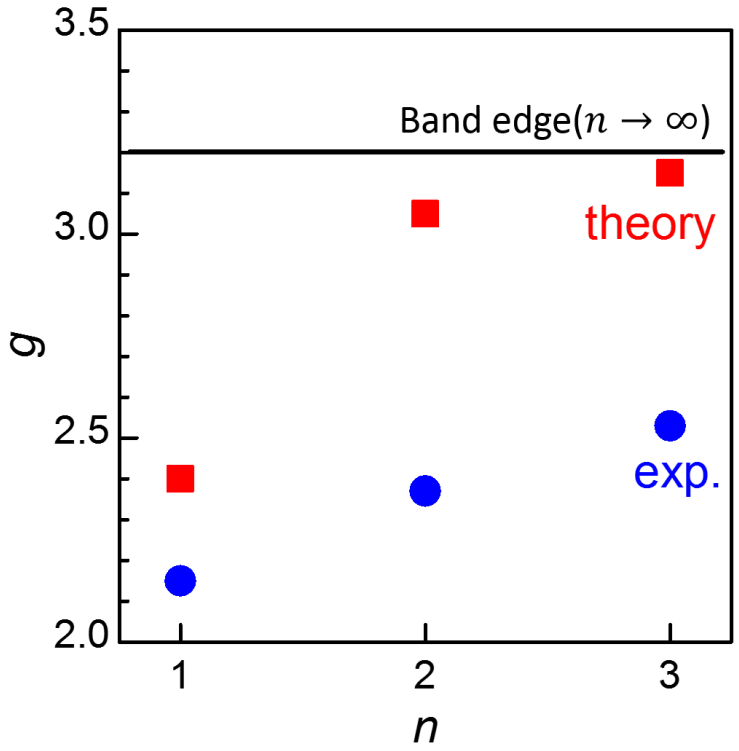

Figure 0.7: Comparison of experimental and theoretically derived the g-factors of 1*s* to 3*s* exciton.

To figure out the impact of the finite-k distribution on the magnetic dipole moments, we perform the DFT calculation by applying the 2D hydrogenic wave functions and the interaction potential with Rytova-Keldysh form. The results are summarized by the red square dots in Figure 0.7. Right on the band edge, the μ_v is calculated about $1.2\mu_B$, yielding the μ_{total} is $3.2\mu_B$ in K' valley (the black line in Figure 0.7). Considering the finite spreading in k-space, the calculated μ_{total} for 1*s* is significantly smaller about $2.4\mu_B$, denoted as the dashed lines in Fig.3d. For 2*s* and 3*s* exciton, the total magnetic moment is approaching $3.2\mu_B$, yielding $3.05\mu_B$ and $3.15\mu_B$, respectively. Qualitatively, the trend derived theoretically matches the experimental data well, reflecting the k–dependent μ_v does participate in the total magnetic dipole moments.

However, quantitatively, the magnitude is consistently larger and the discrepancy is dependent by *n* quantum numbers. We suggest that there are other sources participate in addition to the Barry curvature. A recent paper reveals that the strong Coulomb interaction as well as exchange interaction can induce an abnormal behavior of *g*-factor for exciton in 1L-WSe_2 in high electron-doped region [147]. In addition, in our previous work, we indicated that the 2*s* exciton exhibits superior valley polarization and coherence which is origin from the suppression of the Coulomb-exchange-interaction-driven valley-depolarization process, the Maialle-Silva-Sham (MSS) mechanism [31] which is dramatically distinct from 1*s* to 3*s* exciton. The discrepancy between in the theoretical calculation and experimental data could be partially explained by the participation of exchange interaction which is not negligible when considering the tightly bound exciton.

7.6 Summary

In conclusion, we demonstrate in the first time the observation of PL of Rydberg exciton up to 4*s*. Due to the superior sample quality and high magnetic fields, we are able to accurately determine the Zeeman shift and diamagnetic shift of different Rydberg excitons, enabling us to unambiguously assign the PL emission features. In addition, we systematically investigate the physical properties of these Rydberg excitons. The diamagnetic shift increase monotonically with higher excited states, reflecting the larger size of higher Rydberg states. We also observe the magnetic dipole moment is sensitive to the *n* quantum numbers. The trend qualitatively matches our theoretical calculation. However, more theoretical work is required to explain the discrepancy quantitatively.

CHAPTER 8

SUPERIOR VALLEY POLARIZATION OF 2*S* RYDBERG EXCITON

8.1 Research Objective and Motivation

The coupled spin-valley physics [10] in 1L-TMDC semiconductors has inspired great strides towards realizing valleytronic devices harnessing these 2D materials [11–13,115]. As extensively discussed in Chapter 6, the two energetically degenerate 1L-TMDC valleys with opposite angular momentum can be selectively populated with circularly polarized optical excitation, and the valley polarization can be detected both optically [11,12,115] as well as electrically [13]. The two degenerate valleys can be lifted by applying a finite perpendicular magnetic field, as demonstrated in Chapter 6 and 7. Further, coherent superposition of valley excitons can be generated with linearly polarized light [114] or a sequence of laser pulses with opposite circular polarization [123], which allows for rotation of the valley pseudospin with magnetic Zeeman effect or optical Stark effect [148,149]. Such coherent manipulations of valley pseudospin are at the heart of future quantum valleytronic devices, and require thorough understanding and efficient control of various valley depolarization and decoherence processes. Intervalley scattering, the one of the core issues in the valleytronic studies, which directly related the valley polarization and dephasing of the quantum states, similar to spin relaxation issues in spintronic. In general, intervalley scattering can occur due to both extrinsic mechanisms such as disorder scattering, and intrinsic mechanisms such as the Coulomb exchange interaction [129]; the competition between these different valley relaxation channels is a topic under active debate [123,150–152].

So far many of the valleytronic studies focus on the 1*s* bright exciton (X in chapter 6) and the low energy bound states (e.g. T_1 and T_2), which is readily accessible in 2D TMDC monolayers [11–13,114,115,123,148,149,153]. In this chapter, we study the valleytronic properties of the Rydberg states, the 2*s* exciton. Even though the PL emission of 2*s* is not energetic favorable due to the Kasha's rule, the 2*s* exciton luminescence in our high quality 1L-WSe_2 can be clearly observed and is persisted up to room temperatures, providing a new quantum entity for facile manipulation of valley pseudospins. Most interestingly, we found that 2*s* exciton exhibits much higher degree of valley polarization and coherence in contrast to 1*s*, enabling the opportunity to use 2*s* exciton as the better valleytronic states.

8.2 Physical Properties of the Rydberg 2*s* Excitons Emission

We first explore the physical properties of 2*s* exciton by PL measurements. Figure 0.1a shows detailed temperature dependence of the exciton luminescence emission. X_{1s} peaks at about 1.65 eV at room temperature and blue shifts with a narrower linewidth at lower temperatures. Its intensity first increases and then decreases, peaking at about 150K as shown in Figure 0.1b. We note that this is distinct from WSe_2 samples that display monotonic 1*s* intensity decrease with lowering temperature, as a result of disorder scattering that depletes bright excitons into thermal equilibrium with lower energy dark excitons possessing opposite electron spin configuration [116]. In the temperature range $T > 150$ K, the increase of intensity is due to the reduction of phonon scattering at lower temperature. However, below 150 K, the dramatically decrease of intensity of 1*s* is because: First, the ground dark exciton states deplete the bright exciton. Second, several

multi-particle bound states are getting dominated due to the reduction of thermal activation energy. The non-monotonic 1*s* intensity temperature dependence is thus a manifestation of out-of-equilibrium exciton radiative recombination becoming more competitive with thermal equilibration between different quantum channels when disorder in the sample is minimized. In contrast, the intensity of 2*s* luminescence keeps increasing with lowering temperature. This indicates that removal of phonon scattering enhances non-equilibrium 2*s* radiative emission, and further suggests that the 2*s* exciton also has fast radiative recombination rate [154–156] as well as the limited competition with other states.

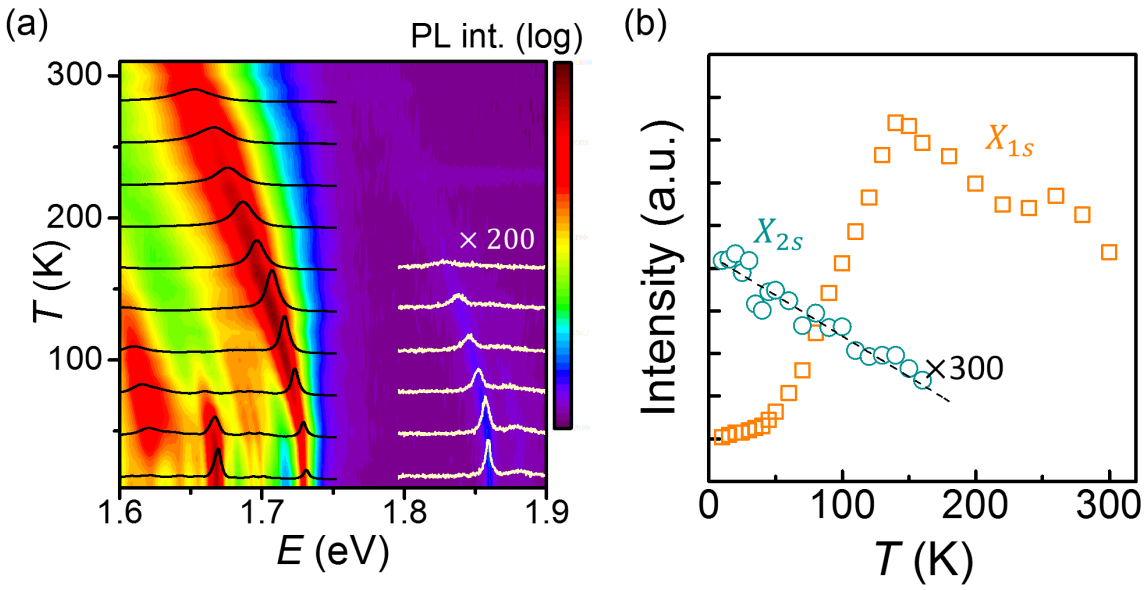

Figure 0.1: (a) Photoluminescence spectra plotted as a function of temperature. Selected spectra at *T* = 10 to 280 K with 30 K steps are displayed. (b) Temperature dependences of 1*s* and 2*s* intensity.

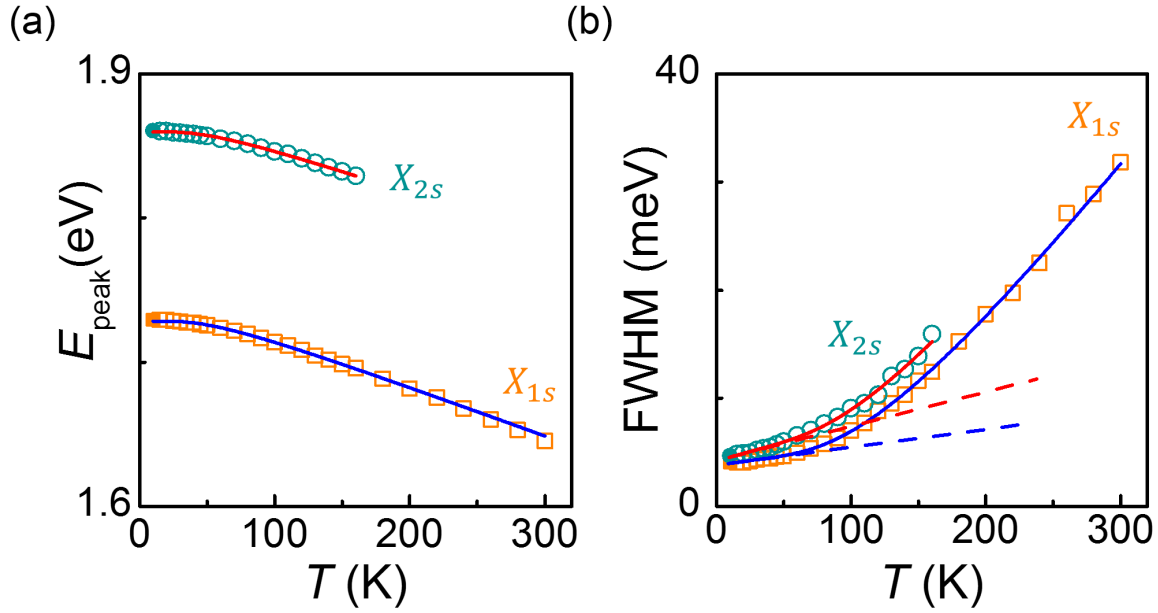

Figure 0.2: Temperature dependent (a) peak energy and (b) linewidth of X_{1s} and X_{2s} radiations. The solid curves are fits using Eq. 8.1 and 8.2. The dashed lines in (b) represent the linear terms which dominate at low temperatures.

The 1*s* and 2*s* peak energy and linewidth show similar temperature dependences. We found that they can be fitted to the same models of hyperbolic cotangent relation (Eq. 8.1) [157] and phonon induced broadening (Eq. 8.2) [158] respectively:

$$E_g(T) = E_0 - S\langle\hbar\omega\rangle\left[\coth\left(\frac{\langle\hbar\omega\rangle}{2k_BT}\right) - 1\right] \qquad \text{Eq. (8.1)},$$

where E_0 is the optical bandgap at T = 0 K, S is the coupling factor, and $\langle\hbar\omega\rangle$ represents the average phonon energy in the system [159];

$$\gamma = \gamma_0 + c_1T + \frac{c_2}{e^{\frac{\langle\hbar\omega\rangle}{k_BT}} - 1} \qquad \text{Eq. (8.2)},$$

where γ_0 is the FWHM at T = 0 K, the second and third terms account for the impacts of acoustic and optical phonons respectively, and $\langle\hbar\omega\rangle$ matches well with the OC and IMC phonons which are accidentally degenerate in 1L-WSe_2 [27]. From the fitting parameters in Table 8.1, γ_0 is 3.80 ± 0.05meV. This matches well with four-wave-mixing measurements [160] that reveals the intrinsic FWHM of 1L-WSe_2 to be 3.8 ± 0.4 meV at 5 K, indicating that disorder in our sample is indeed minimal.

Table 0.1: The fitting parameters for the temperature dependent peak energy and linewidth of 1*s* and 2*s* exciton luminescence.

	peak energy			linewidth			
	$\langle\hbar\omega\rangle$	E_0	S	$\langle\hbar\omega\rangle$	γ_0(FHWM)	c_1	c_2
	meV	eV		meV	meV	μeV/K	
X_{1s}	13.0 ± 0.4	1.728	2.01 ± 0.03	31 ± 1	3.80 ± 0.05	16.0 ± 1.4	0.05 ± 0.002
X_{2s}		1.860	1.85 ± 0.05		4.20 ± 0.06	34.0 ± 1.7	0.05 ± 0.004

Similar to the one we demonstrated with 1*s* exciton in Chapter 6.4, we also performed electrostatic doping dependent PL measurements using an hBN-sandwiched FET device to probe charge-doping dependence of the 2*s* exciton. Figure 0.3 shows the PL spectra as a function of gate voltage at 4 K. We found that the intensity of X_{1s} and X_{2s} are highly correlated: both peaks appear at charge neutral and become broader and slightly red shift at hole doping side, indicating that X_{1s} and X_{2s} are associated with neutral excitons. Interestingly, in contrast to 1*s* exciton which develops rich features in the low energy, the energy range in between 2*s* and 1*s* excitons is quite spectral clean, indicating 2s exciton has weaker Coulomb interaction. This result is consistent with the

larger radius of 2*s* exciton we measured in Chapter 7 and the monotonic temperature dependent intensity we just discussed.

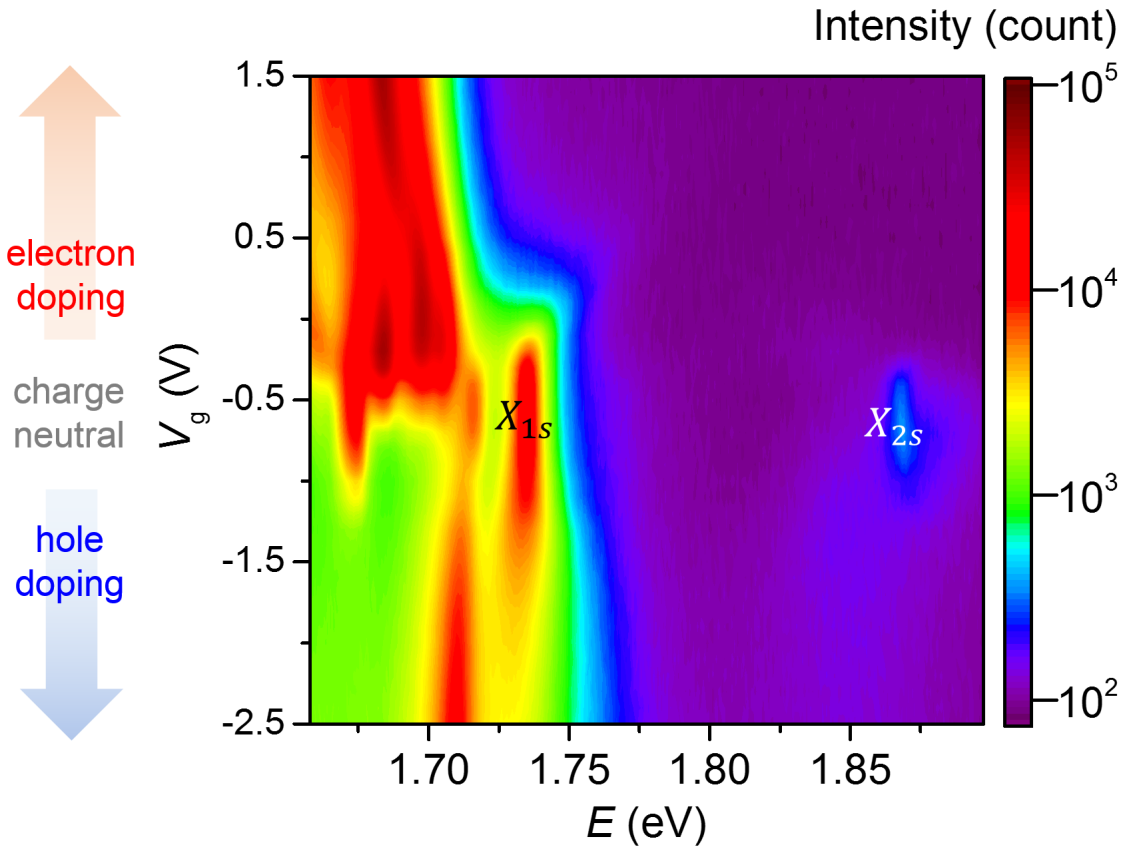

Figure 0.3: PL spectra plotted as a function of gate voltage for a hBN sandwiched 1L-WSe_2 FET device at 4 K with 1mW, 2.33 eV excitation.

8.3 Valley Polarization and Valley Coherence of Excitonic States in 1L-WSe_2

Taking advantage of the robust spin-valley locking and valley-helicity selection rule [10], we use circularly polarized light to selectively populate one valley and monitor the resultant valley polarization by examining the helicity of optical emission [11,12,115]. Using the similar definition employed in the spintronic, we define the valley polarization $P = \frac{I_{\sigma^+} - I_{\sigma^-}}{I_{\sigma^+} + I_{\sigma^-}}$: exciting the sample with σ^+ polarization light and collect the luminescence emission with σ^+ and σ^- separately. The $I_{\sigma^\pm}$ is defined as the radiation intensity for the helicity $\sigma^\pm$ for the corresponding modes.

We also use linearly polarized light to create a coherent superposition of excitons in both K and K' valleys; the decoherence of the valley excitons are reflected in the degree of linear polarization of the luminescence emission [114]. Experimentally we excite our sample with a horizontal (H) linearly polarized laser light and detect the luminescence emission with H and vertical (V) polarizations; see Figure 0.9a. We define $C = \frac{I_{\mathrm{HH}} - I_{\mathrm{HV}}}{I_{\mathrm{HH}} + I_{\mathrm{HV}}}$ to quantify the coherence of the superposition states, where I_{HH} and I_{HV} are defined as the radiation intensity for the H and V polarized light with the excitation of H polarized light.

We first demonstrate the *P* and *C* on the 1*s* exciton as well as the low energy bound states in Figure 0.4. The Figure 0.4a shows the cocircular ($\sigma^+\sigma^+$) and cross-circular ($\sigma^+\sigma^-$) polarization spectra taken at 4 K with excitation about 20 meV above 1*s* exciton. As can be seen, the bright exciton X is slightly valley polarized. Two trions exhibit distinct behaviors, T_1 is strong valley polarized while T_2 is none. These two observations reflect the existence of strong Coulomb exchange interaction with the bright

exciton, which is the core in this chapter. The XD and TD both show slightly valley polarization. The helicity-valley selection rule does not hold in dark exciton, which has been shown in Chapter 6. The valley polarization of XD and TD is thus determined to X and T_2 for XD and TD, respectively. Moreover, we observed a peak X' with the energy about 60 meV below the X also exhibits great valley polarization. The origin of X' is so far unclear and will be further investigated in Chapter 9.

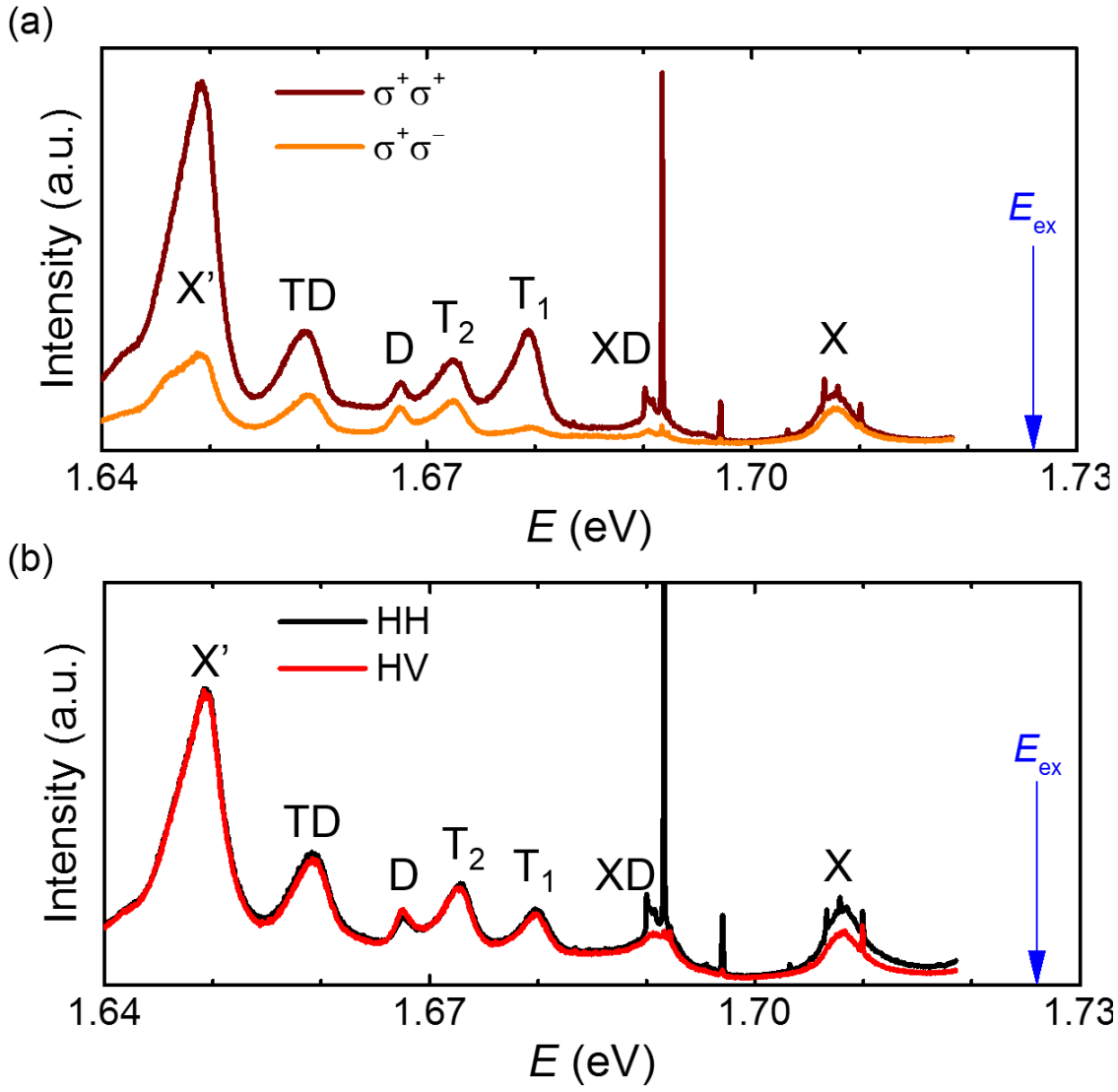

Figure 0.4: The circular and linear polarization-resolved photoluminescence of 1*s* exciton and its multi-particle bound states in 1L-WSe_2 at 4 K.

In Figure 0.4b we present the spectra from the same sample and sample temperature but replacing the circular polarized light with the linear polarized one. Interestingly, only X show slightly valley coherence. Other modes in general exhibit zero valley coherence. The loss of valley coherence can be attributed to the Coulomb exchange interactions which breaks the valley coherence [114]. Another possible explanation as we will discuss in Chapter 9, the radiative recombination lifetime of these lower energy states is much longer comparing with X [127], resulting in the competition with other dephasing mechanisms.

Now we turn to the *P* and *C* of 2*s* exciton state in the higher energy side. Previous studies had shown that the magnitude *P* and *C* in H-TMDC are sensitive to the temperature and the energy difference between excitation energy and the exciton emission energy [114,161]. We thus perform the measurement at same temperature and fix the excitation energy about 20 meV above the 1*s* and 2*s* exciton to compare difference of *P* and *C*. Interestingly, as demonstrated in Figure 0.5, we found the 2*s* exciton exhibits superior capability in retaining the broken time reversal symmetry and coherence of incident laser light with $P = 0.82$ and $C = 0.56$. However, for 1*s* exciton, $P = 0.15$ and $C = 0.17$ are significantly smaller than 2*s*. The high *P* and *C* in 2*s* exciton imply that the valley relaxation by defect scattering or other dephasing mechanism has less impact on 2*s* exciton, making the 2*s* exciton as a good quantum state for valleytronic applications.

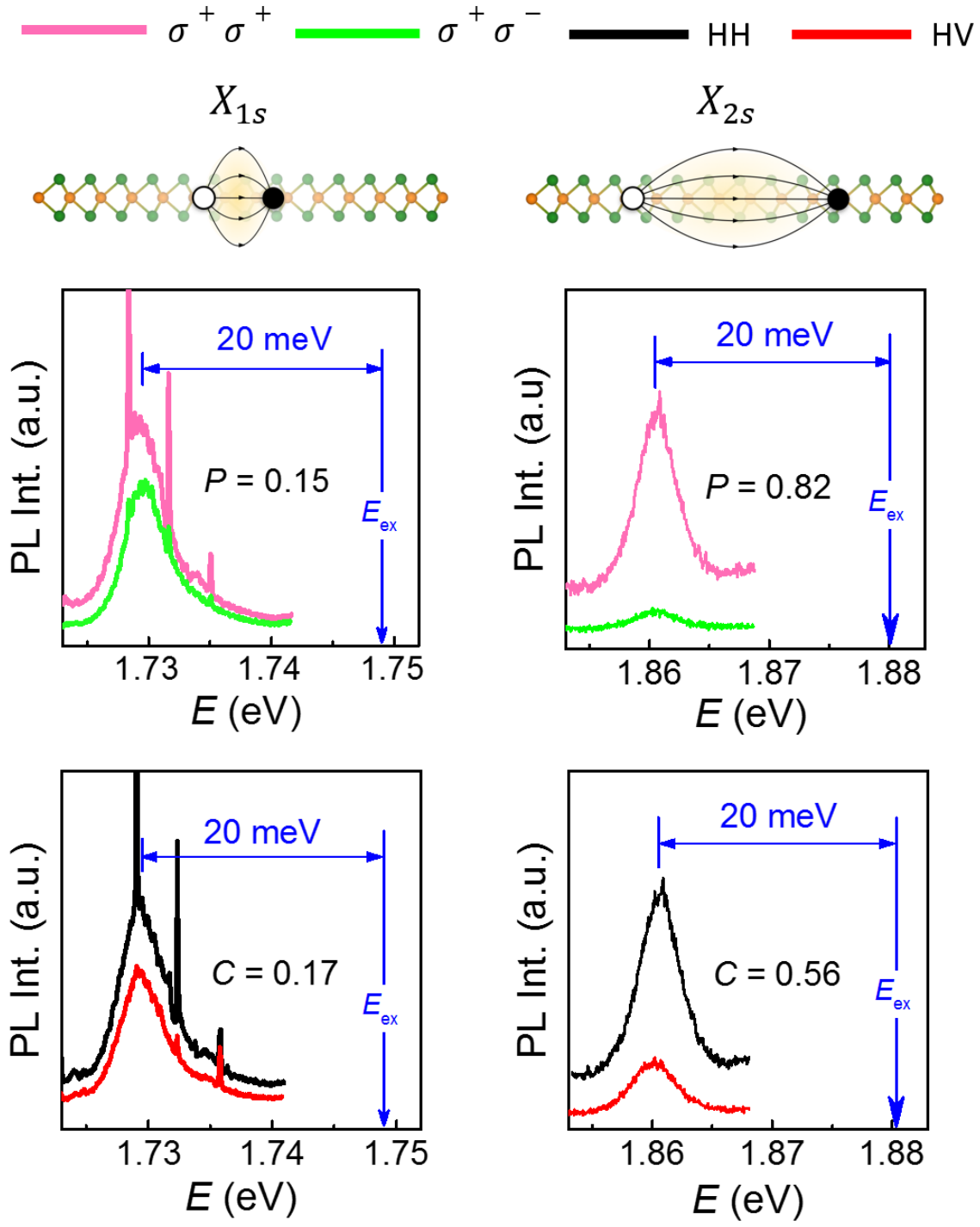

Figure 0.5: The circular and linear polarization-resolved photoluminescence of 1L-WSe_2 at 20 K with detuned excitation photon energy at 20 meV above 1*s* (left) and 2*s* (right) excitons.

The higher P and C observed in 2s exciton can be understood by the phenomenological relation:

$$P_{ns} = \frac{1}{1+\tau_{ns}/\tau_{\mathrm{s-ns}}} \qquad \text{Eq. (8.3)},$$

where τ_{ns} and $\tau_{\mathrm{s-ns}}$ is the population and polarization decay time for various Rydberg exciton state. As qualitative evidence shown in Figure 0.6, we note that the FWHM linewidth of 2s exciton (4.8 meV) is wider than the 1s exciton (4.0 meV), reflecting the 2s exciton has more decay channels such as 2s–1s transition. Quantitatively, we estimate the decay rate ratio by comparing the oscillation strength of 1s and 2s exciton. As shown in Figure 0.6, the absorption dip of 2s exciton is about 17 times smaller while the PL intensity is about 70 times smaller (see Figure 0.1b), yielding the population decay rate about 4.1 times larger of 2s exciton. Applying the τ_{1s} as 2 ps [127], and $P_{1s} = 0.15$ for 1s exiction, we can derive the polarization decay time $\tau_{\mathrm{s-1s}}$ is about 0.35 ps.

Here, by assuming that the constant polarization decay time $\tau_{\mathrm{s-2s}} = \tau_{\mathrm{s-1s}} = 0.35$ ps, we can straightforward calculate the P_{2s} is about 0.42 (using $\tau_{2s} = 2\ \mathrm{ps}/4.1 = 0.48\ \mathrm{ps}$), which is only half of the value 0.82 we acquired experimentally. The discussion above indicates that population decay rate difference alone cannot resolve the discrepancy of valley polarization of 2s. To achieve $P_{2s} = 0.82$, we find out that τ_{s-2s} has be to much larger than τ_{s-1s} about 2.2 ps, indicating the distinct polarization relaxation mechanism.

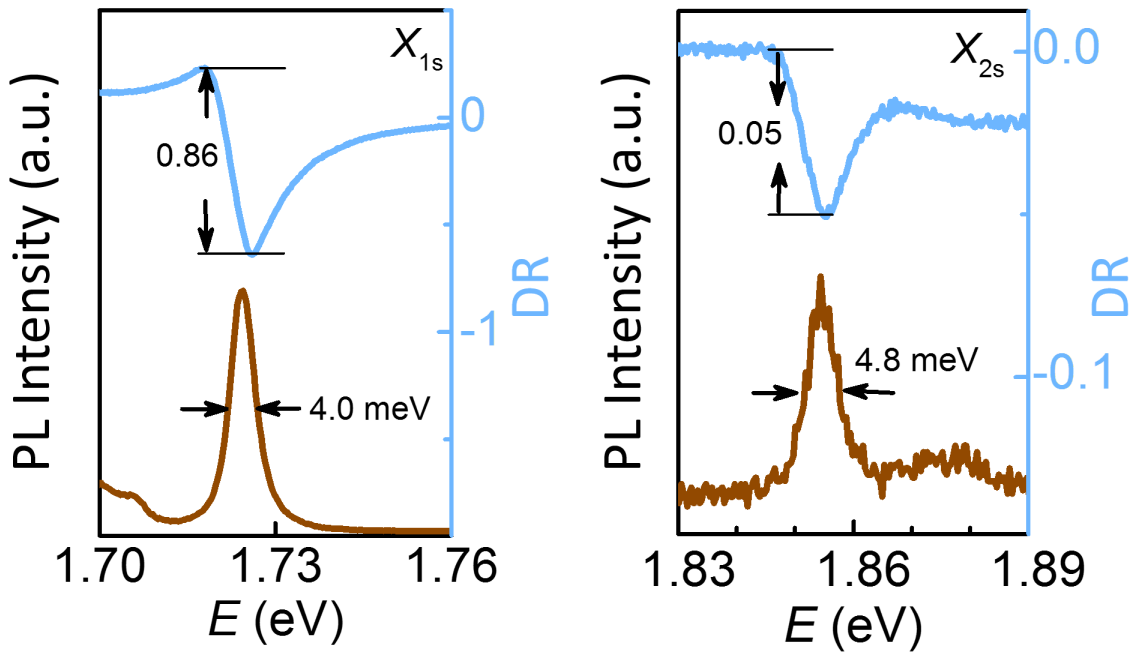

Figure 0.6: The PL and DR spectra of 1*s* and 2*s* excitons at 20 K.

8.4 Coulomb Exchange Interaction Induced Intervalley Scattering in 1L-WSe_2

In this section, we explain the drastically different valley polarization and coherence for 1*s* and 2*s* excitons in the framework of the exchange interaction MSS mechanism. As illustrated in Figure 0.7a, the strong Coulomb interaction between the photo-generated electrons and holes not only gives rise to exceptionally large exciton binding energy [18], but also leads to the annihilation of one exciton in one valley and creation an exciton in the other valley. This exchange of the excitons between the two valleys conserves energy but induces flipping of exciton angular momentum and pseudospin, compromising the valley polarization and coherence. For excitons with center-of-mass momentum $\vec{k}$, the inter-valley exchange interaction is given by [162]

$$J_{\vec{k}} = -|\psi(r_{eh}=0)|^2 \frac{a^2 t^2}{E_g^2} V(\vec{k}) k^2 e^{-2i\theta} \qquad \text{Eq. (8.4)}$$

where $\psi(r_{eh})$ is the real space wavefunction for the relative motion between the electron and the hole, $a = 3.32$ Å is the lattice constant of monolayer WSe_2, $t = 1.19$ eV is the hopping energy, $E_g \approx 2$ eV is the band gap, $V(\vec{k})$ is the $\vec{k}$ component of the Coulomb interaction, and θ denotes the direction of $\vec{k}$. Effectively this exchange interaction introduces a pseudo-magnetic field acting on the valley pseudospin of the excitons. The angular dependence in Eq. 8.4 implies that the direction of the pseudo-magnetic field depends on the direction of the exciton wavevector (Figure 0.7b). Consider, for example, a set of excitons with the same energy and pseudospin populated on a ring in the $\vec{k}$ space. The pseudo magnetic fields acting on them will have the same magnitude but different directions depending on the direction of $\vec{k}$. This makes the excitons on the ring to precess towards different directions, which in turn, causes valley depolarization and decoherence as the excitons propagate.

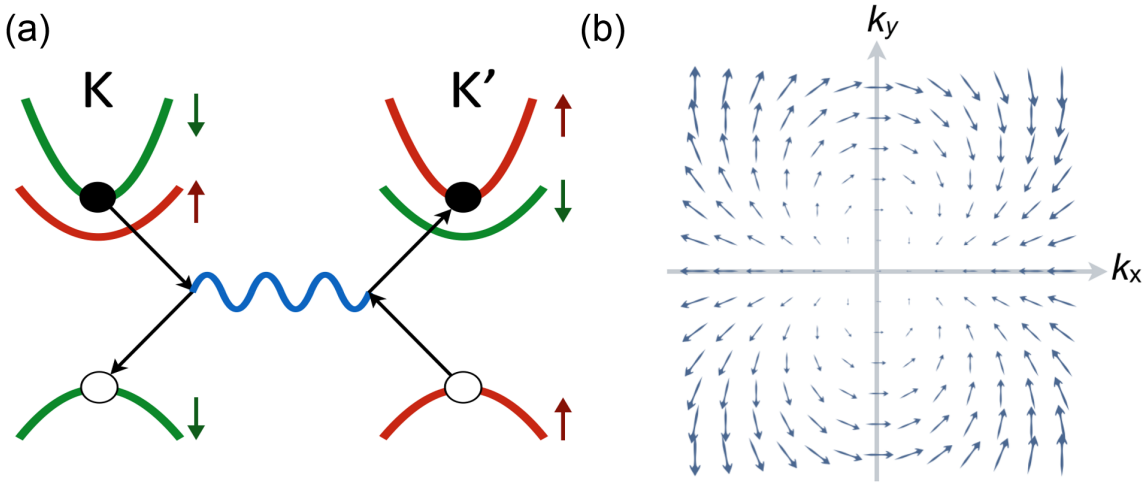

Figure 0.7: (a) The schematic showing the inter-valley electron-hole exchange interaction, which induces pseudospin flip. (b) The strength and direction of the inter-valley exchange pseudo-magnetic field in *k*-space.

In Eq. (8.4), $|\psi(r_{eh} = 0)|^2$ describes the probability density for the electron and the hole to spatially overlap. For the 1*s* exciton this is given approximately by $1/a_B^2$, where $a_B \approx 2.1$ nm. In the case of 2*s* excitons, we have measured the diamagnetic shift of 2*s* exciton (See Chapter 7) an acquired the electron-hole separation in 2*s* exciton is about 7.2 nm. By assuming that the 1*s* and 2*s* excitons have about the same reduced mass $m_r = 0.22\, m_0$, the exchange interaction of 2*s* exciton is then about 15 times weaker. This difference indeed has a significant impact on the exciton valley pseudospin dynamics. In Figure 0.8a, we simulate the pure exchange-interaction-driven valley depolarization and decoherence for excitons with different momentum k and kinetic energy $E_k = k^2/2M$; the analytically solution can be found in Ref. [31]. At $k = 0$, both P and C are equal to 1 since the exchange interaction in Eq.(8.4) goes to zero at $k = 0$; for nonzero k, both P and C of 1*s* drops steeply at finite E_k, while for 2*s* the decrease is much slower, confirming that 1*s* is more impacted by the exchange depolarization fields.

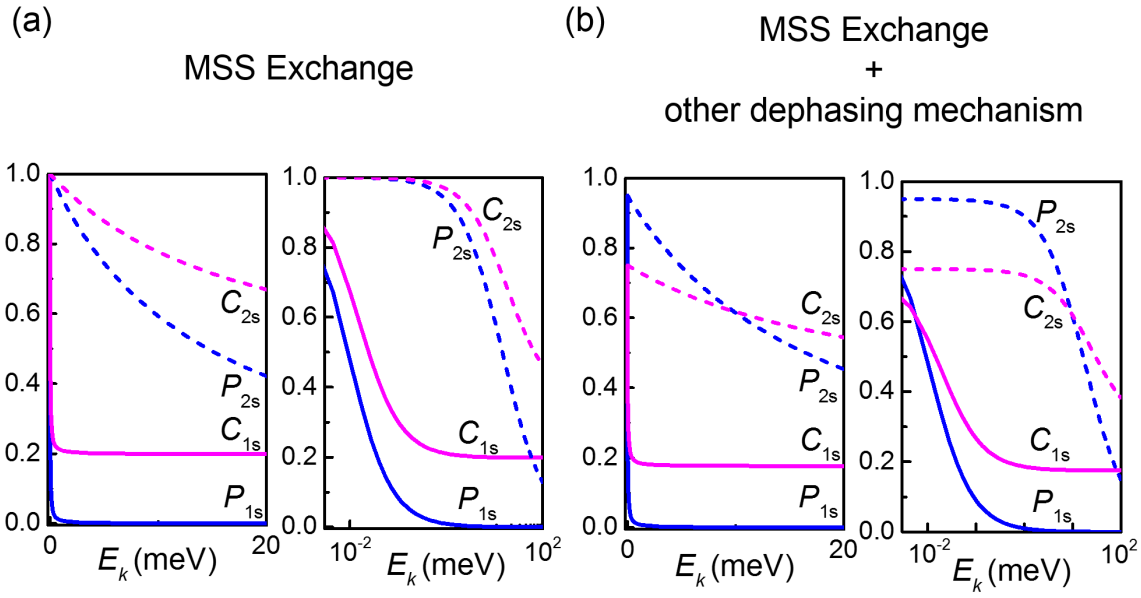

Figure 0.8: (a) The simulated valley coherence (*C*) and polarization (*P*) as a function of E_k for 1*s* and 2*s* excitons considering pure exchange interactions. The left (right) panel is in linear (semilog) scale. (b) Simulated *C* and *P* considering both exchange interactions and other depolarization and decoherence mechanisms

It is of interest to note that for both 1*s* and 2*s* simulations in Figure 0.8a, *C* is always larger than *P* — this is a hallmark of exciton exchange interaction in 2D [129]: the exchange-interaction-induced pseudo-magnetic-fields are in the plane of the atomic layer, thus the out-of-plane pseudospin of valley polarized excitons experiences the pseudo magnetic fields in two directions, while the in-plane pseudospin of the valley coherent excitons is relaxed only by the magnetic field component that is perpendicular to the pseudospin. Experimentally, we have observed *C* to be larger than *P* for 1*s* in Figure 0.5 as well as with many other laser excitations (more data is displayed in the next section Figure 0.9b), further confirming that the exchange interaction dominates the 1*s* exciton valleytronic behavior. This is consistent with another recent study on high-quality MoS_2 where *C* is also found to be larger than *P* [111].

For 2*s* excitons, however, *P* is significantly larger than *C*. This suggests that with weaker 2*s* exchange interaction, other decoherence and depolarization mechanisms become more competitive. To account for these additional mechanisms, we add another depolarization decay time in our model [31] such that even for $k = 0$, *P* and *C* are smaller than 1. This relatively simple model captures our observations semi-quantitatively: as shown in Figure 0.8b, for excitons with small kinetic energy ($E_k < 10$meV), *P* is mostly larger than *C* for 2*s* exciton and smaller than *C* for 1*s*, and numerically the 2*s* *P* and *C* values are much larger than 1*s*. In fact, our conclusion in Chapter 7 also shows that 2*s* excitons are distributed narrower in k-space, matching our simulation results where 2*s* exciton has larger *P* and *C* with small kinetic energy.

8.5 Enhancing Valley Polarization and Coherence by Incorporating Interlayer Phonon Scattering

Excitons can only become radiative if its momentum lies within the light cone, whose boundary corresponds to 1*s* and 2*s* exciton kinetic energy of ~10 μeV. At such small E_k's the impact of exchange interaction is negligible. However, the experimental data shows the large difference between *P* and *C* for 1*s* and 2*s*, indicating the excitons outside the light cone with larger momentum provide a reservoir where disorder and phonon can scatter them into the light cone, which subsequently radiate [154]. The average exchange interaction that the radiatively recombined excitons experienced is thus much larger than the fields inside the light cone, as we discussed in Chapter 8.4.

In this section, we show that it is possible to reduce the impact of exchange interaction fields on 1*s* by using the small-momentum 2*s* exciton as an alternative reservoir, assisted by multiple zone-center phonon scattering [163]. With the presence of hBN, the 2*s* exciton can lose the excess ~130 meV by emitting zero-momentum hBN-WSe_2 combinational phonons (as illustrate on top of Figure 0.9a). This reduces the number of phonons involved from six [163] to two, and markedly improves the radiative cross-section. Figure 0.9a demonstrated the PLE measurement of 1*s* exciton. The intensity of the 1*s* exciton is dramatically enhanced when the 1s exciton overlapping with the hBN+WSe_2 combinational phonon modes. We note that this interlayer phonon coupling effect is quite interesting and unique in the 2D van der Waals heterostructures and has been extensively studied recently [164–166].

In Figure 0.9b, we extract the *P* and *C* of 1*s* exciton with laser excitation scanning from 1.84 to 1.89 eV, covering the energy range of the 2*s* exciton to explore the impact of 2*s*–1*s* transition. When the excitation is off resonance, *P* and *C* are in the range of 0.1 to 0.2. When on-resonance with 2*s* exciton, the *P* and *C* are markedly improved to 0.30 and 0.64 respectively. This improvement results from using the small-momentum 2*s* exciton as a high-quality reservoir for the 1*s* luminescence. The 2*s* exciton reservoir is prepared by illuminating the sample with photons that match the 2*s* exciton energy. The reservoir excitons subsequently lose ~ 130 meV excess energy through phonon emission. As a side note, in Figure 0.9b we observe that *C* is larger than *P* over the whole PLE range, confirming that exchange interaction dominates the 1*s* valley depolarization and decoherence as discussed in Chapter 8.4.

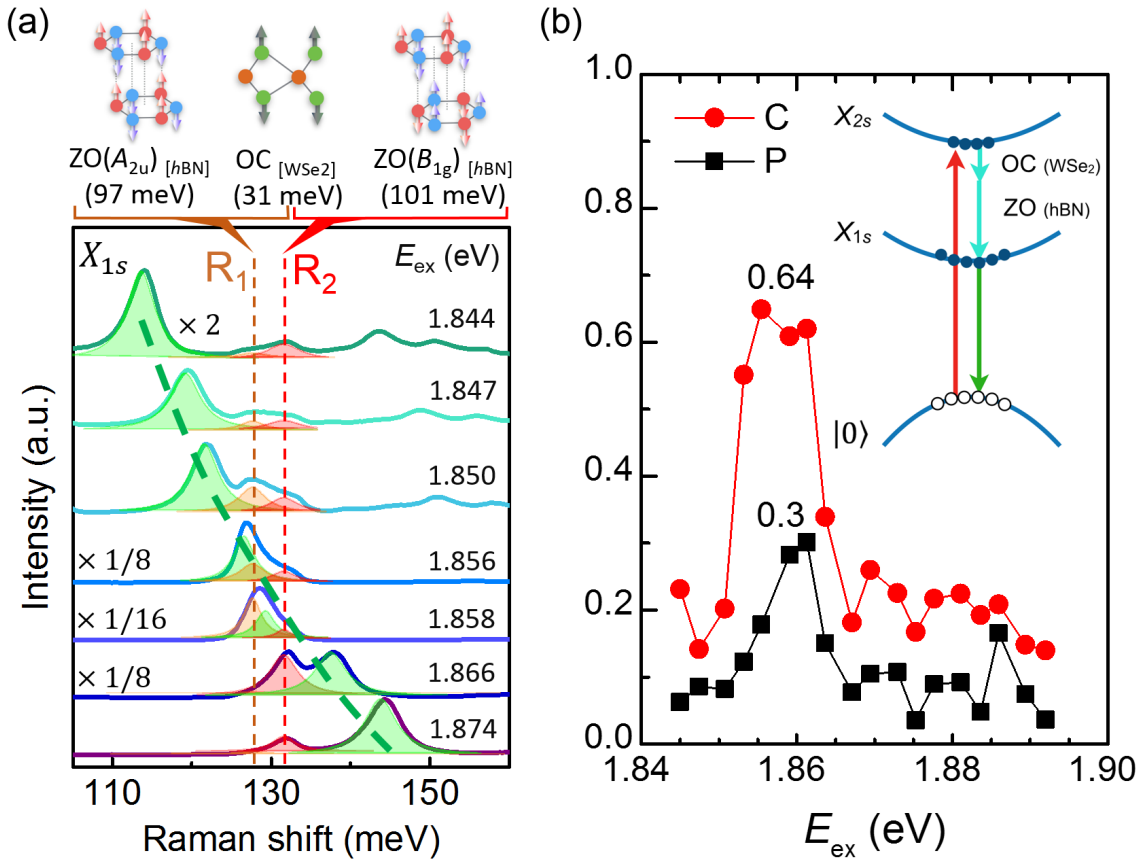

Figure 0.9: (a) Resonant Raman scattering of R_1 and R_2 using photon energies from 1.844 to 1.874 eV. The peaks guided by dashed curve are the 1*s* exciton luminescence. (b) *C* and *P* of the 1*s* exciton emission as a function of laser excitation energy.

The same mechanism can also be adopted to improve the P and C of 2s excitons. In Figure 0.10a we demonstrate the resonant Raman spectra with various excitation laser from 1.886 to 1.905 eV. We observe that not only zone center phonon (OC and IMC) but also several finite-k phonons are strongly resonant with 2s exciton emission and become visible. As we displayed in Chapter 7, the energy different of 3s/4s exciton is about 25/35 meV higher than 2s exciton. The energy difference coincidently matches well with the phonon branches of 1L-WSe_2 [52], enabling the incoming resonance with 3s/4s exciton and outgoing resonance with 2s exciton. In addition, the finite-k phonons can further assist to scatter the excitons into the light cone and then emit, providing additional fast population decay channels.

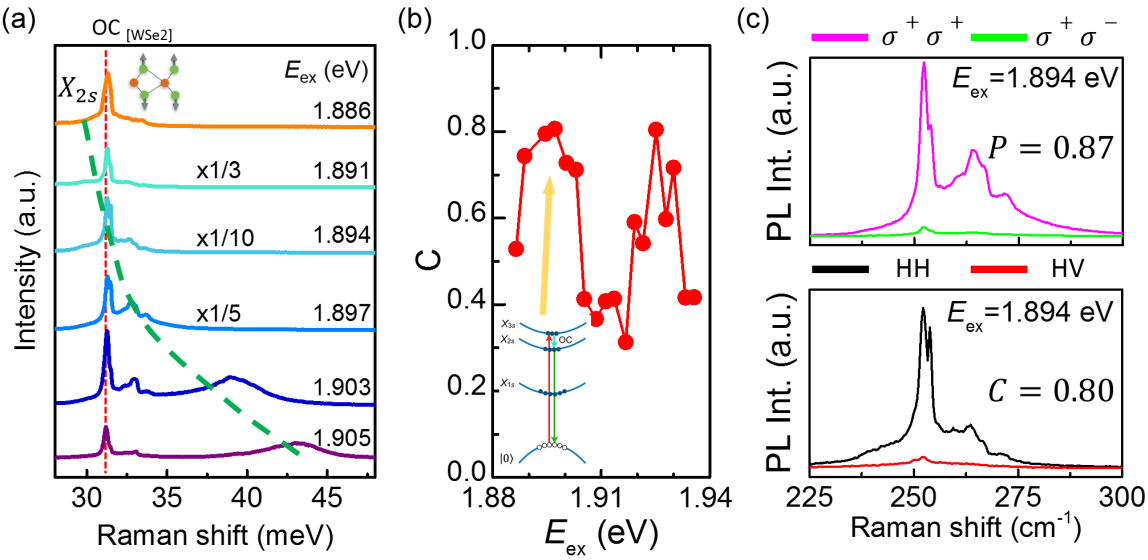

Figure 0.10: (a) Resonant Raman scattering of WSe_2 OC mode using photon energies from 1.886 to 1.905 eV. The peaks guided by dashed curve are the 2s exciton luminescence. (b) The calculated C of 2s exciton emission as a function of laser excitation energy. The resonant showing up at 1.894 eV involves the incoming resonance with 3s exciton and outgoing resonance with 2s exciton. (c) The circular and linear polarization-resolved photoluminescence of 1L-WSe_2 at 4 K with excitation photon energy at 3s exciton.

As can be seen in Figure 0.10b, the valley coherence of 2*s* excitons is dramatically enhanced when the energy differences match either one phonon energy (left peak, $\Delta E \sim 250$ cm^{-1}) or the combination of two phonons (right peak, $\Delta E \sim 500$ cm^{-1}). The enhancement of valley coherence can be understood by both fast population decay and the reduction of Coulomb exchange interaction. As demonstrated in Figure 0.10c, by employing resonant phonon scattering, the *P* and *C* of 2*s* exciton can be further improved to $P = 0.87$ and $C = 0.80$.

8.7 Summary

In conclusion, we have accessed the 2*s* radiative emission in hBN sandwiched high-quality 1L-WSe_2 crystals. The 2*s* luminescence is highly robust and can be also access at room temperature due to its large binding energy. In addition, the 2*s* exciton exhibits superior valley polarization and coherence. This observation could be facilitated in part by the fast population decay of 2*s*, and our analysis further points to the action of intervalley Coulomb exchange interaction in TMDC pseudospin propagation. Our studies provide key insights into the TMDC intervalley scattering processes which are essential for developing TMDC-based valleytronic devices. Moreover, we demonstrate that achieving the *P* of 0.3 and *C* of 0.64 for 1*s* and *P* of 0.87 and *C* of 0.80 for 2*s* exciton by incorporating the zone center phonons from hBN and WSe_2 resonant with the Rydberg exciton states. Not only the phonons in WSe_2 but also the phonons on the approximate materials can take part in this process to create an efficient emissive recombination channels.

CHAPTER 9

DYNAMICS OF EXCITONIC COMPLEX IN 1L-WSE_2

9.1 Research Objective and Motivation

The reduction of screening of Coulomb interaction in atomically thin 2D material results in the tightly bound 1*s* exciton in 1L-WSe_2. Several interesting physics properties we have discussed in previous chapters. The large binding energy of 1*s* exciton is about 170 meV and the radius is only around 2 nm. The confinement in both out-of-plane direction and in-plane axis directly link to the strong many-body correlation, reflected by the observation of multi-particles bound states as we show in Chapter 6. It is desirable to study the dynamics between these bound states. For example, the competition between Coulomb exchange interaction and the population lifetime of the excitonic states is an important issue related to the valley polarization and coherence which we have investigated in Chapter 8.

9.2 Experimental Setup of Time-resolved Photoluminescence

Figure 0.1 illustrates the experimental setup of time-resolved photoluminescence measurement. We employ a supercontinuum white laser (Fianium WhiteLase) with a pulse width of about 20 ps and a repetition rate of 20 MHz. The white laser is filtered by several spectral filters to acquire a clean 530 nm excitation. The laser is then focused on the sample mounted in a cryostat with the spot size about 2 μm. To measure the PL spectra, the signal is collected and then detected by a liquid nitrogen cooled CCD device.

A time-correlated single-photon counting (TCSPC) method (PicoHarp 300) was used to perform the time-resolved PL spectroscopy with the resolution of 4 ps.

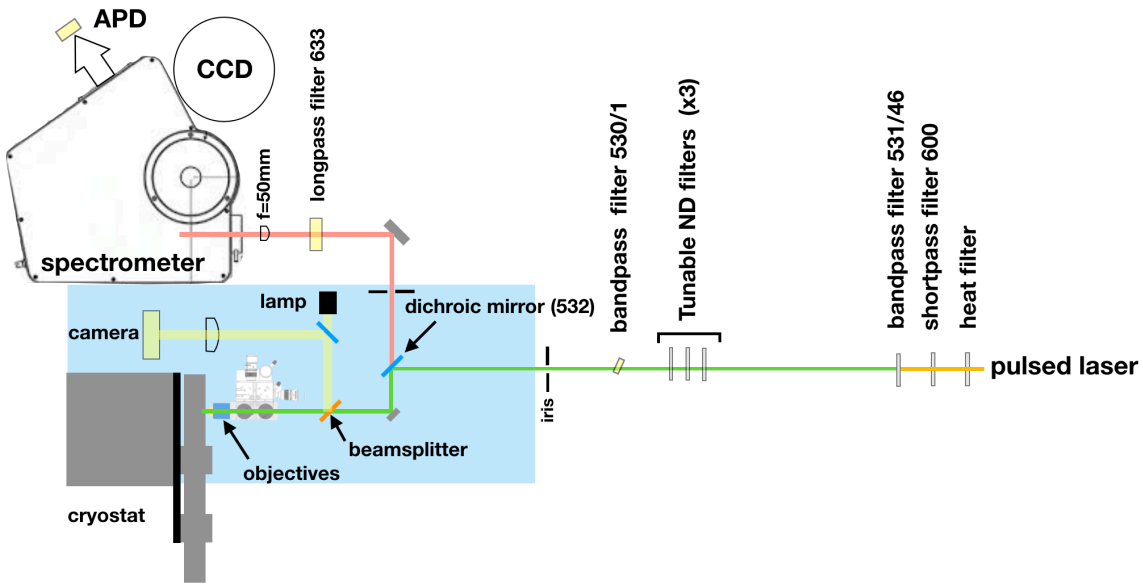

Figure 0.1: Experimental setup of the time-resolved photoluminescence measurement.

9.3 Preliminary Results on Lifetime of the Excitonic States

Figure 0.2 illustrates the typical time-resolved PL intensity of 1*s* exciton in 1L-WSe_2 at 7 K. The dots are the photon counts as a function of time while the shaded area reflects the instrumental response function (IRF) about 87 ps in FWHM. The population decay of 1*s* exciton can be fitted by a two-time-constant exponential decay function, given the fast component rate about 31 ps and a slow component about 210 ps. A recent paper reported the 2 ps decay time of 1*s* exciton measured by a ultrafast streak camera [127] which has been interpreted as the intrinsic radiative recombination lifetime under quasi-resonant excitation. The lifetime of 31 ps we measured here is thus limited by the detection speed of detector. The slow component of 210 ps has been interpreted as the signature of exciton thermalization: the radiative window is small and thus yields a radiative decay time longer than the intrinsic recombination time. The two-time-constant feature observed in Figure 0.2 indicates X_{1s} is a hot excitonic state.

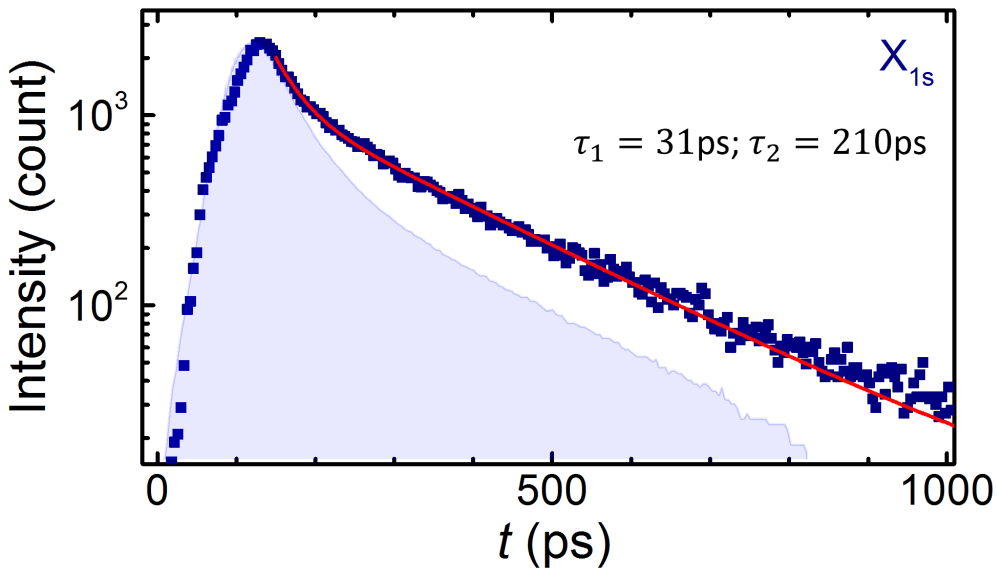

Figure 0.2: A typical time-resolved PL signal of 1*s* exciton at 7 K. The solid curve is fitted by a two-time-constant exponential decay function. The shaded area is the IRF.

Figure 0.3a displays a typical PL spectra for 1L-WSe_2 excited by the pulsed laser. Taking the advantage of the pulsed laser, we are able to observe these multi-particles bound XD and TD states under even lower power about 1 μW, avoiding the heating issues observed in CW laser excitation measurement [25]. Figure 0.3b shows the lifetime measurement of these XD and TD, complementary to the discussion in Chapter 6. The XD exhibits similar two-time-constant exponential decay as X, implying that XD is not a ground state. This result is consistent with our assignment that XD is composed by a X and D, where X is the hot exciton. In contrast, the intensity decay of TD peak can be described by using only one-exponential decay function with the lifetime of 250 ps, indicating the TD state is in thermal equilibrium [127].

Interestingly, in Figure 0.3a we observe other three intense modes denoted as X', L1 and L2 showing up in the energy of about 60 meV, 103 meV and 116 meV below the X, respectively. As can be seen in Figure 0.3c, X' mode is anticipated to has less decay channels, showing the slightly longer lifetime of 270 ps than the TD. Turning to even lower energy, L1 and L2 modes have longer decay time about 295 ps and 320 ps, respectively. In addition, both L1 and L2 modes have another decay component with ultralong lifetime in the order of 100 ns, which may be from the exciton bound by deep-level defect states. In fact, the L1 and L2 peak have been attributed to the defect activated modes, demonstrated by a strong electron-beam irradiation [167]. However, our preliminary data delivered in the following reveal the unusual physical properties, distinct from the model of defect bound exciton states.

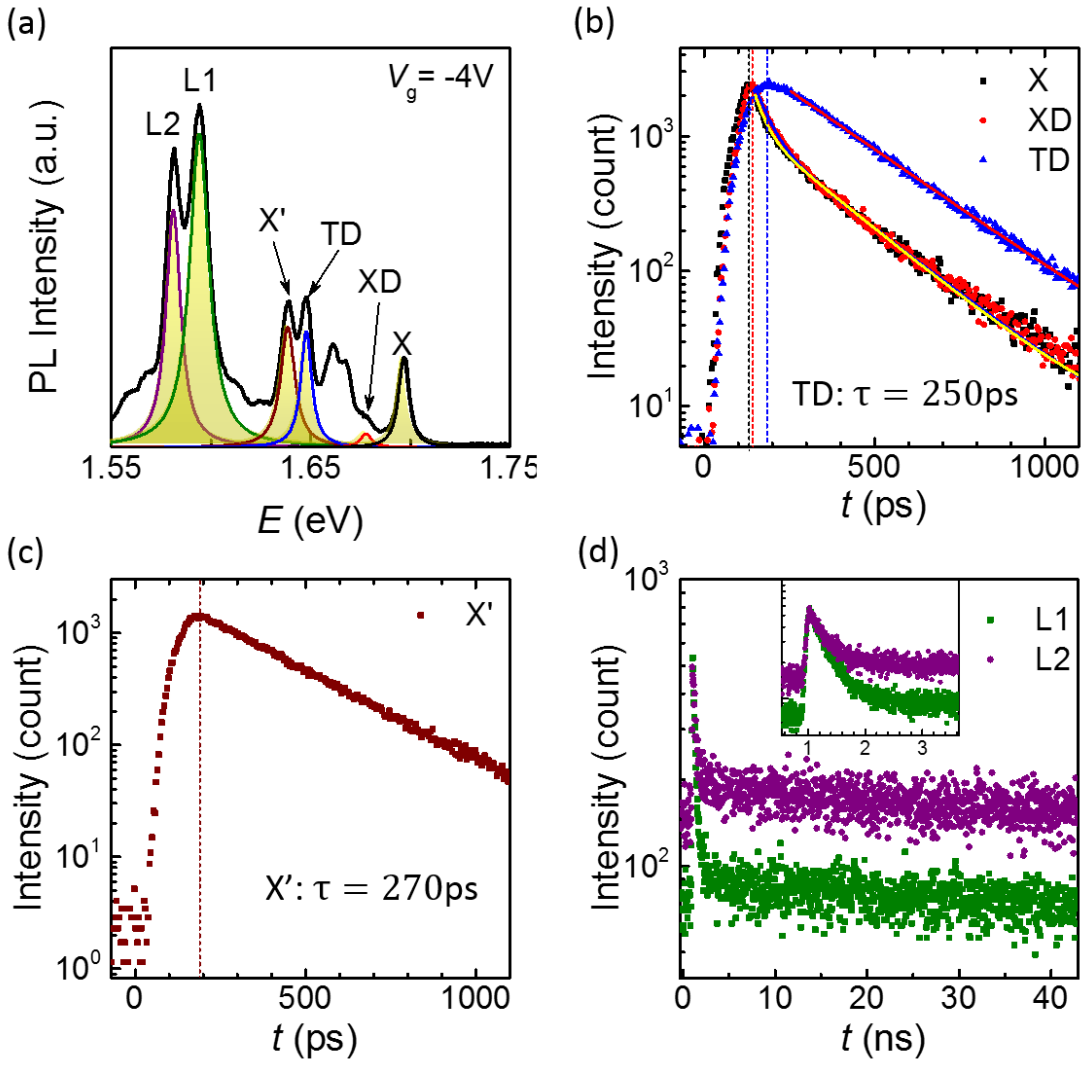

Figure 0.3: (a) The PL spectra of 1L-WSe_2 excited by a 20 ps pulsed laser at 7 K. (b) The time-resolved PL of X, XD and TD bound states. The solid curves are exponential fittings. The dashed line indicates the time of intensity peaked. (c) The time-resolved PL of X' state. (d) The time-resolved PL of L1 and L2 states. Inset: the zoom in data during the initial 3 ns.

9.4 The X', L1 and L2 Low Energy Bound States

We first investigate the gate voltage tuning of the PL spectra. Figure 0.4a illustrates the color map of gate dependent PL spectra. At the charge neutral point about $V_g = -9$ V, as can be seen in Figure 0.4b, only X, XD and X' modes are presented in the maximum intensity, implying that the X' is a charged neutral state. As the gate voltage increase (electron doping), the L1 and L2 peaks appear and go up and dramatically. As the V_g goes beyond 4 V, as denoted in the white dashed line in Figure 0.4a, the X, L1 and L2 start blue shifting. This effect can be explained by the Pauli blocking effects observed in X when the Fermi-level is tuned above the upper conduction band [25,146,168]. In addition to peak energy shift, we further observe that the intensity of X is strongly quenched above this gate voltage while the L2 is dramatically increased.

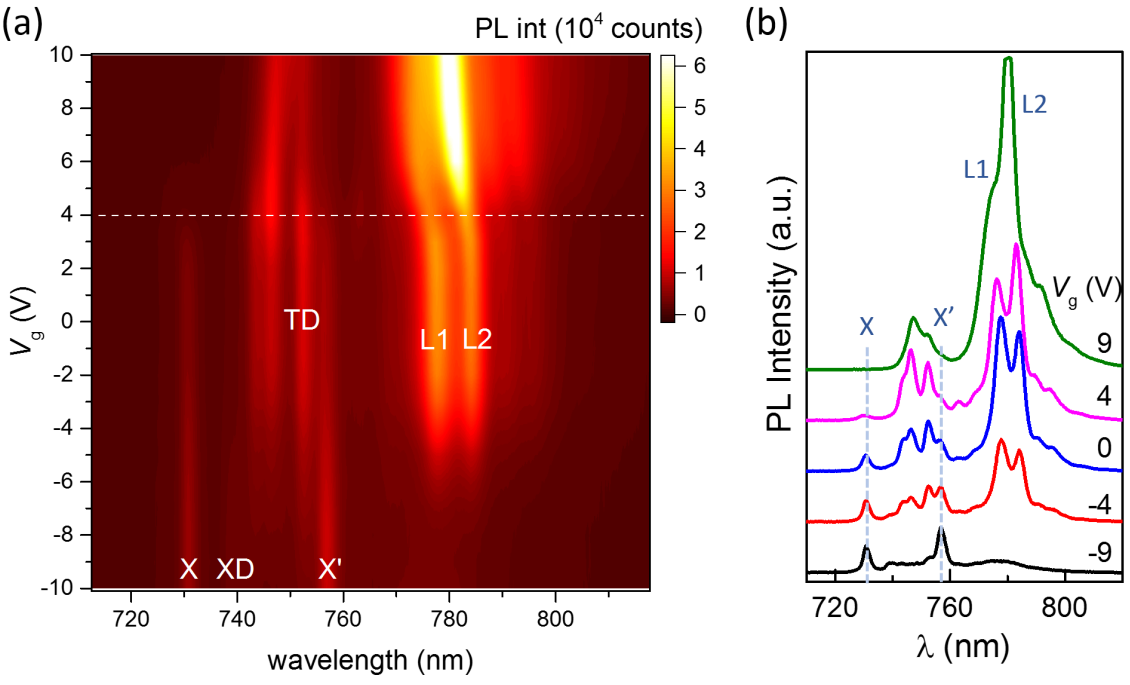

Figure 0.4: The contour map of gate voltage dependent PL spectra. Charge neutral point is about $V_g = -9$ V. The white dashed line indicates the turning point we discussed above. (b) The selected PL spectra at the corresponding gate voltages.

We further examine the excitation power dependent intensity of L1 peak. Figure 0.5a displays the PL under several different orders of excitation fluence at the $V_g = 0$V. As can be seen in the bottom penal, we can only observe L1 and L2 peak in the spectra, indicating that these states indeed a dominant interaction of the exciton in 1L-WSe_2. With the increasing excitation fluence, other high energy excitonic species growing up as demonstrated in the top penal in Figure 0.5a. To further understand the excitation fluence dependence, we extract the intensity of L1 mode and plot them as a function of excitation fluence in Figure 0.5b. The PL intensity simply increases under low excitation fluence condition ($<6 \times 10^{-12}$ J/cm^2). In contrast, the PL intensity deviates from a simple linear dependence and eventually saturates at the excitation fluence about 6×10^{-9} J/cm^2. The sublinear saturation behavior in higher excitation fluence has been interpreted as the fully population of the localized states [169] or the exciton-exciton annihilation [170]. In our time-resolved PL in Figure 0.3d, the two constant exponential decay in L1 and L2 modes is a signature of the exciton-exciton annihilation process which has been demonstrated with the free exciton X in atomic layered TMDCs [170,171]. While in our experimental results, the critical excitation fluence is 6 orders less than the value reported in previous studies on free exciton. This indicates that the defects may localize the excitons and activate the exciton-exciton annihilation effect even in a low excitation density. We thus can estimate the defect density of our sample by assuming the 10% absorption of photons and all the generated excitons are bound to the defect site. By choosing the saturation fluence of about 10^{-8} J/cm^2, we can estimate the defect density about 2.8×10^9 cm^{-2}.

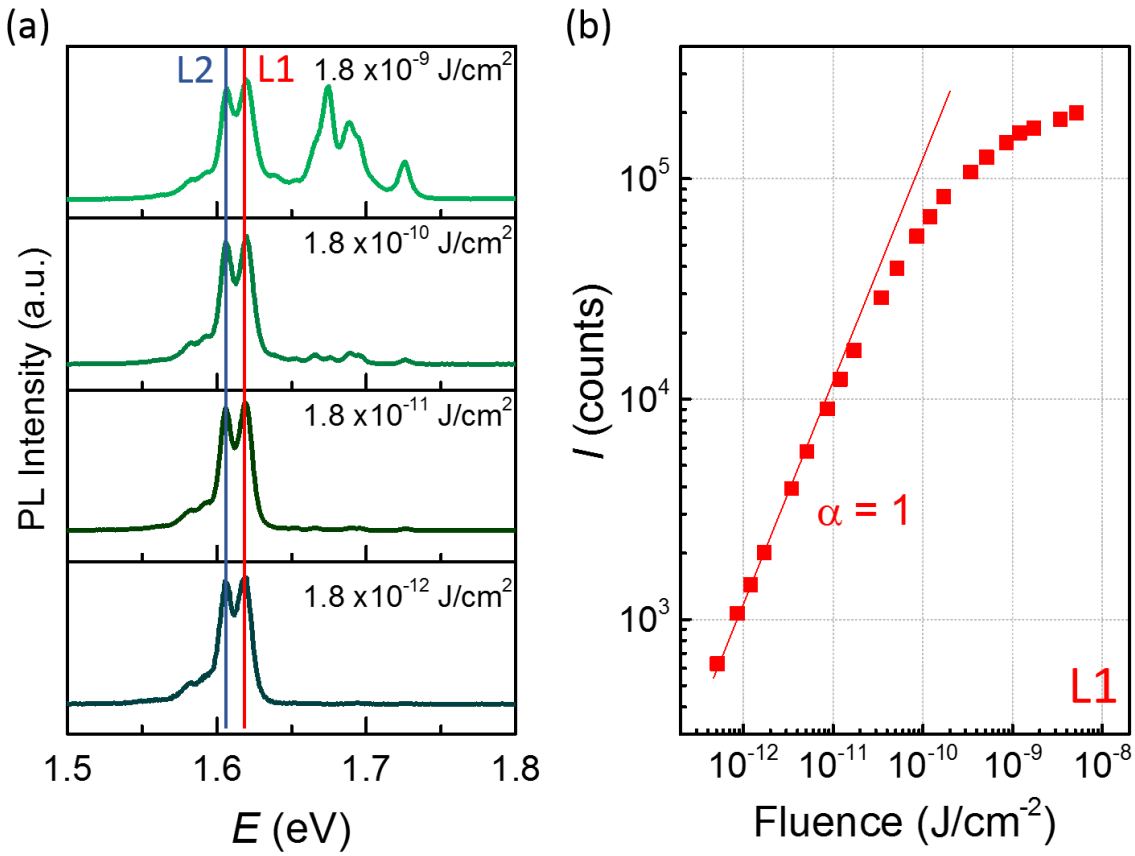

Figure 0.5: (a) The PL spectra excited by various excitation energy densities. (b) The log-log plot of intensity of L1 peak vs. excitation energy density. The trend follows the linear trends at low energy density while is saturated in the high fluence.

We gain the further insight of the nature of the L1 and L2 localized states by performing the helicity-resolved PL measurement in magnetic fields. Figure 0.6a shows the both σ^- and σ^+ emissions under various out-of-plane magnetic fields. The magnetic field break the valley degeneracy and thus induce the exciton repopulation between K and K' valleys. For X mode, no significant difference of intensity in two valleys, consistent with data presented in Figure 0.11. However, we observe that both L1 and L2 peaks exhibit significant difference of intensity in two valleys Specifically, under a positive magnetic field, the L1 and L2 bound excitons prefer to populate to the lower energy K valley than the K' valley. This can be explained by the long lifetime which enables the thermal equilibrium of high and low energy states, in contrast to the X which has ultrashort lifetime about 2 ps. We note that the L1 and L2 exhibit large `positive' valley polarization P_V (the definition we used in Chapter 6.7), contrary to the XD and TD modes which possess the large negative P_V. It is interesting to note that X' mode at 60 meV below X also exhibit large negative P_V. We suggest that this mode could be from the biexciton states composed by two dark excitons.

The Zeeman shift of each mode encodes the magnetic dipole moment of the involved electronic bands. In Figure 0.6b, we extract the energy different of X and L1 emission form K and K' valley at various magnetic fields and linearly fit their *g*-factors. The *g*-factor of X is about 2.1, which is the sum of the contribution from the intravalley and intervalley components in magnetic dipole moments, as discussed in Chapter 6 and 7. Surprisingly, we find that the L1 and L2 exhibits *g*-factor up to 5.8. The enhancement of *g*-factor has been interpreted due to the strong Coulomb interaction [147] and the Landau Level splitting in highly doped 1L-WSe_2 [146].

At last, we plot the intensity of L1 mode as a function of the peak energy from the spectra we acquire in several magnetic fields in Figure 0.6c. We found that the intensity can be well captured by a Boltzmann distribution function,

$$I = I_0 + \frac{A}{e^{(E-\mu)/kT}+1} \quad \text{Eq. (9.1)},$$

where μ is the chemical potential, I_0 and A are fitting parameters. This result again indicates that the L1 is in thermal equilibrium. The fitting temperature is about 7 K, matching closely to the experimental temperature 4 K.

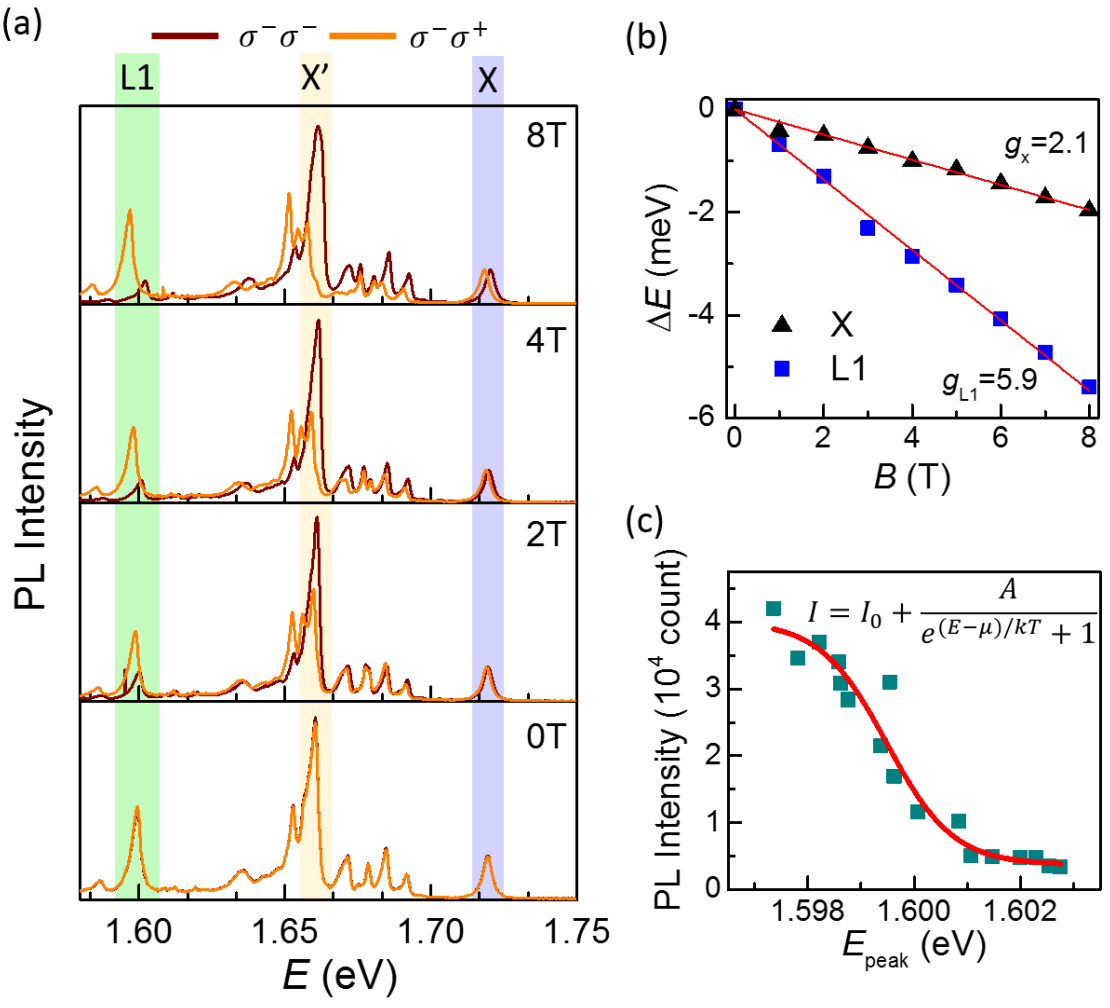

Figure 0.6: (a) The helicity-resolved PL spectra at various magnetic fields. (b) The peak energy as a function of magnetic fields. (c) The peak energy dependent intensity of L1 mode. The red line is the fit by Boltzmann distribution.

9.5 Summary and Future Work

In this chapter, we explore the many-body correlation of the exciton in 1L-WSe_2 by examining the lower energy states. These states had been attributed to the defect activated bound excitons in literatures. However, in our high quality sample, these low energy states become well defined sharp peaks and exhibit interesting physical properties. To realize the origin and the underline physics, more theoretical and experimental studies are needed.

CHAPTER 10

CONCLUSION REMARK

The recent theoretical and experimental studies unveil the novel physics in 2D materials. In this dissertation, we employed the polarization resolved Raman and PL spectroscopy to characterize the quantized excitation including phonon and excitons in 2D-TMDCs which possess rich intralayer and interlayer polytypes, providing an intriguing platform to study the of photon-electron and photon-phonon interaction. We first carried out the comprehensive results on the six generic phonons in the H-TMDCs atomic layers in Chapter 3. We assigned the phonon modes accurately with the assist of polarization-resolved measurements. The energy of phonon modes has been further applied as the signature of number of layer and polytypes, reflecting that the phonons are closely related to the lattice structures. We found the similar technique and framework can also been used in the cousin of H-TMDCs: T'-TMDCs exhibit interesting physics in Weyl semimetallic and topological insulating phases. As we demonstrated in Chapter 4, the polarization resolved Raman spectroscopy can tell the crystal orientation and provide a direct evidence of inversion symmetry breaking. The Raman spectroscopy has been widely applied to gauge the crystal quality. This becomes extremely important in 2D materials due to the large surface/volume ratio. We thus demonstrated the *in situ* monitoring of crystal quality of 1L T'-(Mo, W)Te_2 by polarization resolved Raman spectroscopy in Chapter 5. Distinct from the conventional method which monitors the intrinsic phonon modes, we proposed by looking at Raman modes from the by-product after degradation. We anticipate that this method could be potentially applied to other air sensitive 2D materials, especially in the atomic layer limit. Out results shown from

Chapter 3 to 5 as well as the appendix A and B provides comprehensive references for the future studies on the phonons in 2D materials.

In the second part of dissertation, we explore the optical properties of the tightly bound exciton in 1L-WSe_2 by different spectroscopy techniques. Several important issues are raised to realize the many-body correlation of exciton and its valley dynamics. In chapter 5, we focus on the multi-particle bound states associated with 1*s* bright exciton in high quality 1L-WSe_2 sample. In addition to the bright exciton and trions, we observed the multi-particle bound biexciton and exciton-trion emissions. The magnetic field dependent PL measurements further demonstrate the negative valley polarization of biexciton and exciton-trion, revealing the unique intervalley configuration involving dark exciton. In Chapter 6, we study the Rydberg excitonic states by performing the PL spectroscopy in high magnetic fields. The high magnetic fields as well as high sample quality enable us to observe at the first time the 3*s* and 4*s* exciton PL emissions, which are further confirmed by measuring their diamagnetic shifts. In addition, we found that the *g*-factors in higher excited excitons is larger, pointing out the size dependent magnetic dipole moments in the Rydberg excitons. In Chapter 7, we focus on 2*s* exciton PL emission which is quite robust even at the room temperatures. We found that the 2*s* exciton exhibits much higher valley polarization and valley coherence than 1*s* exciton. Quantitative analysis shows that the electron-hole exchange interactions plays a significant role due to the reduced of electron-hole wavefunction overlapping in 2*s* exciton, consistent with our finding in Chapter 7. We further demonstrate by employing the phonons-exciton resonance effect to achieve the superior *P* and *C* for 1*s* and 2*s* excitons.

Finally, we reported our preliminary results on the low energy bound states in Chapter 9. We demonstrate the time-resolved PL and magneto-optical measurements on these modes, revealing their unusual physical properties. Our results open a window for the investigation of the many body correlation of excitons in atomically thin materials.

APPENDIX A

RAMAN TENSORS FOR TMDCS POLYMORPHS

Table A.1: The Raman tensors for the atomic layered and bulk TMDCs polytypes mentioned in this dissertation. (adopted from Ref. [50])

system	class	materials	Raman tensor
monoclinic	C_{2h}	bulk T'$_{mo}$-MoTe2 1L T'-MoTe2 1L T'-WTe2	A_g $\begin{bmatrix} a & & d \\ & b & \\ d & & c \end{bmatrix}$ B_g $\begin{bmatrix} & e & \\ e & & f \\ & f & \end{bmatrix}$ *m* mode *z* mode
orthorhombic	C_{2v}	bulk T'$_{or}$-$MoTe_2$ bulk WTe_2	A_1 $\begin{bmatrix} a & & \\ & b & \\ & & c \end{bmatrix}$ B_1 $\begin{bmatrix} & & d \\ & & \\ d & & \end{bmatrix}$ A_2 $\begin{bmatrix} & e & \\ e & & \\ & & \end{bmatrix}$ B_2 $\begin{bmatrix} & & \\ & & f \\ & f & \end{bmatrix}$ *m* mode *z* mode
trigonal	D_{3d}	even layer H-TMDCs (AB stacking)	A_{1g} $\begin{bmatrix} a & & \\ & a & \\ & & b \end{bmatrix}$ E_g $\begin{bmatrix} c & & \\ & -c & d \\ & d & \end{bmatrix}$ E_g $\begin{bmatrix} & -c & -d \\ -c & & \\ -d & & \end{bmatrix}$ OC, OMC, B IC, IMC, S
hexagonal	D_{3h}	odd layer H-TMDCs (AB stacking)	A_1' $\begin{bmatrix} a & & \\ & a & \\ & & b \end{bmatrix}$ E" $\begin{bmatrix} & c & \\ c & & \\ & & \end{bmatrix}$ E" $\begin{bmatrix} & & -c \\ & & \\ -c & & \end{bmatrix}$ E' $\begin{bmatrix} d & & \\ & d & \\ & & \end{bmatrix}$ E' $\begin{bmatrix} d & & \\ & -d & \\ & & \end{bmatrix}$ OC, OMC, B IC, IMC, S LA, TA, IC, IMC, shear
	D_{6h}	bulk H-TMDC	A_{1g} $\begin{bmatrix} a & & \\ & a & \\ & & b \end{bmatrix}$ E_{1g} $\begin{bmatrix} & c & \\ c & & \\ & & \end{bmatrix}$ E_{1g} $\begin{bmatrix} & & -c \\ & & \\ -c & & \end{bmatrix}$ E_{2g} $\begin{bmatrix} d & & \\ & d & \\ & & \end{bmatrix}$ E_{2g} $\begin{bmatrix} d & & \\ & -d & \\ & & \end{bmatrix}$ OC IC IMC, S

APPENDIX B

PHONON ENERGIES OF ATOMIC LAYERED H-TMDCS

Table B.1: The experimental extracted energy (cm^{-1}) of six prototypical optical phonon modes in atomic layered H-TMDCs. The excitation is argon laser. The data is taken at room temperature with excitation power less than 100 μW.

H-TMDC		1L	2L	3L	4L	5L
MoS_2	S		24.2	29.6	31.2	
	B		41.6	30.1	23.5/54.1	
	IC		286.3	285.6	286.2	
	IMC	386.3	384.9	384.2	384.1	
	OC	404.1	406.1	407.2	408.1	
	OMC		-	-	-	
WS_2	S		19.6	24.2	-	
	B		33.8	27.0	-	
	IC		-	-	-	
	IMC	359.0	358.3	358.0	-	
	OC	420.4	420.8	421.2	-	
	OMC		-	-	-	
$MoSe_2$	S		21.0	24.9	26.4	
	B		34.3	24.5	18.2/45.4	
	IC		170.4	169.7	170.3	
	IMC	288.6	287.4	284.2/287.2	283.9/287.0	
	OC	241.8	242.8	239.9/243.0	240.9/243.2	
	OMC		355.2	353.5/355.0	353.7/355.2	
WSe_2	S		17.7	21.6	23.2	
	B		29.1	20.5	15.7/38.0	
	IC		177.0	176.8	176.6	
	IMC	250.8	249.6	249.1	248.9	
	OC	250.8	251.2	251.4	251.6	
	OMC		310.3	310.0	309.6	
$MoTe_2$	S		19.6	24	10.4/25.3	16.7/26.2
	B		28.6	20.9	16.2/37.9	12.6/32.9
	IC		118.1	117.6	118.1	117.8
	IMC	171.5	172.4	172.9/169.6	173.1/170.5	173.2/171.1/169.0
	OC	236.0	235.2	234.9	234.7	234.5
	OMC		290.7	290.6	290.4	290.3

BIBLIOGRAPHY

[1] S. Manzeli, D. Ovchinnikov, D. Pasquier, O. V. Yazyev, and A. Kis, Nat. Rev. Mater. **2**, 17033 (2017).

[2] K. A. N. Duerloo, Y. Li, and E. J. Reed, Nat. Commun. **5**, 4214 (2014).

[3] M. Kan, J. Y. Wang, X. W. Li, S. H. Zhang, Y. W. Li, Y. Kawazoe, Q. Sun, and P. Jena, J. Phys. Chem. C **118**, 1515 (2014).

[4] J. Yan, J. Xia, X. Wang, L. Liu, J.-L. Kuo, B. K. Tay, S. Chen, W. Zhou, Z. Liu, and Z. X. Shen, Nano Lett. **15**, 8155 (2015).

[5] Y. Cao, V. Fatemi, S. Fang, K. Watanabe, T. Taniguchi, E. Kaxiras, and P. Jarillo-Herrero, Nature **556**, 43 (2018).

[6] C. R. Dean, L. Wang, P. Maher, C. Forsythe, F. Ghahari, Y. Gao, J. Katoch, M. Ishigami, P. Moon, M. Koshino, T. Taniguchi, K. Watanabe, K. L. Shepard, J. Hone, and P. Kim, Nature **497**, 598 (2013).

[7] R. Bistritzer and A. H. MacDonald, Phys. Rev. B - Condens. Matter Mater. Phys. **84**, 1 (2011).

[8] A. Splendiani, L. Sun, Y. Zhang, T. Li, J. Kim, C. Y. Chim, G. Galli, and F. Wang, Nano Lett. **10**, 1271 (2010).

[9] K. F. Mak, C. Lee, J. Hone, J. Shan, and T. F. Heinz, Phys. Rev. Lett. **105**, 136805 (2010).

[10] D. Xiao, G.-B. Bin Liu, W. Feng, X. Xu, W. Yao, W.-Y. Y. Shan, Y. Yao, W. Yao, D. Xiao, G.-B. Bin Liu, W. Feng, X. Xu, and W. Yao, Phys. Rev. Lett. **108**, 1 (2012).

[11] K. F. Mak, K. He, J. Shan, and T. F. Heinz, Nat. Nanotechnol. **7**, 494 (2012).

[12] H. Zeng, J. Dai, W. Yao, D. Xiao, and X. Cui, Nat. Nanotechnol. **7**, 490 (2012).

[13] K. F. Mak, K. L. McGill, J. Park, and P. L. McEuen, Science (80-.). **344**, 1489 (2014).

[14] A. A. Soluyanov, D. Gresch, Z. Wang, Q. Wu, M. Troyer, X. Dai, and B. A. Bernevig, Nature **527**, 495 (2015).

[15] J. R. Schaibley, H. Yu, G. Clark, P. Rivera, J. S. Ross, K. L. Seyler, W. Yao, and X. Xu, Nat. Rev. Mater. **1**, 1 (2016).

[16] G. G. Macfarlane and T. P. McLean, J. Phys. Chem. Solids **8**, 388 (1959).

[17] H. M. Hill, A. F. Rigosi, C. Roquelet, A. Chernikov, T. C. Berkelbach, D. R. Reichman, M. S. Hybertsen, L. E. Brus, and T. F. Heinz, Nano Lett. **15**, 2992 (2015).

[18] K. He, N. Kumar, L. Zhao, Z. Wang, K. F. Mak, H. Zhao, and J. Shan, Phys. Rev. Lett. **113**, 026803 (2014).

[19] Z. Ye, T. Cao, K. O'Brien, H. Zhu, X. Yin, Y. Wang, S. G. Louie, and X. Zhang, Nature **513**, 214 (2014).

[20] M. M. Ugeda, A. J. Bradley, S. F. Shi, F. H. Da Jornada, Y. Zhang, D. Y. Qiu, W. Ruan, S. K. Mo, Z. Hussain, Z. X. Shen, F. Wang, S. G. Louie, and M. F. Crommie, Nat. Mater. **13**, 1091 (2014).

[21] G.-B. Bin Liu, W.-Y. Y. Shan, Y. Yao, W. Yao, and D. Xiao, Phys. Rev. B - Condens. Matter Mater. Phys. **88**, 1 (2013).

[22] X.-X. Zhang, T. Cao, Z. Lu, Y.-C. Lin, F. Zhang, Y. Wang, Z. Li, J. C. Hone, J. A. Robinson, D. Smirnov, S. G. Louie, and T. F. Heinz, Nat. Nanotechnol. **12**, 883 (2017).

[23] Y. Zhou, G. Scuri, D. S. Wild, A. A. High, A. Dibos, L. A. Jauregui, C. Shu, K. De Greve, K. Pistunova, A. Y. Joe, T. Taniguchi, K. Watanabe, P. Kim, M. D. Lukin, and H. Park, Nat. Nanotechnol. 1 (2017).

[24] G. Wang, C. Robert, M. M. Glazov, F. Cadiz, E. Courtade, T. Amand, D. Lagarde, T. Taniguchi, K. Watanabe, B. Urbaszek, and X. Marie, Phys. Rev. Lett. **119**, 047401 (2017).

[25] S.-Y. Chen, T. Goldstein, T. Taniguchi, K. Watanabe, and J. Yan, (2018).

[26] P. Nagler, M. V. Ballottin, A. A. Mitioglu, M. V. Durnev, T. Taniguchi, K. Watanabe, A. Chernikov, C. Schüller, M. M. Glazov, P. C. M. Christianen, and T. Korn, Http://Arxiv.Org/Abs/1801.09255 (2018).

[27] S.-Y. Chen, C. Zheng, M. S. Fuhrer, and J. Yan, Nano Lett. **15**, 2526 (2015).

[28] T. Goldstein, S.-Y. Chen, J. Tong, D. Xiao, A. Ramasubramaniam, and J. Yan, Sci. Rep. **6**, 28024 (2016).

[29] S. Y. Chen, T. Goldstein, D. Venkataraman, A. Ramasubramaniam, and J. Yan, Nano Lett. **16**, 5852 (2016).

[30] S. Y. Chen, C. H. Naylor, T. Goldstein, A. T. C. Johnson, and J. Yan, ACS Nano **11**, 814 (2017).

[31] S. Y. Chen, T. Goldstein, J. Tong, T. Taniguchi, K. Watanabe, and J. Yan, Phys. Rev. Lett. **120**, 46402 (2018).

[32] T. Goldstein, S. Y. Chen, J. Tong, D. Xiao, A. Ramasubramaniam, and J. Yan, Sci. Rep. **6**, 28024 (2016).

[33] I. Jung, M. Pelton, R. Piner, D. A. Dikin, S. Stankovich, S. Watcharotone, M. Hausner, and R. S. Ruoff, Nano Lett. **7**, 3569 (2007).

[34] K. S. Novoselov, A. K. Geim, S. V Morozov, D. Jiang, Y. Zhang, S. V Dubonos, I. V Grigorieva, and A. A. Firsov, Science (80-.). **306**, 666 (2004).

[35] R. V Gorbachev, I. Riaz, R. R. Nair, R. Jalil, L. Britnell, B. D. Belle, E. W. Hill, K. S. Novoselov, K. Watanabe, T. Taniguchi, A. K. Geim, and P. Blake, Small **7**, 465 (2011).

[36] G. Rubio-Bollinger, R. Guerrero, D. de Lara, J. Quereda, L. Vaquero-Garzon, N. Agraït, R. Bratschitsch, and A. Castellanos-Gomez, Electronics **4**, 847 (2015).

[37] C. R. Dean, A. F. Young, I. Meric, C. Lee, L. Wang, S. Sorgenfrei, K. Watanabe, T. Taniguchi, P. Kim, K. L. Shepard, and J. Hone, Nat. Nanotechnol. **5**, 722 (2010).

[38] L. Wang, I. Meric, P. Y. Huang, Q. Gao, Y. Gao, H. Tran, T. Taniguchi, K. Watanabe, L. M. Campos, D. A. Muller, J. Guo, P. Kim, J. Hone, K. L. Shepard, and C. R. Dean, Science (80-.). **342**, 614 (2013).

[39] J. Maultzsch, S. Reich, and C. Thomsen, Phys. Rev. B - Condens. Matter Mater. Phys. **70**, 1 (2004).

[40] P. Nemes-Incze, Z. Osváth, K. Kamarás, and L. P. Biró, Carbon N. Y. **46**, 1435 (2008).

[41] K. Liu, L. Zhang, T. Cao, C. Jin, D. Qiu, Q. Zhou, A. Zettl, P. Yang, S. G. Louie, and F. Wang, Nat. Commun. **5**, 1 (2014).

[42] J. Ribeiro-Soares, R. M. Almeida, E. B. Barros, P. T. Araujo, M. S. Dresselhaus, L. G. Cançado, and A. Jorio, Phys. Rev. B **90**, 115438 (2014).

[43] Y. Zhao, X. Luo, H. Li, J. Zhang, P. T. Araujo, C. K. Gan, J. Wu, H. Zhang, S. Y. Quek, M. S. Dresselhaus, and Q. Xiong, Nano Lett **13**, 1007 (2013).

[44] R. Loudon, Adv. Phys. **13**, 423 (1964).

[45] A. Molina-Sánchez and L. Wirtz, Phys. Rev. B **84**, 155413 (2011).

[46] C. Lee, H. Yan, L. E. Brus, T. F. Heinz, J. Hone, and S. Ryu, ACS Nano **4**, 2695 (2010).

[47] X. Zhang, W. Han, J. Wu, S. Milana, Y. Lu, Q. Li, A. Ferrari, and P. Tan, Phys. Rev. B **87**, 115413 (2013).

[48] A. Berkdemir, H. R. Gutiérrez, A. R. Botello-Méndez, N. Perea-López, A. L. Elías, C.-I. Chia, B. Wang, V. H. Crespi, F. López-Urías, J.-C. Charlier, H. Terrones, and M. Terrones, Sci Rep **3**, 1755 (2013).

[49] A. A. Mitioglu, P. Plochocka, G. Deligeorgis, S. Anghel, L. Kulyuk, and D. K. Maude, Phys. Rev. B **89**, 245442 (2014).

[50] P. Tonndorf, R. Schmidt, P. Böttger, X. Zhang, J. Börner, A. Liebig, M. Albrecht, C. Kloc, O. Gordan, D. R. T. Zahn, S. M. de Vasconcellos, and R. Bratschitsch, Opt. Express **21**, 4908 (2013).

[51] H. Li, Q. Zhang, C. C. R. Yap, B. K. Tay, T. H. T. Edwin, A. Olivier, and D. Baillargeat, Adv. Funct. Mater. **22**, 1385 (2012).

[52] H. Terrones, E. Del Corro, S. Feng, J. M. Poumirol, D. Rhodes, D. Smirnov, N. R. Pradhan, Z. Lin, M. A. Nguyen, A. L. Elias, T. E. Mallouk, L. Balicas, M. A. Pimenta, and M. Terrones, Sci Rep **4**, 4215 (2014).

[53] W. Zhao, Z. Ghorannevis, K. K. Amara, J. R. Pang, M. Toh, X. Zhang, C. Kloc, P. H. Tan, and G. Eda, Nanoscale **5**, 9677 (2013).

[54] X. Luo, Y. Zhao, J. Zhang, M. Toh, C. Kloc, Q. Xiong, and S. Y. Quek, Phys. Rev. B **88**, 195313 (2013).

[55] D. J. Late, S. N. Shirodkar, U. V Waghmare, V. P. Dravid, and C. N. Rao, Chemphyschem **15**, 1592 (2014).

[56] P. H. Tan, W. P. Han, W. J. Zhao, Z. H. Wu, K. Chang, H. Wang, Y. F. Wang, N. Bonini, N. Marzari, N. Pugno, G. Savini, A. Lombardo, and A. C. Ferrari, Nat Mater **11**, 294 (2012).

[57] C. H. Lui and T. F. Heinz, Phys. Rev. B **87**, 121404 (2013).

[58] C. H. Lui, Z. Ye, C. Keiser, X. Xiao, and R. He, Nano Lett **14**, 4615 (2014).

[59] E. Cappelluti, R. Roldán, J. A. Silva-Guillén, P. Ordejón, and F. Guinea, Phys. Rev. B **88**, 75409 (2013).

[60] X. Qian, J. Liu, L. Fu, and J. J. Li, Science (80-.). **346**, 1344 (2014).

[61] Y. Sun, S. C. Wu, M. N. Ali, C. Felser, and B. Yan, Phys. Rev. B - Condens. Matter Mater. Phys. **92**, 1 (2015).

[62] Y. Qi, P. G. Naumov, M. N. Ali, C. R. Rajamathi, W. Schnelle, O. Barkalov, M. Hanfland, S.-C. Wu, C. Shekhar, Y. Sun, V. Süß, M. Schmidt, U. Schwarz, E. Pippel, P. Werner, R. Hillebrand, T. Förster, E. Kampert, S. Parkin, R. J. Cava, C. Felser, B. Yan, and S. A. Medvedev, Nat. Commun. **7**, 11038 (2016).

[63] F. C. Chen, X. Luo, R. C. Xiao, W. J. Lu, B. Zhang, H. X. Yang, J. Q. Li, Q. L. Pei, D. F. Shao, R. R. Zhang, L. S. Ling, C. Y. Xi, W. H. Song, and Y. P. Sun, Appl. Phys. Lett. **108**, 162601 (2016).

[64] A. Tamai, Q. S. Wu, I. Cucchi, F. Y. Bruno, S. Ricco, T. K. Kim, M. Hoesch, C. Barreteau, E. Giannini, C. Bernard, A. A. Soluyanov, and F. Baumberger, 1 (2016).

[65] N. Xu, Z. J. Wang, A. P. Weber, A. Magrez, P. Bugnon, H. Berger, C. E. Matt, J. Z. Ma, B. B. Fu, B. Q. Lv, N. C. Plumb, M. Radovic, E. Pomjakushina, K. Conder, T. Qian, J. H. Dil, J. Mesot, H. Ding, and M. Shi, Arxiv 1 (2016).

[66] A. Liang, J. Huang, S. Nie, Y. Ding, Q. Gao, C. Hu, S. He, Y. Y. Zhang, C. Wang, B. Shen, J. Liu, P. Ai, L. Yu, X. Sun, W. Zhao, S. Lv, D. Liu, C. Li, Y. Y. Zhang, Y. Hu, Y. Xu, L. Zhao, G. Liu, Z. Mao, X. Jia, F. Zhang, S. Zhang, F. Yang, Z.

Wang, Q. Peng, H. Weng, X. Dai, Z. Fang, Z. Xu, C. Chen, and X. J. Zhou, ArXiv 1 (2016).

[67] J. Jiang, Z. K. Liu, Y. Sun, H. F. Yang, R. Rajamathi, Y. P. Qi, L. X. Yang, C. Chen, H. Peng, C.-C. Hwang, S. Z. Sun, S.-K. Mo, I. Vobornik, J. Fujii, S. S. P. Parkin, C. Felser, B. H. Yan, and Y. L. Chen, ArXiv 1604.00139 (2016).

[68] I. Belopolski, S.-Y. Xu, Y. Ishida, X. Pan, P. Yu, D. S. Sanchez, M. Neupane, N. Alidoust, G. Chang, T.-R. Chang, Y. Wu, G. Bian, H. Zheng, S.-M. Huang, C.-C. Lee, D. Mou, L. Huang, Y. Song, B. Wang, G. Wang, Y.-W. Yeh, N. Yao, J. E. Rault, P. Le Fèvre, F. Bertran, H.-T. Jeng, T. Kondo, A. Kaminski, H. Lin, Z. Liu, F. Song, S. Shin, and M. Z. Hasan, ArXiv **1604.07079**, (2016).

[69] K. Deng, G. Wan, P. Deng, K. Zhang, S. Ding, E. Wang, M. Yan, H. Huang, H. Zhang, Z. Xu, J. Denlinger, A. Fedorov, H. Yang, W. Duan, H. Yao, Y. Wu, y S. Fan, H. Zhang, X. Chen, and S. Zhou, ArXiv 1 (2016).

[70] L. Huang, T. M. McCormick, M. Ochi, Z. Zhao, M. Suzuki, R. Arita, Y. Wu, D. Mou, H. Cao, J. Yan, N. Trivedi, and A. Kaminski, 1 (2016).

[71] C. H. Naylor, W. M. Parkin, J. Ping, Z. Gao, Y. R. Zhou, Y. Kim, F. Streller, R. W. Carpick, A. M. Rappe, M. Drndić, J. M. Kikkawa, and A. T. C. Johnson, Nano Lett. **16**, 4297 (2016).

[72] T. Hahn, *International Tables for Crystallography, Volume A: Space Group Symmetry.*, 5th ed. (Springer, Berlin, Germany, 2002).

[73] B. E. Brown, Acta Crystallogr. **20**, 268 (1966).

[74] R. Clarke, E. Marseglia, and H. P. Hughes, Philos. Mag. Part B **38**, 121 (1978).

[75] G. Kresse and J. Furthmüller, Comput. Mater. Sci. **6**, 15 (1996).

[76] J. Klimeš, D. R. Bowler, and A. Michaelides, Phys. Rev. B **83**, 195131 (2011).

[77] M. Dion, H. Rydberg, E. Schröder, D. C. Langreth, and B. I. Lundqvist, Phys. Rev. Lett. **92**, 246401 (2004).

[78] T. Björkman, J. Chem. Phys. **141**, 074708 (2014).

[79] S.-Y. Chen, C. Zheng, M. S. Fuhrer, and J. Yan, Nano Lett. **15**, 2526 (2015).

[80] H. B. Ribeiro, M. A. Pimenta, C. J. S. De Matos, R. L. Moreira, A. S. Rodin, J. D. Zapata, E. A. T. De Souza, and A. H. Castro Neto, ACS Nano **9**, 4270 (2015).

[81] X. Ling, S. Huang, E. H. Hasdeo, L. Liang, W. M. Parkin, Y. Tatsumi, A. Nugraha, A. A. Puretzky, P. Masih Das, B. G. Sumpter, D. Geohegan, J. Kong, R. Saito, M. Drndic, V. Meunier, and M. S. Dresselhaus, Nano Lett. acs. nanolett.5b04540 (2016).

[82] C. Kranert, C. Sturm, R. Schmidt-Grund, and M. Grundmann, Phys. Rev. Lett. **116**, 1 (2016).

[83] K. H. Matlack, J. Y. Kim, L. J. Jacobs, and J. Qu, J. Nondestruct. Eval. **34**, (2015).

[84] F. Zheng, C. Cai, S. Ge, X. Zhang, X. Liu, H. Lu, Y. Zhang, J. Qiu, T. Taniguchi, K. Watanabe, S. Jia, J. Qi, J.-H. Chen, D. Sun, and J. Feng, Adv. Mater. **28**, 4845 (2016).

[85] D. H. Keum, S. Cho, J. H. Kim, D.-H. Choe, H.-J. Sung, M. Kan, H. Kang, J.-Y. Hwang, S. W. Kim, H. Yang, K. J. Chang, and Y. H. Lee, Nat. Phys. **11**, 482 (2015).

[86] M. Acerce, D. Voiry, and M. Chhowalla, Nat. Nanotechnol. **10**, 313 (2015).

[87] D. Voiry, H. Yamaguchi, J. Li, R. Silva, D. C. B. Alves, T. Fujita, M. Chen, T. Asefa, V. B. Shenoy, G. Eda, and M. Chhowalla, Nat. Mater. **12**, 850 (2013).

[88] G. H. Han, D. H. Keum, J. Zhao, B. G. Shin, S. Song, J. J. Bae, J. Lee, J. Hokim, H. Kim, B. H. Moon, and Y. H. Lee, 2D Mater. **3**, 031010 (2016).

[89] C. H. Lee, E. C. Silva, L. Calderin, M. A. T. Nguyen, M. J. Hollander, B. Bersch, T. E. Mallouk, and J. A. Robinson, Sci. Rep. **5**, 10013 (2015).

[90] Y. Kim, Y. I. Jhon, J. Park, J. H. Kim, S. Lee, and Y. M. Jhon, Nanoscale **8**, 2309 (2016).

[91] Y. C. Jiang, J. Gao, and L. Wang, Sci. Rep. **6**, 1 (2016).

[92] J. Lee, F. Ye, Z. Wang, R. Yang, J. Hu, Z. Mao, J. Wei, and P. X.-L. Feng, Nanoscale **8**, 7854 (2016).

[93] J. C. Park, S. J. Yun, H. Kim, J. H. Park, S. H. Chae, S. J. An, J. G. Kim, S. M. Kim, K. K. Kim, and Y. H. Lee, ACS Nano **9**, 6548 (2015).

[94] M. M. Lucchese, F. Stavale, E. H. H. M. Ferreira, C. Vilani, M. V. O. Moutinho, R. B. Capaz, C. A. Achete, and A. Jorio, Carbon N. Y. **48**, 1592 (2010).

[95] J. S. Kim, Y. Liu, W. Zhu, S. Kim, D. Wu, L. Tao, A. Dodabalapur, K. Lai, and D. Akinwande, Sci. Rep. **5**, 8989 (2015).

[96] F. Ye, J. Lee, J. Hu, Z. Mao, J. Wei, and P. X.-L. Feng, Small **12**, 5802 (2016).

[97] V. N. Denisov, A. N. Ivlev, A. S. Lipin, B. N. Mavrin, and V. G. Orlov, J. Phys. Condens. Matter **9**, 4967 (1997).

[98] R. M. Martin, G. Lucovsky, and K. Helliwell, Phys. Rev. B **13**, 1383 (1976).

[99] I. H. Campbell and P. M. Fauchet, Solid State Commun. **58**, 739 (1986).

[100] S. Wang, W. Guan, D. Ma, X. Chen, L. Wan, S. Huang, and J. Wang, CrystEngComm **12**, 166 (2010).

[101] S. Cho, S. Kim, J. H. Kim, J. Zhao, J. Seok, D. H. Keum, J. Baik, D. H. Choe, K. J. Chang, K. Suenaga, S. W. Kim, Y. H. Lee, and H. Yang, Science (80-.). **349**, 625 (2015).

[102] G. H. Han, D. H. Keum, J. Zhao, B. G. Shin, S. Song, J. J. Bae, J. Lee, J. H. Kim, H. Kim, B. H. Moon, and Y. H. Lee, 2D Mater **3**, 1 (2016).

[103] F. Ye, J. Lee, J. Hu, Z. Mao, J. Wei, and P. X.-L. Feng, Small 1 (2016).

[104] L. Colombier, J. Selles, E. Rousseau, J. Lauret, F. Vialla, C. Voisin, and G. Cassabois, Phys. Rev. Lett. **109**, 197402 (2012).

[105] J. C. Kim, D. R. Wake, and J. P. Wolfe, Phys. Rev. B **50**, 15099 (1994).

[106] M. Nakayama, H. Ichida, and H. Nishimura, J. Phys. Condens. Matter **11**, 7653 (1999).

[107] J. Renard, R. Songmuang, C. Bougerol, B. Daudin, and B. Gayral, Nano Lett. **8**, 2092 (2008).

[108] A. Srivastava, M. Sidler, A. V. Allain, D. S. Lembke, A. Kis, A. Imamoɬlu, and A. Imamoğlu, Nat. Phys. **11**, 141 (2015).

[109] G. Aivazian, Z. Gong, A. M. Jones, R. L. Chu, J. Yan, D. G. Mandrus, C. Zhang, D. Cobden, W. Yao, and X. Xu, Nat. Phys. **11**, 148 (2015).

[110] J. Wierzbowski, J. Klein, F. Sigger, C. Straubinger, M. Kremser, T. Taniguchi, K. Watanabe, U. Wurstbauer, A. W. Holleitner, M. Kaniber, K. Müller, and J. J. Finley, Sci. Rep. **7**, 12383 (2017).

[111] F. Cadiz, E. Courtade, C. Robert, G. Wang, Y. Shen, H. Cai, T. Taniguchi, K. Watanabe, H. Carrere, D. Lagarde, M. Manca, T. Amand, P. Renucci, S. Tongay, X. Marie, and B. Urbaszek, Phys. Rev. X **7**, 021026 (2017).

[112] Z. Wang, L. Zhao, K. F. Mak, and J. Shan, Nano Lett. **17**, 740 (2017).

[113] A. M. Jones, H. Yu, J. R. Schaibley, J. Yan, D. G. Mandrus, T. Taniguchi, K. Watanabe, H. Dery, W. Yao, and X. Xu, Nat. Phys. **12**, 323 (2016).

[114] A. M. Jones, H. Yu, N. J. Ghimire, S. Wu, G. Aivazian, J. S. Ross, B. Zhao, J. Yan, D. G. Mandrus, D. Xiao, W. Yao, and X. Xu, Nat. Nanotechnol. **8**, 634 (2013).

[115] T. Cao, G. Wang, W. Han, H. Ye, C. Zhu, J. Shi, Q. Niu, P. Tan, E. Wang, B. Liu, and J. Feng, Nat. Commun. **3**, 887 (2012).

[116] X. X. Zhang, Y. You, S. Y. F. Zhao, and T. F. Heinz, Phys. Rev. Lett. **115**, 1 (2015).

[117] Y. You, X. X. Zhang, T. C. Berkelbach, M. S. Hybertsen, D. R. Reichman, and T. F. Heinz, Nat. Phys. **11**, 477 (2015).

[118] D. K. Zhang, D. W. Kidd, and K. Varga, Nano Lett. **15**, 7002 (2015).

[119] M. Z. Mayers, T. C. Berkelbach, M. S. Hybertsen, and D. R. Reichman, Phys. Rev. B **92**, 161404 (2015).

[120] I. Kylänpää and H.-P. Komsa, Phys. Rev. B **92**, 205418 (2015).

[121] M. Szyniszewski, E. Mostaani, N. D. Drummond, and V. I. Fal'ko, Phys. Rev. B **95**, 081301 (2017).

[122] E. Mostaani, M. Szyniszewski, C. H. Price, R. Maezono, M. Danovich, R. J. Hunt, N. D. Drummond, and V. I. Fal'ko, Phys. Rev. B **96**, 075431 (2017).

[123] K. Hao, G. Moody, F. Wu, C. K. Dass, L. Xu, C. H. Chen, L. Sun, M. Y. Li, L. J. Li, A. H. MacDonald, and X. Li, Nat. Phys. **12**, 677 (2016).

[124] A. Steinhoff, M. Florian, A. Singh, K. Tran, M. Kolarczik, S. Helmrich, A. W. Achtstein, U. Woggon, N. Owschimikow, F. Jahnke, and X. Li, Http://Arxiv.Org/Abs/1801.04225 (2018).

[125] K. Hao, J. F. Specht, P. Nagler, L. Xu, K. Tran, A. Singh, C. K. Dass, C. Schüller, T. Korn, M. Richter, A. Knorr, X. Li, and G. Moody, Nat. Commun. **8**, 15552 (2017).

[126] Y. Li, A. Chernikov, X. Zhang, A. Rigosi, H. M. Hill, A. M. van der Zande, D. A. Chenet, E.-M. Shih, J. Hone, and T. F. Heinz, Phys. Rev. B **90**, 205422 (2014).

[127] C. Robert, D. Lagarde, F. Cadiz, G. Wang, B. Lassagne, T. Amand, A. Balocchi, P. Renucci, S. Tongay, B. Urbaszek, and X. Marie, Phys. Rev. B **93**, 1 (2016).

[128] A. Kormányos, G. Burkard, M. Gmitra, J. Fabian, V. Zólyomi, N. D. Drummond, and V. Fal'ko, 2D Mater. **2**, 022001 (2015).

[129] M. Z. Maialle, E. A. De Andrada E Silva, and L. J. Sham, Phys. Rev. B **47**, 15776 (1993).

[130] H. S. Lee, M. S. Kim, H. Kim, and Y. H. Lee, Phys. Rev. B **93**, 140409 (2016).

[131] J. Pei, J. Yang, X. Wang, F. Wang, S. Mokkapati, T. Lü, J. C. Zheng, Q. Qin, D. Neshev, H. H. Tan, C. Jagadish, and Y. Lu, ACS Nano **11**, 7468 (2017).

[132] J. Shang, X. Shen, C. Cong, N. Peimyoo, B. Cao, M. Eginligil, and T. Yu, ACS Nano **9**, 647 (2015).

[133] T. Kazimierczuk, D. Fröhlich, S. Scheel, H. Stolz, and M. Bayer, Nature **514**, 343 (2014).

[134] M. Saffman, T. G. Walker, and K. Mølmer, Rev. Mod. Phys. **82**, 2313 (2010).

[135] E. F. Gross, Nuovo Cim. Ser. 10 **3**, 672 (1956).

[136] A. A. Mitioglu, P. Plochocka, Á. Granados del Aguila, P. C. M. Christianen, G. Deligeorgis, S. Anghel, L. Kulyuk, and D. K. Maude, Nano Lett. **15**, 4387 (2015).

[137] A. V. Stier, K. M. McCreary, B. T. Jonker, J. Kono, and S. A. Crooker, Nat. Commun. **7**, 10643 (2016).

[138] G. Plechinger, P. Nagler, A. Arora, A. Granados del Águila, M. V. Ballottin, T. Frank, P. Steinleitner, M. Gmitra, J. Fabian, P. C. M. Christianen, R. Bratschitsch, C. Schüller, and T. Korn, Nano Lett. **16**, 7899 (2016).

[139] A. V. Stier, N. P. Wilson, K. A. Velizhanin, J. Kono, X. Xu, and S. A. Crooker, Phys. Rev. Lett. **120**, 1 (2018).

[140] A. Chernikov, T. C. Berkelbach, H. M. Hill, A. Rigosi, Y. Li, O. B. Aslan, D. R. Reichman, M. S. Hybertsen, and T. F. Heinz, Phys. Rev. Lett. **113**, 1 (2014).

[141] F. Yang, M. Wilkinson, E. J. Austin, and K. P. O'Donnell, Phys. Rev. Lett. **70**, 323 (1993).

[142] M. Manca, M. M. Glazov, C. Robert, F. Cadiz, T. Taniguchi, K. Watanabe, E. Courtade, T. Amand, P. Renucci, X. Marie, G. Wang, and B. Urbaszek, Nat. Commun. **8**, 1 (2017).

[143] A. V. Stier, N. P. Wilson, K. A. Velizhanin, J. Kono, X. Xu, and S. A. Crooker, Phys. Rev. Lett. **120**, 057405 (2018).

[144] B. Fallahazad, H. C. P. Movva, K. Kim, S. Larentis, T. Taniguchi, K. Watanabe, S. K. Banerjee, and E. Tutuc, Phys. Rev. Lett. **116**, 1 (2016).

[145] M. V. Gustafsson, M. Yankowitz, C. Forsythe, D. Rhodes, K. Watanabe, T. Taniguchi, J. Hone, X. Zhu, and C. R. Dean, Nat. Mater. **17**, 411 (2018).

[146] Z. Wang, J. Shan, and K. F. Mak, Nat. Nanotechnol. **12**, 144 (2017).

[147] Z. Wang, K. F. Mak, and J. Shan, Phys. Rev. Lett. **120**, 66402 (2018).

[148] R. Schmidt, A. Arora, G. Plechinger, P. Nagler, A. Granados Del Águila, M. V. Ballottin, P. C. M. Christianen, S. Michaelis De Vasconcellos, C. Schüller, T. Korn, R. Bratschitsch, A. G. Águila, and M. V. Ballottin, Phys. Rev. Lett. **117**, 1 (2016).

[149] Z. Ye, D. Sun, and T. F. Heinz, Nat. Phys. **13**, 26 (2017).

[150] H. Dery and Y. Song, Phys. Rev. B - Condens. Matter Mater. Phys. **92**, 125431 (2015).

[151] G. Kioseoglou, A. T. Hanbicki, M. Currie, A. L. Friedman, and B. T. Jonker, Sci. Rep. **6**, 25041 (2016).

[152] G. Wang, E. Palleau, T. Amand, S. Tongay, X. Marie, and B. Urbaszek, Appl. Phys. Lett. **106**, 112101 (2015).

[153] T. Yan, J. Ye, X. Qiao, P. Tan, and X. Zhang, Phys. Chem. Chem. Phys. **19**, 3176 (2017).

[154] C. Poellmann, P. Steinleitner, U. Leierseder, P. Nagler, G. Plechinger, M. Porer, R. Bratschitsch, C. Schüller, T. Korn, and R. Huber, Nat. Mater. **14**, 889 (2015).

[155] M. Palummo, M. Bernardi, and J. C. Grossman, Nano Lett. **15**, 2794 (2015).

[156] H. Wang, C. Zhang, W. Chan, C. Manolatou, S. Tiwari, and F. Rana, Phys. Rev. B **93**, 1 (2016).

[157] K. P. O'Donnell and X. Chen, Appl. Phys. Lett. **58**, 2924 (1991).

[158] M. Selig, G. Berghäuser, A. Raja, P. Nagler, C. Schüller, T. F. Heinz, T. Korn, A. Chernikov, E. Malic, and A. Knorr, Nat. Commun. **7**, (2016).

[159] H. Sahin, S. Tongay, S. Horzum, W. Fan, J. Zhou, J. Li, J. Wu, and F. M. Peeters, Phys. Rev. B **87**, 165409 (2013).

[160] G. Moody, C. Kavir Dass, K. Hao, C. H. Chen, L. J. Li, A. Singh, K. Tran, G. Clark, X. Xu, G. Berghäuser, E. Malic, A. Knorr, and X. Li, Nat. Commun. **6**, 1 (2015).

[161] B. Zhu, H. Zeng, J. Dai, Z. Gong, and X. Cui, Proc. Natl. Acad. Sci. **111**, 11606 (2014).

[162] H. Yu, G. Bin Liu, P. Gong, X. Xu, and W. Yao, Nat. Commun. **5**, 35 (2014).

[163] G. Wang, M. Glazov, C. Robert, T. Amand, X. Marie, and B. Urbaszek, Phys. Rev. Lett. **115**, 1 (2015).

[164] C. M. Chow, H. Yu, A. M. Jones, J. Yan, D. G. Mandrus, T. Taniguchi, K. Watanabe, W. Yao, and X. Xu, Nano Lett. **17**, 1194 (2017).

[165] C. M. Chow, H. Yu, A. M. Jones, J. R. Schaibley, M. Koehler, D. G. Mandrus, R. Merlin, W. Yao, and X. Xu, Npj 2D Mater. Appl. (2017).

[166] C. Jin, J. Kim, J. Suh, Z. Shi, B. Chen, X. Fan, M. Kam, K. Watanabe, T. Taniguchi, S. Tongay, A. Zettl, J. Wu, and F. Wang, Nat. Phys. **13**, 127 (2016).

[167] Z. Wu, Z. Luo, Y. Shen, W. Zhao, W. Wang, H. Nan, X. Guo, L. Sun, X. Wang, Y. You, and Z. Ni, Nano Res. **9**, 3622 (2016).

[168] B. Scharf, Z. Wang, D. Van Tuan, J. Shan, K. F. Mak, I. Zutic, and H. Dery, 1 (2016).

[169] Z. Wu, W. Zhao, J. Jiang, T. Zheng, Y. You, J. Lu, and Z. Ni, J. Phys. Chem. C **121**, 12294 (2017).

[170] S. Mouri, Y. Miyauchi, M. Toh, W. Zhao, G. Eda, and K. Matsuda, Phys. Rev. B - Condens. Matter Mater. Phys. **90**, 1 (2014).

[171] D. Sun, Y. Rao, G. A. Reider, G. Chen, Y. You, L. Brézin, A. R. Harutyunyan, and T. F. Heinz, Nono Lett. **14**, 5625 (2014).